



**Top-Quark Mass Determinations  
in the  $e\mu$  Dilepton Channel**

and

**Top-Quark Mass Effects in  
Higgs Boson Pair Production**

**Ludovic M. Scyboz**





# Top-Quark Mass Determinations in the $e\mu$ Dilepton Channel

and

## Top-Quark Mass Effects in Higgs Boson Pair Production

Ludovic M. Scyboz

Vollständiger Abdruck der von der Fakultät für Physik der Technischen Universität München zur Erlangung des akademischen Grades eines

Doktors der Naturwissenschaften (Dr. rer. nat.)

genehmigten Dissertation.

**Vorsitzender:**

Prof. Dr. Andreas Weiler

**Prüfende der Dissertation:**

1. Dr. Stefan Kluth
2. Prof. Dr. Wolfgang Hollik,  
Technische Universität München

Die Dissertation wurde am 16.05.2019 bei der Technischen Universität München eingereicht und durch die Fakultät für Physik angenommen.



## <sup>5</sup> Abstract

<sup>6</sup> In the Standard Model (SM) of Particle Physics, the top-quark plays the role of a center-  
<sup>7</sup> piece. It interacts across all sectors and with all gauge fields, and has been successfully  
<sup>8</sup> used as a portal to precision measurements of the SM parameters. Top-quarks are  
<sup>9</sup> also indirectly related to other SM sectors, for example to Higgs boson production pro-  
<sup>10</sup> cesses which are induced predominantly by top-quark loops at the Large Hadron Collider  
<sup>11</sup> (LHC). During Runs I and II of the LHC, a large number of top-quark pair ( $t\bar{t}$ ) and  
<sup>12</sup> single-top events were recorded. They allowed to reduce the experimental uncertainty  
<sup>13</sup> on top-quark properties, like the top-quark mass, but also spin correlations and  $W$  bo-  
<sup>14</sup> son polarization in  $t\bar{t}$  events, the  $Wtb$  coupling, or flavour-changing neutral currents. In  
<sup>15</sup> the case of the top-quark mass, the experimental uncertainties of the latest ATLAS and  
<sup>16</sup> CMS combination are now competing with theoretical uncertainties: approximations  
<sup>17</sup> that were previously thought to be appropriate must be reevaluated.

<sup>18</sup> In particular, the narrow-width approximation (NWA) for top-quark pair production  
<sup>19</sup> assumes the production of an on-shell top- and antitop-quark, and is used in Monte-Carlo  
<sup>20</sup> (MC) predictions for most experimental measurements. Since the actual final-state is  
<sup>21</sup> composed of the top-quark pair decay products, a more accurate description of the signal  
<sup>22</sup> should consider  $W^+W^-b\bar{b}$  final-states instead. The full final-state includes contributions  
<sup>23</sup> that cannot be factorized in both top-quark decay legs, or that do not contain a top-quark  
<sup>24</sup> pair to begin with. These diagrams are called non-factorizing, respectively non-doubly  
<sup>25</sup> resonant. In cases where measurements rely on phase-space regions sensitive to these  
<sup>26</sup> contributions, the extracted top-quark mass will be biased.

<sup>27</sup> In this work, we take the example of the 8 TeV ATLAS top-quark mass analysis in the  
<sup>28</sup>  $e\mu$  dilepton channel, which bases on simulated templates to extract the MC top-quark  
<sup>29</sup> mass by an unbinned likelihood fit. In a similar setup, we compare the extracted top-  
<sup>30</sup> quark masses at parton-level for different theoretical descriptions of the  $t\bar{t}$  final-state at  
<sup>31</sup> next-to-leading order (NLO) in production. In this respect, MC events are produced for  
<sup>32</sup> three different descriptions of the top-quark decay in the NWA, as well as for the full  
<sup>33</sup>  $W^+W^-b\bar{b}$  process at NLO in production. The top-quark mass  $m_t^{\text{MC}}$  extracted by the  
<sup>34</sup> template fit method is compared for each of these theoretical descriptions, and important  
<sup>35</sup> offsets of up to  $\Delta m_t^{\text{MC}} \sim 1$  GeV are underlined. A more realistic assessment, where these  
<sup>36</sup> predictions are folded to detector-level, is also presented.

<sup>37</sup> As mentioned, the top-quark mass also plays an important role in other sectors of the  
<sup>38</sup> SM. With the example of di-Higgs production with non-SM values of the Higgs couplings,  
<sup>39</sup> we show that the  $m_t$ -dependence of QCD NLO corrections introduces sizeable differences  
<sup>40</sup> with respect to predictions where top-quark degrees of freedom are integrated out. A  
<sup>41</sup> full-fledged MC event generator (with the possibility of varying the Higgs self-coupling  
<sup>42</sup> and the Higgs-top Yukawa coupling) is introduced.



## <sup>43</sup> Zusammenfassung

<sup>44</sup> Im Standard-Modell (SM) der Teilchenphysik spielt das Top-Quark eine zentrale Rolle.  
<sup>45</sup> Es wechselwirkt mit Teilchen aller Sektoren sowie mit allen quantentheoretischen Eich-  
<sup>46</sup> feldern, und wurde in verschiedenen Zusammenhängen als Grundpfeiler für Präzisions-  
<sup>47</sup> messungen des SM verwendet. Top-Quarks sind auch eng mit anderen Sektoren des  
<sup>48</sup> SM verbunden: Higgs-Bosonen zum Beispiel werden am Large Hadron Collider (LHC)  
<sup>49</sup> überwiegend durch Top-Quark-Schleifen erzeugt. Während Runs I und II des LHC  
<sup>50</sup> wurde eine große Anzahl an Top-Quark-Paar ( $t\bar{t}$ ) und Einzel-Top-Events ermittelt. Diese  
<sup>51</sup> haben es ermöglicht, Messungen von Top-Quark-Eigenschaften bedeutend zu verbessern,  
<sup>52</sup> beispielsweise die der Top-Quark-Masse. In diesem Fall sind die von ATLAS und CMS  
<sup>53</sup> angegebenen experimentellen Unsicherheiten zu dem Punkt gekommen, wo sie mit den  
<sup>54</sup> aktuellen theoretischen Unsicherheiten rivalisieren: das heisst insbesondere, dass früher  
<sup>55</sup> verwendete Näherungen neu abgeschätzt werden müssen.

<sup>56</sup> Die sogenannte Schmal-Breite-Näherung (NWA), bei der ein Top-Quark-Paar on-shell  
<sup>57</sup> produziert wird, wird üblicherweise in den meisten Monte-Carlo (MC) Analysen ver-  
<sup>58</sup> wendet. Weil der gemessene  $t\bar{t}$ -Endzustand aber von den Top-Zerfallsprodukten gebildet  
<sup>59</sup> wird, sollte eine konsistente Beschreibung des Signals eher auf dem intermediären  
<sup>60</sup>  $W^+W^-b\bar{b}$  Zustand beruhen. Letzterer beinhaltet Feynman-Diagramme, die entweder  
<sup>61</sup> nicht in zwei Top-Zerfall-Kanälen faktorisieren, oder überhaupt keine zwei Top-Propa-  
<sup>62</sup> gatoren aufweisen. Diese Diagramme heissen nicht-faktorisierend, bzw. nicht-doppelt-  
<sup>63</sup> resonant. Wenn Messungen durchgeführt werden, die sensitiv auf solche Beiträge sind,  
<sup>64</sup> kann sich ein systematischer Fehler in der extrahierten Top-Quark-Masse bilden.

<sup>65</sup> Wir nehmen als Beispiel die ATLAS Top-Quark-Massenanalyse im  $e\mu$ -Dileptonkanal,  
<sup>66</sup> welche auf simulierten Templates basiert zur Bestimmung der Top-Quark-Masse. In  
<sup>67</sup> einem ähnlichen Setup wird die extrahierte Top-Masse verglichen, wo unterschiedliche  
<sup>68</sup>  $t\bar{t}$ -Endzustandsbeschreibungen in nächstführender Ordnung der Störungstheorie (NLO)  
<sup>69</sup> in Produktion eingesetzt werden. Genauer werden für drei verschiedene Beschreibun-  
<sup>70</sup> gen des Top-Quark-Zerfalls, sowie für die volle NLO  $W^+W^-b\bar{b}$ -Rechnung, Verteilungen  
<sup>71</sup> erzeugt. Die mithilfe der Template-Fit-Methode extrahierte Top-Quark-Masse  $m_t^{\text{MC}}$   
<sup>72</sup> zeigt erhebliche Unterschiede bis zu  $\Delta m_t^{\text{MC}} \sim 1 \text{ GeV}$ . Eine realistischere Studie wird  
<sup>73</sup> eingeführt wo Particle-Level-Vorhersagen auf Detector-Level gefaltet werden.

<sup>74</sup> Außerdem wirken Top-Quark-Effekte auch im Higgs-Sektor. Anhand des Beispiels  
<sup>75</sup> von Higgs-Paar-Produktion ( $hh$ ) beim LHC wird gezeigt, dass die  $m_t$ -Abhängigkeit  
<sup>76</sup> von  $hh$  Produktion auf NLO QCD zu Unterschieden in differentiellen Verteilungen  
<sup>77</sup> führt im Vergleich zu Vorhersagen, wo die Top-Quark-Freiheitsgrade ausintegriert wer-  
<sup>78</sup> den. Ein vollständiges MC-Programm zur Erzeugung von Higgs-Paar-Events (wo die  
<sup>79</sup> trilineare Higgs-Selbstkopplung sowie die Higgs-Top-Yukawakopplung variiert werden  
<sup>80</sup> können) wird präsentiert.



# 81 Contents

82	<b>Abstract</b>	v
83	<b>Zusammenfassung</b>	vii
84	<b>Contents</b>	ix
85	<b>1 Introduction</b>	1
86	<b>I Theoretical and Experimental Setup</b>	5
87	<b>2 The Standard Model</b>	7
88	2.1 Matter content and gauge interactions . . . . .	7
89	2.2 The Higgs mechanism . . . . .	10
90	2.3 Top-Higgs interactions . . . . .	13
91	2.4 Outstanding issues with the Standard Model . . . . .	16
92	<b>3 Higher-order perturbative calculations in hadron-hadron collisions</b>	17
93	3.1 Divergences in Quantum-Field Theory . . . . .	17
94	3.1.1 Regularization . . . . .	17
95	3.1.2 Renormalization . . . . .	20
96	3.1.3 Perturbative expansion of Quantum Chromodynamics . . . . .	20
97	3.2 Infrared divergences . . . . .	22
98	3.3 The factorization theorem . . . . .	23
99	<b>4 Monte-Carlo (MC) event generators</b>	25
100	4.1 Matrix-element providers . . . . .	27
101	4.1.1 GoSAM: MC interfacing of one-loop amplitudes . . . . .	27
102	4.1.2 Infrared divergence cancellation . . . . .	29
103	4.2 Parton-shower models . . . . .	31
104	4.2.1 Altarelli-Parisi splitting functions . . . . .	31
105	4.2.2 The Sudakov form factor . . . . .	32
106	4.2.3 Parton-shower matching . . . . .	32
107	4.3 Hadronization . . . . .	34
108	4.3.1 Lund string model . . . . .	34
109	4.3.2 Cluster model . . . . .	34

110	<b>5 The LHC and the ATLAS detector</b>	37
111	5.1 The Large Hadron Collider . . . . .	37
112	5.2 The ATLAS detector . . . . .	38
113	5.2.1 The Inner Detector . . . . .	39
114	5.2.2 The Liquid Argon (LAr) Calorimeter . . . . .	41
115	5.2.3 The Tile Calorimeter (TileCal) . . . . .	42
116	5.2.4 The Muon Spectrometer . . . . .	42
117	5.2.5 Trigger and Data acquisition . . . . .	42
118	5.2.5.1 Data formats and Event reconstruction . . . . .	44
119	5.2.5.2 MC simulation . . . . .	45
120	<b>II Top-Quark Mass Determinations</b>	47
121	<b>6 Theoretical predictions for <math>t\bar{t}</math> final-states</b>	49
122	6.1 The narrow-width approximation (NWA) . . . . .	50
123	6.2 $W^+W^-b\bar{b}$ production: review of existing calculations . . . . .	52
124	6.3 $W^+W^-b\bar{b}$ calculation setup at NLO QCD . . . . .	53
125	6.4 Event requirements . . . . .	55
126	6.5 Total cross-section results . . . . .	56
127	<b>7 NWA versus <math>W^+W^-b\bar{b}</math>: Top-quark mass uncertainties at parton-level</b>	57
128	7.1 The template fit method . . . . .	57
129	7.2 Definition of the observables . . . . .	58
130	7.3 Comparison of the different theoretical descriptions . . . . .	60
131	7.4 Template fit results . . . . .	65
132	<b>8 Experimental resolution and bin migration</b>	71
133	8.1 Inverse problems . . . . .	71
134	8.2 Folding setup in ATLAS . . . . .	72
135	8.3 Theoretical descriptions and MC samples . . . . .	74
136	8.4 The AnalysisTop setup . . . . .	76
137	<b>9 Determination of the top-quark mass at detector-level</b>	79
138	9.1 Differential results at particle- and detector-level . . . . .	79
139	9.2 Statistical and systematic cross-checks . . . . .	79
140	9.3 Folded results and template parametrization . . . . .	80
141	9.4 Numerical result for top-quark mass uncertainties . . . . .	81
142	<b>III Top-Quark Mass Effects in Higgs Pair Production</b>	83
143	<b>10 Top-mass dependence in Higgs pair production at NLO</b>	85
144	10.1 Theoretical descriptions of $hh$ production . . . . .	86
145	10.1.1 Approximations in the heavy-top limit ( $m_t \rightarrow \infty$ ) . . . . .	87

146	10.1.2 Two-loop contribution in the SM . . . . .	88
147	10.2 The Electroweak Chiral Lagrangian . . . . .	88
148	10.3 Total cross-sections for BSM benchmark points . . . . .	90
149	10.4 Differential cross-sections and HTL approximations . . . . .	96
150	<b>11 Variations of the triple Higgs-coupling and parton-shower effects</b>	<b>99</b>
151	11.1 The Powheg-BOX framework . . . . .	99
152	11.2 Interfacing two-loop contributions . . . . .	100
153	11.3 Total and differential cross-sections at fixed-order . . . . .	101
154	11.4 Parton-shower matched predictions at NLO . . . . .	103
155	<b>12 Conclusion and Outlook</b>	<b>107</b>
156	<b>Bibliography</b>	<b>109</b>
157	<b>A Further template fit plots</b>	<b>126</b>
158	<b>B Color-flow comparisons for Sherpa</b>	<b>130</b>
159	<b>C BSM benchmark points in <math>hh</math> production</b>	<b>131</b>
160	<b>D Hardness definitions in matching Powheg to Pythia</b>	<b>134</b>
161	<b>Acknowledgments</b>	<b>135</b>



# <sup>162</sup> 1 Introduction

<sup>163</sup> The Standard Model (SM) of Particle Physics is one of the most successful physical  
<sup>164</sup> theories to date. While it still begs some unanswered questions that are outlined in  
<sup>165</sup> Chapter 2, the precision to which its predictions were tested by high-energy colliders,  
<sup>166</sup> but also in low-energy experiments, large-scale universe phenomena, neutrino and other  
<sup>167</sup> experiments is extremely convincing. In particular, the SM bases on mathematical  
<sup>168</sup> concepts that allow for a significant predictive power. Considering that physicists tend to  
<sup>169</sup> like a theory that contains the least amount of free parameters and a maximal predictive  
<sup>170</sup> power, the SM fares rather well: it contains only 19 parameters, namely the angles of the  
<sup>171</sup> Cabibbo-Kobayashi-Maskawa mixing matrix and its CP-violating phase (3+1), the gauge  
<sup>172</sup> couplings corresponding to the model’s underlying symmetries (3), the lepton and quark  
<sup>173</sup> masses (9), the QCD vacuum angle (1), and the Higgs mass and vacuum expectation  
<sup>174</sup> value (2). Since most of these parameters have been measured to an excellent precision,  
<sup>175</sup> efforts have largely concentrated on the less well-measured parameters, one of these being  
<sup>176</sup> the top-quark mass.

<sup>177</sup> Because the top-quark is the heaviest known elementary particle, with a mass from  
<sup>178</sup> the world combination measured at  $m_t = 173.0 \pm 0.4$  GeV [1], physicists had to wait  
<sup>179</sup> until 1995 for its discovery by the CDF [2] and DØ [3] experiments at Fermilab, 23  
<sup>180</sup> years after it was predicted. Only then did the last missing piece of the three quark  
<sup>181</sup> generations fall into place. Nowadays, abundant production of top-quarks with the  
<sup>182</sup> Large Hadron Collider (LHC) at CERN allows for a variety of accurate measurements  
<sup>183</sup> of its properties. Of particular interest, the precise determination of its mass is a key  
<sup>184</sup> to a deeper understanding of modern quantum-field theory (QFT). Most notably, the  
<sup>185</sup> top-quark mass enters global electroweak fits which are important for consistency testing  
<sup>186</sup> of the SM; it also strongly affects corrections to the Higgs quartic coupling, thus having  
<sup>187</sup> a large impact on the stability of the SM vacuum. Finally, being the only quark with a  
<sup>188</sup> lifetime surpassing the hadronization scale, it is the only *bare* colored particle produced  
<sup>189</sup> in SM processes. In general, one has to choose an appropriate mass definition, be it a  
<sup>190</sup> QFT-consistent definition like the pole mass (on-shell renormalized) and the  $\overline{\text{MS}}$  mass  
<sup>191</sup> (renormalized after the short-distance  $\overline{\text{MS}}$  scheme), or the so-called Monte-Carlo (MC)  
<sup>192</sup> mass.

<sup>193</sup> Recently, the ATLAS and CMS experiments, using innovative approaches and analysis  
<sup>194</sup> techniques, have been able to reduce the uncertainty of the measured MC top-quark  
<sup>195</sup> mass to about  $\Delta m_t \approx 0.5$  GeV in their respective combinations [5, 6] (see Fig. 1.1  
<sup>196</sup> for measurements at LHC). Achieving a more precise determination of  $m_t$  constitutes  
<sup>197</sup> a significant challenge for both the experimental and theoretical communities. While  
<sup>198</sup> on the one hand, experimentalists have to find new ideas to drive down the mostly  
<sup>199</sup> systematics-dominated uncertainties, theorists need to improve precision calculations by

## 1 Introduction

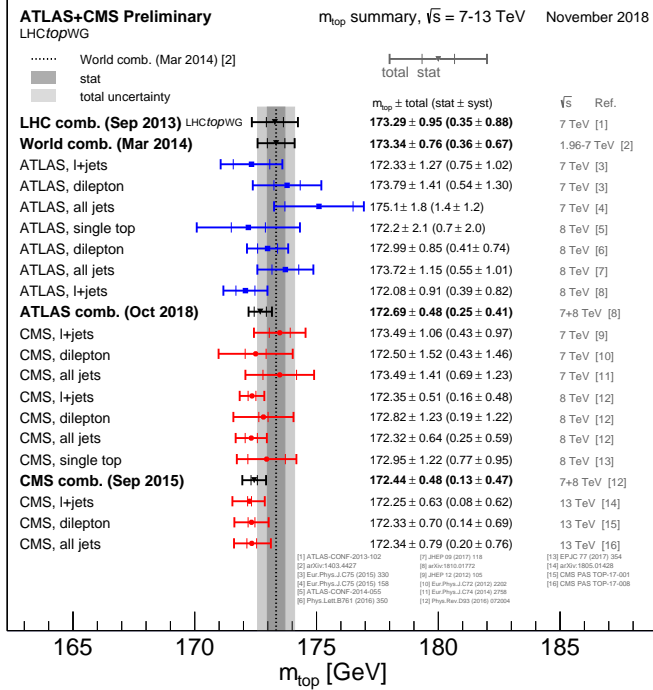


**Figure 1.1:** ATLAS and CMS combination of  $\sqrt{s} = 7, 8, 13$  TeV data for measurements of the top-quark mass  $m_t$ . Figure taken from Ref. [4].

going to higher-order predictions and beyond formerly accepted approximations. The computation of higher-order corrections for on-shell top-quark pair ( $t\bar{t}$ ) production has been a major success during the LHC era. The production of a pair of on-shell top-quarks is referred to as the narrow-width approximation (NWA). Because the corrections to NWA calculations are expected to be small, of order  $\mathcal{O}(\Gamma_t/m_t) < 1\%$  for inclusive cross-sections, most fixed-order predictions aim at computing higher-order QCD and EW corrections to top-quark pair production in this approximation.

The experimentalists, though, reconstruct the top-quark pair from their decay products, so either from the dilepton, lepton+jets or all-hadronic final-states, depending on the decay channel of the top and antitop-quarks. The fixed-order prediction of a fully-decayed  $t\bar{t}$  final-state is computationally demanding: instead of a  $2 \rightarrow 2$  process, the final-state phase space becomes that of a  $2 \rightarrow 4$  (for  $pp \rightarrow W^+W^-b\bar{b}$ ) or a  $2 \rightarrow 6$  process (including  $W$  boson decay products). A computation of the full final-state prediction at next-to-leading order (NLO) comprises Feynman diagrams that are not present in the NWA: some do not contain double-resonant top-quarks, and others include internal lines between the top-quark decay legs, i.e. the latter do not factorize. In fact, the additional interference terms can be of importance to distributions that are sensitive to higher-order and off-shell effects, for example in phase-space regions populated first at higher-order in QCD.

219 Concerning the theoretical definition of the top-quark mass, relations between different  
220 renormalization schemes are known at 4-loop order [7]. This relation suffers from an IR  
221 so-called renormalon singularity, which is associated to an intrinsically non-perturbative  
222 ambiguity in the definition of the top-quark pole mass. This inherent uncertainty was  
223 estimated to be of the order  $\mathcal{O}(250 \text{ MeV})$  [8–11]. Moreover, analyses that rely on sim-  
224 lated distributions (like the template fit method studied in the next Chapters) measure  
225 the MC top-quark mass, not the pole mass. Although the discussion on the exact rela-  
226 tion of the MC to the pole top-quark mass is still ongoing, the difference between both  
227 values is expected to be of the order  $\mathcal{O}(300 - 500 \text{ MeV})$  [12, 13].

228 In this work, we first briefly present the foundations of the SM including the Higgs  
229 mechanism and the relation between the Higgs sector and the top-quark in Chapter 2. In  
230 Chapter 3, the basics of higher-order calculations are summarized: the appearance of UV  
231 and IR divergences in loop corrections and the way to deal with them (regularization and  
232 renormalization), the perturbative expansion for QCD at high energies from the running  
233 of the strong coupling  $\alpha_s$ , and the factorization theorem for hadron-hadron collisions are  
234 laid out in some detail. Finally, we concentrate on MC event generators in Chapter 4  
235 and explain the ingredients needed for particle-level event generation. Switching to  
236 the experimental side, the LHC and in particular the ATLAS detector are presented  
237 in Chapter 5. At that point, the different theoretical descriptions of top-quark pair  
238 production are discussed in Chapter 6. With the example of top-quark pair predictions  
239 in the  $e\mu$  dilepton channel, we show how higher-order and off-shell effects can have a  
240 sizeable impact on an experimental MC top-quark mass extraction in Chapter 7. There,  
241 four different theoretical descriptions are compared with respect to an experimentally  
242 realistic top-quark mass extraction for  $pp \rightarrow W^+(\rightarrow e^+\nu_e)W^-(\rightarrow \mu^-\bar{\nu}_\mu)b\bar{b}$ . In the  
243 NWA, we produce top-quark pairs at NLO QCD, and describe the top-decay at different  
244 accuracies: LO, respectively NLO QCD, as well as operated by a parton-shower. We  
245 compare the NWA results to a full  $W^+W^-b\bar{b}$  computation at NLO QCD. Taking into  
246 account detector reconstruction efficiencies and bin migration effects, which is the subject  
247 of Chapter 8, we then quantify the shift in the extracted top-quark mass in an exact  
248 ATLAS framework in Chapter 9, where distributions are folded up to detector-level.

249 Looking at another sector entirely, we emphasize that top-quarks also play an impor-  
250 tant role in calculations for the production of one or several Higgs bosons at the LHC.  
251 Because the top-quark is the heaviest SM particle and since the Higgs boson’s coupling  
252 to fermions is proportional to their mass, higher-order corrections to Higgs processes  
253 mainly happen through top-quark loops. For instance, single Higgs production at the  
254 LHC is dominated by gluon-fusion with a top-quark loop intermediate state (so-called  
255 loop-induced production), i.e. higher-order corrections to  $gg \rightarrow h$  start at two-loop  
256 level already. The same holds for the production of a pair of Higgs bosons: this pro-  
257 cess is of particular interest, since di-Higgs production is the main channel for probing  
258 the trilinear Higgs self-coupling. Although the Higgs couplings to heavy fermions and  
259 gauge bosons are currently nicely constrained, as shown in Fig. 1.2, the best limit set  
260 on the Higgs self-coupling’s ratio  $\kappa_\lambda$  to the SM-predicted value is given by ATLAS at  
261  $-5.0 \leq \kappa_\lambda \leq 12.1$  [16]. In general, the Higgs sector is one of the more poorly explored  
262 experimentally, and it is important to have precise (at best model-independent) theoret-

## 1 Introduction

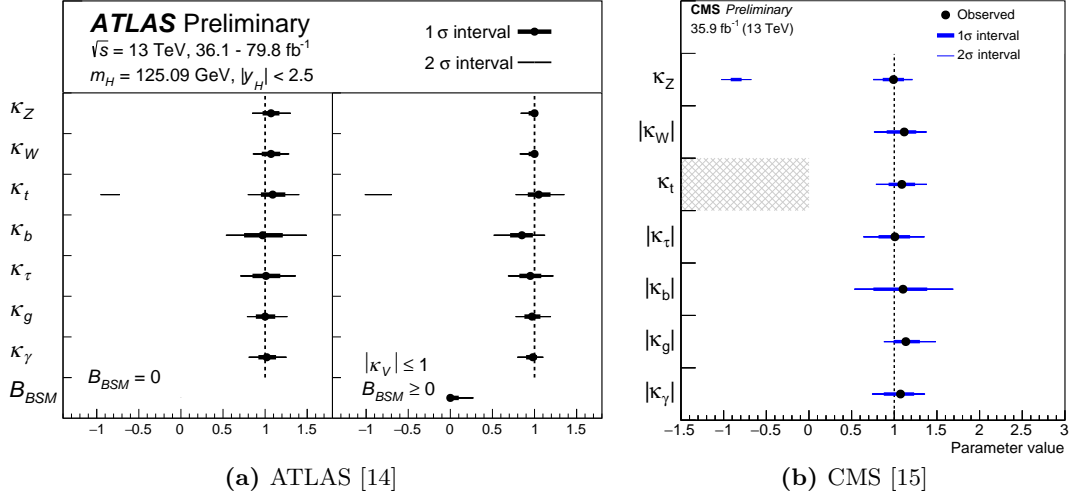


**Figure 1.2:** Fit values of the Higgs coupling modifiers with respect to the SM-predicted coupling strength (in the  $\kappa$ -framework).

ical predictions for the case where the Higgs couplings are not SM-like. We show, within a non-linear Effective Field Theory (EFT) framework allowing to vary the Higgs couplings, that the full  $m_t$ -dependence of di-Higgs production at NLO QCD has important effects, especially on differential cross-section predictions. In Chapter 10, the electroweak chiral Lagrangian (EWChL) is introduced. The results for NLO di-Higgs cross-sections and differential distributions with variations of the Higgs couplings are presented at 14 TeV for several benchmark points. Finally, the implementation of the full  $m_t$ -dependent NLO corrections for di-Higgs production into the Powheg-BOX-V2 [17–19] event generator is the subject of Chapter 11. In this package, variations of the trilinear Higgs self-coupling and the top-Higgs Yukawa coupling are now possible. We show studies comparing differential distributions for fixed-order NLO to parton-shower matched predictions, and discuss parton-shower related uncertainties. Finally, we summarize the current state of the SM and outline future, potentially interesting developments in both top-quark and Higgs physics.

277

## **Part I**

### **278 Theoretical and Experimental Setup**



## <sup>279</sup> 2 The Standard Model

<sup>280</sup> The SM was developed and supplemented over five decades, and describes all elementary  
<sup>281</sup> particles and their interactions via three of the four fundamental forces in a quantum-field  
<sup>282</sup> theoretical framework: the electromagnetic, weak and strong interactions. Although it  
<sup>283</sup> is known that the SM suffers from some theoretical shortfalls that are briefly described  
<sup>284</sup> at the end of this Chapter (like non-zero neutrino mass measurements [20]), there is, to  
<sup>285</sup> date, no experimental evidence that directly contradicts it.

<sup>286</sup> At the core, the discovery by Glashow, Salam and Weinberg [21–23] that the electro-  
<sup>287</sup> magnetic and weak interactions could be embedded in a unified theory constitutes the  
<sup>288</sup> first stone of the SM edifice. What if all known forces and particles could be described  
<sup>289</sup> by the same, unique theory? Later, the quantum chromodynamics (QCD) sector, which  
<sup>290</sup> describes the strong interaction, was correctly theorized to rely on a (non-Abelian) gauge  
<sup>291</sup> symmetry group by Wilczek, Gross and Politzer [24, 25], which leads to asymptotic free-  
<sup>292</sup> dom of color-charged particles. The addition of the Higgs mechanism, that generates  
<sup>293</sup> mass terms for the fermions and gauge bosons, culminated in what is known today as the  
<sup>294</sup> SM Lagrangian. The SM is one of the most successful theories up-to-date, and has been  
<sup>295</sup> extensively tested against experimental data. A comprehensive comparison of computed  
<sup>296</sup> cross-sections for SM processes to values measured by ATLAS, shown in Fig. 2.1, makes  
<sup>297</sup> for a compelling argument in favor of the SM’s predictive power.

### <sup>298</sup> 2.1 Matter content and gauge interactions

<sup>299</sup> The SM is a quantum-field gauge theory: the known elementary particles are interpreted  
<sup>300</sup> as the excitations of quantized fields, and their interactions are described by the exchange  
<sup>301</sup> of gauge bosons. Both matter and gauge fields obey certain rules under the corresponding  
<sup>302</sup> gauge transformations: that is, they transform according to different representations of  
<sup>303</sup> the underlying gauge group. The SM builds on the

$$SU(3)_C \times SU(2)_L \times U(1)_Y$$

<sup>304</sup> gauge group. It is the product group of the QCD group  $SU(3)_C$ , and its corresponding  
<sup>305</sup> color quantum number  $C$ , and the electroweak group  $SU(2)_L \times U(1)_Y$ , that distinguishes  
<sup>306</sup> left- from right-handed particles as doublets, respectively singlets under the group trans-  
<sup>307</sup> formation. The  $U(1)_Y$  group’s quantum number is the so-called hypercharge  $Y$ . The  
<sup>308</sup> fermionic matter fields are classified into left-handed leptons and quarks, both transform-  
<sup>309</sup> ing as doublets under the  $SU(2)_L$  group, and their singlet right-handed counterparts.  
<sup>310</sup> There are furthermore three distinct copies, called generations, or families:

## 2 The Standard Model

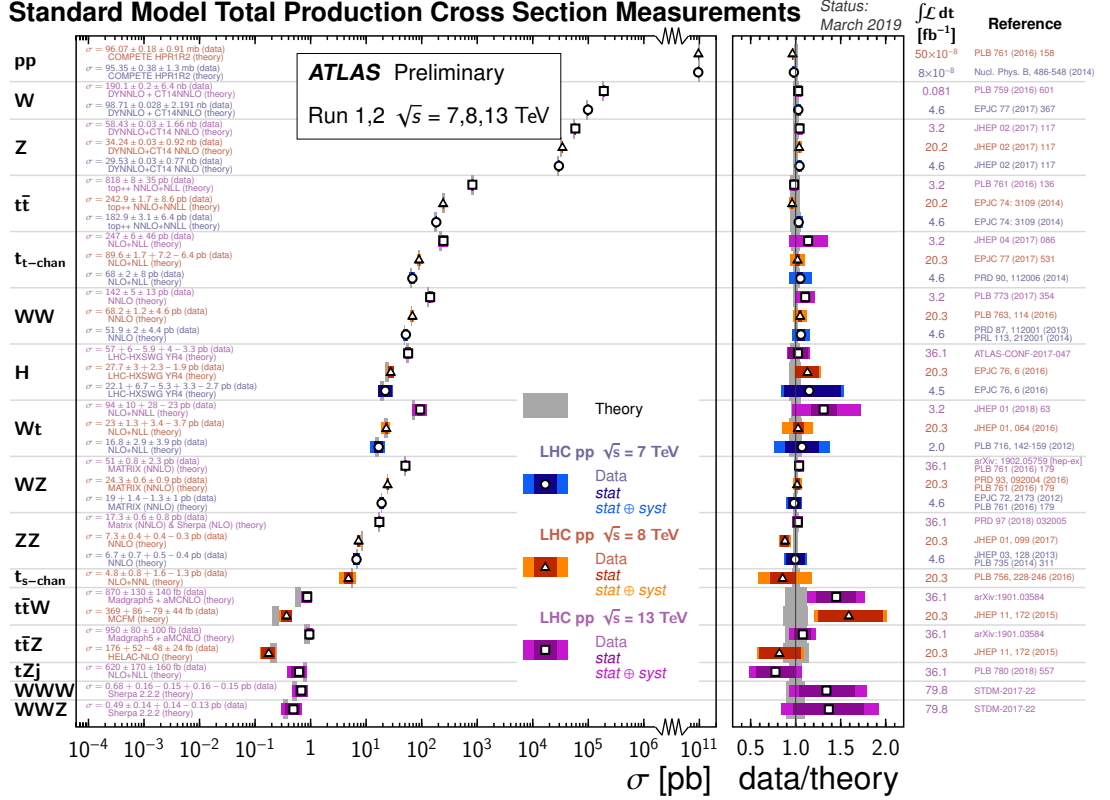


**Figure 2.1:** The predicted cross-sections (in gray, where bands represent the theoretical uncertainty) for SM production processes at LHC center-of-mass energies of  $\sqrt{s} = 7, 8, 13$  TeV are compared to their measured values at the ATLAS experiment (in color) [26]. The ratio of data to theory is shown to be compatible with 1.

$$\begin{pmatrix} \nu_e \\ e^- \end{pmatrix}_L, \quad \begin{pmatrix} u \\ d' \end{pmatrix}_L, \quad \begin{pmatrix} \nu_\mu \\ \mu^- \end{pmatrix}_L, \quad \begin{pmatrix} c \\ s' \end{pmatrix}_L, \quad \begin{pmatrix} \nu_\tau \\ \tau^- \end{pmatrix}_L, \quad \begin{pmatrix} t \\ b' \end{pmatrix}_L,$$

$$e_R^-, \quad u_R, \quad d'_R, \quad \mu_R^-, \quad c_R, \quad s'_R, \quad \tau_R^-, \quad t_R, \quad b'_R,$$

and their corresponding antiparticles. Here,  $e, \mu, \tau$  are the three lepton ( $\ell$ ) generations and their corresponding neutrinos  $\nu_\ell$ . The particles  $u, c, t$ , and  $d', s', b'$  are the up-type, respectively down-type quark weak eigenstates. The down-type eigenstates mix via the unitary Cabibbo-Kobayashi-Maskawa (CKM) matrix to give the physical mass eigenstates  $d, s, b$ :

$$\begin{pmatrix} d' \\ s' \\ b' \end{pmatrix} = \begin{pmatrix} V_{ud} & V_{us} & V_{ub} \\ V_{cd} & V_{cs} & V_{cb} \\ V_{td} & V_{ts} & V_{tb} \end{pmatrix} \begin{pmatrix} d \\ s \\ b \end{pmatrix}.$$

## 2.1 Matter content and gauge interactions

316 The quarks are the only matter fields carrying color charge, and live in the triplet **(3)**,  
 317 respectively anti-triplet **(̄3)** representations of the  $SU(3)_C$  group. The color quantum  
 318 numbers are defined as red, blue and green, respectively anti-red, anti-blue and anti-  
 319 green. That is, for the up- and down-quark:

$$\begin{pmatrix} u_r \\ u_b \\ u_g \end{pmatrix}, \quad \begin{pmatrix} d_r \\ d_b \\ d_g \end{pmatrix} \in SU(3)_C .$$

320 Governing the interactions, the gauge bosons corresponding to each subgroup couple  
 321 with a separate strength to the matter fields:

- 322 • three  $W_\mu^a$ ,  $a = (1, 2, 3)$ , bosons belonging to  $SU(2)_L$ , coupling with strength  $\propto g$ ,
- 323 • one  $B_\mu$  boson belonging to  $U(1)_Y$ , coupling with strength  $\propto g'$ ,
- 324 • eight gluon fields  $G_\mu^a$ ,  $a = (1, \dots, 8)$ , belonging to  $SU(3)_C$ , with coupling  $\propto g_s$ .

325 By the principle of gauge covariance, the interaction terms between gauge bosons and  
 326 the rest of the particle fields are given by promoting the 4-derivatives in the kinetic terms  
 327 of the corresponding sector to covariant derivatives:

$$\partial_\mu \rightarrow D_\mu = \left[ \partial_\mu + ig \frac{\sigma_a}{2} W_\mu^a + ig' \frac{Y}{2} B_\mu \right] \quad (\text{EW}) , \quad (2.1)$$

328

$$\partial_\mu \rightarrow D_\mu = \left[ \partial_\mu + ig_s T_a G_\mu^a \right] \quad (\text{QCD}) , \quad (2.2)$$

329 where  $\sigma_a$  are the three Pauli matrices (the generators of the Lie algebra of  $SU(2)_L$ ),  
 330 and  $T_a$  are the eight generators of the Lie algebra of  $SU(3)_C$ . The replacement by a  
 331 covariant derivative also induces gauge boson self-coupling interactions.

332 Finally, analogously to the quarks, the electroweak gauge bosons mix to give rise to  
 333 the physical charged- and neutral-current interaction bosons:

$$W^\pm = \frac{1}{\sqrt{2}} (W^1 \mp iW^2) , \quad (2.3)$$

$$\begin{pmatrix} \gamma \\ Z \end{pmatrix} = \begin{pmatrix} \cos(\theta_W) & \sin(\theta_W) \\ -\sin(\theta_W) & \cos(\theta_W) \end{pmatrix} \begin{pmatrix} B \\ W^3 \end{pmatrix} , \quad (2.4)$$

334 where  $\theta_W$  is the Weinberg angle.

## 335 2.2 The Higgs mechanism

336 If one writes down the most general, renormalizable Lagrangian for the model above,  
 337 two problems appear:

- 338 • the usual Dirac mass terms one can introduce in the fermionic sector are not  
 339 invariant under  $SU(2)_L$ ,
- 340 • mass terms for the  $W^\pm, Z$  bosons are not gauge-invariant.

341 So, in order to generate masses for the aforementioned particles, an external contrap-  
 342 tion is needed. The Brout-Englert-Higgs [27–29] mechanism proposed in 1964 introduces  
 343 a new spin-0 fundamental  $SU(2)_L$  doublet, called the Higgs field:

$$\phi(x) = \begin{pmatrix} \phi^+(x) \\ \phi^0(x) \end{pmatrix}. \quad (2.5)$$

344 It is colorless, and is charged under the electroweak  $U(1)_Y$  symmetry. The  $SU(3)_C \times$   
 345  $SU(2)_L \times U(1)_Y$  Lagrangian gets completed by a (gauged) Higgs sector, where the  
 346 covariant derivative  $D_\mu$  is given by Eq. (2.1):

$$\mathcal{L}_h = (D_\mu \phi)^\dagger (D^\mu \phi) + V(\phi) \quad (2.6)$$

$$= (D_\mu \phi)^\dagger (D^\mu \phi) + \mu^2 \phi^\dagger \phi - \lambda (\phi^\dagger \phi)^2, \quad \lambda > 0. \quad (2.7)$$

347 Similarly to the case of superconductivity [30], the underlying  $SU(2)_L \times U(1)_Y$  sym-  
 348 metry can be spontaneously broken if the Higgs potential  $V(\phi)$  has a non-zero ground  
 349 state. This is the case for the *Mexican-hat* potential given above, which is pictured in  
 350 Fig. 2.2. When the Higgs field assumes one of the degenerate ground states with a vac-  
 351 uum expectation value at the minimum of the potential around  $v = \mu/\sqrt{\lambda} \sim 246$  GeV,  
 352 it spontaneously breaks the  $SU(2)_L \times U(1)_Y$  symmetry of the Lagrangian.

353 Expanding the Higgs field from Eq. (2.5) around the vacuum and taking the EW  
 354 covariant derivative from Eq. (2.1),

$$\phi(x) = \frac{1}{\sqrt{2}} \begin{pmatrix} 0 \\ v + h(x) \end{pmatrix}, \quad (2.8)$$

$$D_\mu \phi(x) = \frac{1}{\sqrt{2}} \begin{pmatrix} -\frac{ig}{2} (W_\mu^1 - iW_\mu^2) (v + h(x)) \\ \partial_\mu h(x) - \frac{i}{2} (g'B_\mu - gW_\mu^3) (v + h(x)) \end{pmatrix}, \quad (2.9)$$

355 the Higgs field naturally couples to the gauge bosons. Then, computing the squared  
 356 gauged kinematic term of the spontaneously broken Higgs field from Eq. (2.7), and  
 357 replacing the gauge fields with their physical rotated states from Eqs. (2.3), (2.4) gives:

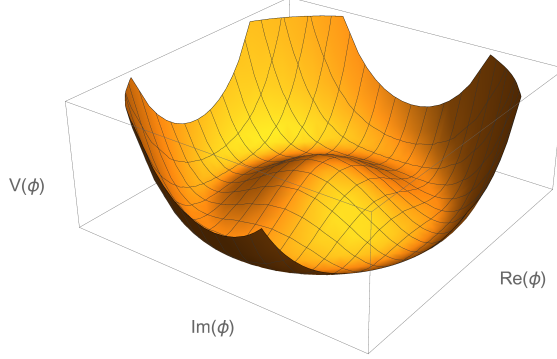


**Figure 2.2:** The  $SU(2) \times U(1)$  symmetric Higgs Mexican-hat potential has a degenerate non-zero ground state at  $v^2 = \langle \phi_0^\dagger \phi_0 \rangle \sim (246 \text{ GeV})^2$ .

$$\begin{aligned} \mathcal{L} \supset & \frac{1}{2} (\partial_\mu h)(\partial^\mu h) + \underbrace{\frac{g^2 v^2}{4}}_{m_W^2} W_\mu^+ W^{-\mu} + \frac{1}{2} \underbrace{\left( \frac{(g^2 + g'^2)v^2}{4} \right)}_{m_Z^2} Z_\mu Z^\mu \\ & + \underbrace{\frac{1}{2} (2\lambda v^2)}_{m_h^2} h^2 + \lambda v h^3 + \frac{\lambda}{8} h^4. \end{aligned} \quad (2.10)$$

358 So, the dynamic EW spontaneous symmetry breaking (EWSB) of the Higgs potential  
 359 generates masses for the  $W^\pm$ ,  $Z$  gauge bosons and identifying the mass terms in the  
 360 Lagrangian leads to the following leading-order boson mass relations<sup>1</sup>:

$$\begin{aligned} m_H &= \sqrt{2\lambda}v, \\ m_W &= \frac{gv}{2}, & \cos(\theta_W) &= \frac{g}{\sqrt{g^2 + g'^2}}, \\ m_Z &= \frac{\sqrt{g^2 + g'^2}v}{2}, & \sin(\theta_W) &= \frac{g'}{\sqrt{g^2 + g'^2}}. \\ m_\gamma &= 0, \end{aligned}$$

362 The  $W$  and  $Z$  boson masses are related (at tree-level):

$$m_W = m_Z \cos(\theta_W),$$

363 with the experimentally measured values  $m_W = 80.385 \text{ GeV}$ ,  $m_Z = 91.1876 \text{ GeV}$  and  
 364 the Weinberg angle  $\theta_W = 0.2223$ . Finally, considering the last two terms in Eq. (2.10),  
 365 the Higgs couples to itself to produce the Feynman diagrams shown in Fig. 2.3.

---

<sup>1</sup>The introduction of the Higgs mechanism also allows for a fermionic gauge-invariant mass term, e.g. by the Yukawa coupling of fermions to the Higgs boson  $\mathcal{L} \supset \frac{m_f}{2v} \bar{\psi}_f \psi_f h \xrightarrow{(h \rightarrow v)} \frac{1}{2} m_f \bar{\psi}_f \psi_f$ .

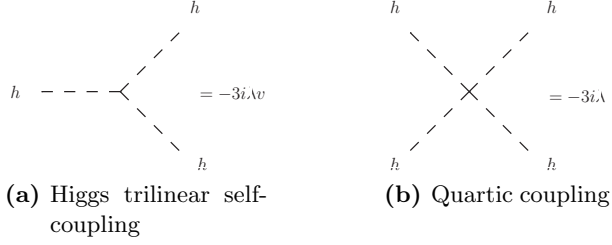


**Figure 2.3:** The physical Higgs field couples to itself after EWSB. The Feynman rules are given for (a) the triple vertex and (b) the quartic vertex.

366 As a side note, expressing Eq. (2.5) with all available degrees of freedom would give,  
367 in polar coordinates,

$$\phi(x) = \frac{v + h(x)}{\sqrt{2}} e^{\frac{i}{v} \chi_a(x) \sigma^a} \begin{pmatrix} 0 \\ 1 \end{pmatrix}, \quad (2.11)$$

368 where the three fields  $\chi_a$  are the massless Goldstone bosons associated with the EWSB  
369 of  $SU(2) \times U(1)$ . Because they will anyhow disappear from the theory (their respective  
370 degrees of freedom are sacrificed to the  $W$  and  $Z$  boson longitudinal polarizations), we  
371 do not explicitly consider them in the following. Combining the matter and gauge terms  
372 with the Higgs sector yields the final form of the SM Lagrangian:

$$\begin{aligned} \mathcal{L}_{\text{SM}} = & -\frac{1}{2} \langle G_{\mu\nu} G^{\mu\nu} \rangle - \frac{1}{2} \langle W_{\mu\nu} W^{\mu\nu} \rangle - \frac{1}{4} B_{\mu\nu} B^{\mu\nu} \\ & + \sum_{\psi=q_L,l_L,q_R,l_R} \bar{\psi} i \not{D} \psi + \text{h.c.} \\ & + Y_l \bar{\psi}_L \phi \psi_R + Y_d \bar{q}_L \phi d_R + Y_u \bar{q}_L \phi u_R + \text{h.c.} \\ & + (D_\mu \phi)^\dagger (D^\mu \phi) + \mu^2 \phi^\dagger \phi - \lambda (\phi^\dagger \phi)^2, \end{aligned} \quad (2.12)$$

373 where  $\langle \cdot \rangle$  represents the trace. The first line contains the field-strength tensors of  
374 the corresponding gauge bosons, e.g. for a gauge group with structure functions  $f^{abc}$   
375 defined by the generators  $[T_a, T_b] =: i f^{abc} T_c$  of the corresponding Lie algebra, and general  
376 coupling strength  $\tilde{g}$ :

$$F_{\mu\nu}^a = \partial_\mu A_\nu^a - \partial_\nu A_\mu^a + \tilde{g} f^{abc} A_\mu^b A_\nu^c.$$

<sup>377</sup> For the three SM subgroups:

- $SU(3)_C$ 
  - $A_\mu^a := G_\mu^a$  the gluon field in the adjoint representation,
  - $\tilde{g} := g_s$  the strong coupling constant,
  - $[T_a, T_b] =: if^{abc}T_c$  with the generators given in Eq. (2.2).
  
- $SU(2)_L$ 
  - $A_\mu^a := W_\mu^a$  the gauge field defined in Eq. (2.1),
  - $\tilde{g} := g$  the  $SU(2)_L$  coupling constant,
  - $[\sigma_a, \sigma_b] =: 2i\epsilon_{abc}\sigma_c$  with the Pauli matrices  $\sigma_i$  and the Levi-Civita symbol  $\epsilon_{abc}$ .
  
- $U(1)_Y$ 
  - $A_\mu^a := B_\mu$  the last gauge field appearing in Eq. (2.1),
  - $\tilde{g} := g'$  the  $U(1)_Y$  coupling constant,
  - $f^{abc} = 0$  since the group is Abelian.

<sup>380</sup> The second line of the SM Lagrangian in Eq. (2.12) contains the kinetic and interaction  
<sup>381</sup> terms for the fermion fields, where  $\not{D} = \gamma^\mu \partial_\mu$ . The third line contains the Yukawa  
<sup>382</sup> interaction of all fermions with the Higgs boson for mass generation, and the last line is  
<sup>383</sup> the unbroken SM Higgs boson sector.

<sup>384</sup> The addition of just one Higgs doublet to the SM, like in Eq. (2.5), is a minimal  
<sup>385</sup> choice. One could legitimately introduce further Higgs fields, as in the two-Higgs doublet  
<sup>386</sup> model (2HDM) [31] or the Minimal Supersymmetric SM (MSSM) [32], which predict  
<sup>387</sup> five physical scalar Higgs particles and which can assimilate the discovered Higgs boson  
<sup>388</sup> at  $m_h = 125$  GeV. These extensions of the SM predict in general different coupling  
<sup>389</sup> strengths of the Higgs boson(s) to other particles and to itself, and precise experimental  
<sup>390</sup> measurements of these couplings (and of the Higgs decay branching ratios) are needed  
<sup>391</sup> in order to differentiate between models.

## <sup>392</sup> 2.3 Top-Higgs interactions

<sup>393</sup> Intrinsically, the top-quark is tightly linked to the Higgs boson properties and has generally  
<sup>394</sup> strong phenomenological implications for the Higgs sector. Because it is the heaviest SM  
<sup>395</sup> elementary particle, and since the Yukawa coupling of the Higgs boson to fermions is proportional to their masses, the Higgs couples strongest to the top-quark  
<sup>396</sup> (in comparison, bottom-quark effects in inclusive Higgs observables are of the order of  
<sup>397</sup>  $m_b/m_t = 2.8\%$ ). It is especially important for Higgs production at the LHC: the pre-  
<sup>398</sup> dominant production mechanism is gluon-fusion via a triangle top-quark loop, as shown  
<sup>399</sup> in Fig. 2.4. In comparison, other associated production modes have cross-sections that  
<sup>400</sup> are more than one order of magnitude smaller. The Feynman diagrams for the main  
<sup>401</sup> production channels at LHC are also depicted in Fig. 2.5.

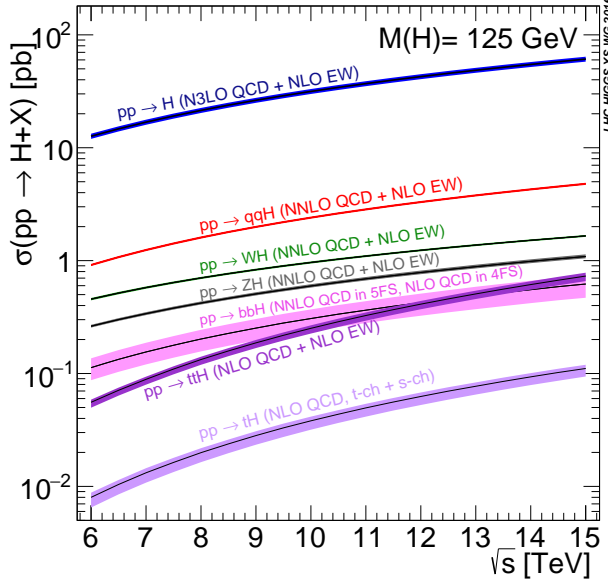


**Figure 2.4:** Theory prediction for  $pp \rightarrow h + X$  production cross-sections as a function of the center-of-mass energy  $\sqrt{s}$ . Single Higgs production at the LHC is dominated by gluon fusion mediated by a top-quark loop. Figure taken from Ref. [33].

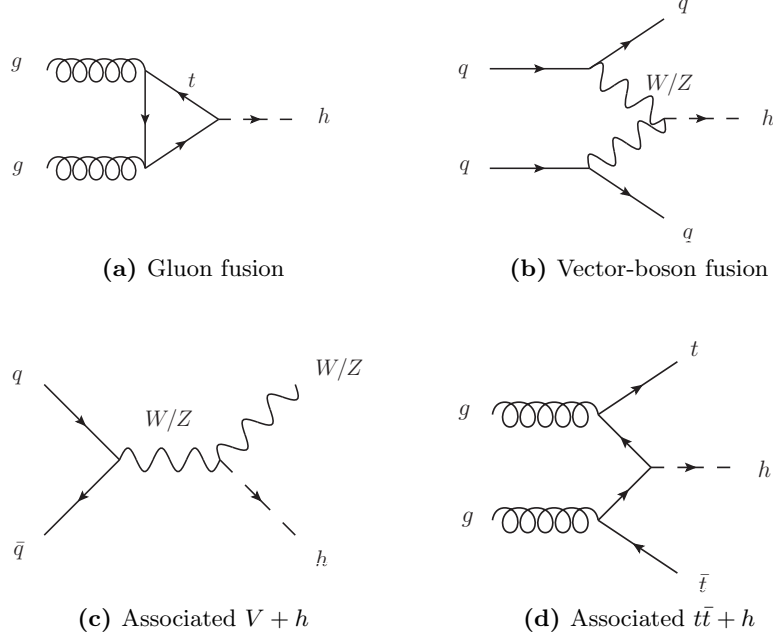


**Figure 2.5:** Leading-order diagrams for Higgs production by (a) gluon fusion, (b) vector-boson fusion, (c) associated vector production and (d) associated  $t\bar{t}$  production.

### 2.3 Top-Higgs interactions

In relation to both the measurement of the Higgs triple self-coupling and the importance of top-mass effects in Higgs production, the reader is referred to the extensive discussion laid out in Chapter 10. Not only do top-quarks influence Higgs process cross-sections at collider experiments, but they also have a deeper connection to the Higgs potential. Indeed, the  $\beta$ -function of the Higgs quartic coupling (which governs the evolution of the coupling's value at different resolution scales, see Chapter 3) is sensitive to renormalization counterterms stemming from top-quark loops.

Eq. (2.13) gives the one-loop  $\beta$ -function for the Higgs quartic coupling [34]:

$$\mu^2 \frac{d\lambda}{d\mu^2} = \beta_\lambda(\lambda, y_t, g_s, \dots) = \frac{1}{16\pi^2} (12\lambda^2 + 6\lambda y_t^2 - 3y_t^4), \quad y_t = \sqrt{2} \frac{m_t}{v} \sim 1 \quad (2.13)$$

where  $y_t$  is the top-Yukawa coupling and is proportional to the top-quark mass  $m_t$ .

Because the top-Yukawa coupling is of order  $\mathcal{O}(1)$ , small variations in the value of the top-quark mass modify the evolution of the Higgs quartic coupling  $\lambda$  in a non-trivial way. If  $\lambda(\mu)$  was to become negative at scales much below the Planck scale,  $M_P \sim 10^{18} - 10^{19}$  GeV (see Fig. 2.6a), the Higgs field could tunnel from the current false vacuum state to the true, absolutely stable vacuum ground state. Current measurements seem to support the fact that the SM is in a metastable state, as shown in Fig. 2.6b. For the existentially anxious reader, a state-of-the art calculation of the EW vacuum decay rate can be found in Ref. [35].

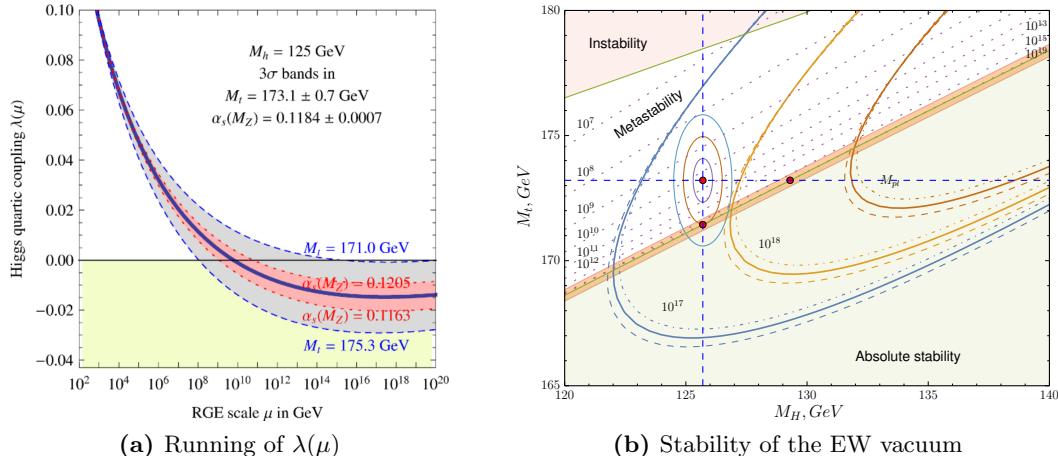


**Figure 2.6:** (a) The evolution of the Higgs quartic coupling  $\lambda$  can lead to negative values at high energy scales (below the Planck scale  $M_P$ ). This in turn makes the EW vacuum potentially unstable. The running is highly dependent on the top-quark mass and  $\alpha_s$  values [36]. (b) The SM point, in red, is plotted in the  $(m_h, m_t)$  phase-space with  $1-, 2-$  and  $3\sigma$  uncertainties. The pink dotted lines indicate contours where  $\lambda(\mu) = 0$  for the indicated values of  $\mu$ , and the parabolic curves where the beta-function  $\beta_\lambda(\mu) = 0$  for chosen values of  $\mu$ . The measured Higgs and top-quark masses point to a SM universe close to the metastable region [37].

## 420 2.4 Outstanding issues with the Standard Model

421 For all its successes, the SM is known to have some theoretical flaws. Below is a list of  
 422 familiar shortcomings:

- 423 • **Massless neutrinos:** In the SM, neutrinos are naturally massless. Experi-  
 424 ments [20] have shown that neutrinos can oscillate between the different families,  
 425 and this requires a mixing of flavor states with mass eigenstates, similarly to the  
 426 CKM mixing. Different mechanisms [38–40] were introduced to generate neutrino  
 427 masses: a right-handed (so-called *sterile*) neutrino could exist, and not interact  
 428 with matter (no right-handed neutrino was ever observed), or neutrinos could ac-  
 429 quire a Majorana mass. Some R-parity violating supersymmetric (SUSY) models  
 430 also produce neutrino masses [41, 42].
- 431 • **Gravity:** General relativity has yet to be quantized and incorporated into the SM  
 432 under its current form, and a unified theory of all four interactions is still missing.  
 433 As a first attempt, an exchange gravitational gauge boson can be introduced under  
 434 the form of a spin-2 particle, called the graviton. The addition of corresponding  
 435 terms to the SM Lagrangian spawns the apparition of UV divergences that cannot  
 436 be handled by a finite number of counterterms [43–45], though, and the theory is  
 437 not perturbatively renormalizable.
- 438 • **Dark matter:** The presence of dark matter in the Universe has been suggested  
 439 from multiple cosmological observations [46–50]. Yet, the SM does not contain a  
 440 good dark matter candidate particle. Some extensions of the SM, in particular  
 441 SUSY, provide a heavy non-decaying particle (the lightest in the SUSY spectrum,  
 442 called light supersymmetric particle (LSP)) that turns out to be a good candidate.
- 443 • **Baryon asymmetry:** The SM predicts that matter and antimatter should have  
 444 been produced almost symmetrically at the Big Bang. Yet baryons are observed  
 445 to be in overwhelming excess over antibaryons in our part of the Universe [51, 52].
- 446 • **Hierarchy problem:** There is a manifest imbalance between the three unified  
 447 forces of the SM and gravity, or between their respective mass scales. In particular,  
 448 it is not clear why the Higgs boson mass is so small with respect to the Planck scale:  
 449 basically, radiative corrections to the Higgs self-energy should blow up its mass, and  
 450 the observed value of  $m_h = 125$  GeV requires an incredible amount of fine-tuning to  
 451 cancel radiative corrections. Again, SUSY models solve this problem by requiring  
 452 every SM particle to have a supersymmetric partner which has the opposite spin-  
 453 statistics: their contributions to the Higgs mass then cancel naturally [53].

454 Although all model extensions of the SM have respective advantages over the current  
 455 theory, none of the particles predicted by them has been observed at the LHC or any  
 456 other experiment yet.

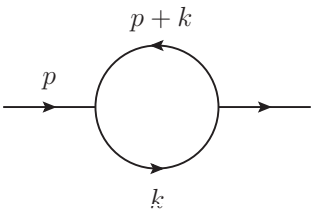
# 457 3 Higher-order perturbative calculations in 458 hadron-hadron collisions

459 The SM Lagrangian presented in the last Chapter provides the Feynman rules to com-  
460 pute theoretical cross-sections. As will be explained in Section 3.1.3, the scattering  
461 amplitudes (at high-energies, for QCD) can be expanded to a perturbative series in the  
462 coupling constant: the interactions are represented by Feynman diagrams, and higher-  
463 order corrections generate loop diagrams that are most of the time divergent. Since  
464 the first successes of QFT in predicting basic energy spectrum properties and leading-  
465 order (LO) scattering amplitudes, there has always been a need for a more consistent  
466 framework in which higher-order corrections could be worked out. In this Chapter, we  
467 summarize the important ingredients used in most theoretical computations nowadays,  
468 in particular in the context of high-energy hadron-hadron collisions. Most of the tradi-  
469 tional content presented here is adapted from Refs. [54–58].

## 470 3.1 Divergences in Quantum-Field Theory

471 Going beyond Feynman tree diagrams in the computation of scattering matrix-elements,  
472 one encounters two classes of divergences. Consider a one-loop scalar massless two-point  
473 function, where the internal loop-momentum is integrated over:

474



$$I_2(p^2; 0, 0) = \int_{-\infty}^{\infty} \frac{d^4 k}{(2\pi)^4} \frac{1}{(k^2 + i\delta)((p+k)^2 + i\delta)} . \quad (3.1)$$

475 In the limit  $|k| \rightarrow \infty$ , the integral behaves as  $I \propto \int \frac{dk k^3}{k^2 \cdot k^2} = \int \frac{dk}{k}$  which is logarithmi-  
476 cally divergent. The integral is also divergent when taking the limit  $k \rightarrow 0$ . These are  
477 called *ultraviolet*, respectively *infrared* divergences.

478 As a solution to the infinities conundrum, the above integral has to be treated by the  
479 introduction of a UV cutoff of some kind – this is a method called *regularization*, and  
480 by absorbing the regularized infinities in a consistent way through the *renormalization*  
481 of the Lagrangian bare couplings and masses.

### 482 3.1.1 Regularization

483 A first attempt at controlling UV divergences consists in the introduction of a high-  
484 momentum regulator  $k^2 < \Lambda^2$ . Then, the loop integral given in Eq. (3.1) behaves as

$$I_2(p^2; 0, 0) \propto \int_{\epsilon}^{\Lambda} \frac{dk}{k} \sim \log(\Lambda) , \quad (3.2)$$

and the integral diverges logarithmically in the cutoff  $\Lambda$ . This is typical of renormalizable theories. Now, obviously, any physical observable should not depend on the value of the arbitrary cutoff, and in practice it does not.<sup>1</sup> As a theoretical downside, the introduction of the cutoff breaks gauge-invariance. It also breaks translational invariance and makes it difficult to use Feynman parameters and the corresponding variable replacements  $p \rightarrow p + k$ .

A possible gauge-invariant regularization method is the so-called Pauli-Villars regularization: a much more massive particle is introduced and its contribution subtracted from the ordinary propagator, that is:

$$\int \frac{d^4k}{(2\pi)^4} \frac{1}{k^2 + i\delta} \rightarrow \int \frac{d^4k}{(2\pi)^4} \left( \frac{1}{k^2 + i\delta} - \frac{1}{k^2 - M^2 + i\delta} \right) . \quad (3.3)$$

The Pauli-Villars technique cannot be applied to QCD because it is not gauge-covariant, though. On the same stance, it introduces an unphysical field that violates the spin-statistics theorem (it amounts to a spurious scalar field with Fermi statistics). One of the preferred regularization methods nowadays is dimensional regularization. It was refined by 't Hooft and Veltman [60] to regularize any integral, is gauge-invariant and works for non-Abelian theories as well. The governing idea is that quantum-field theories in a smaller number of dimensions have a lesser superficial degree of divergence. The four dimensions of space-time are therefore analytically continued to  $d = 4 - 2\epsilon$  dimensions, and the integral in Eq. (3.1) can be cast into the following form:

$$I_2(p^2; 0, 0) = \mu^{2\epsilon} \int \frac{d^d k}{(2\pi)^d} \frac{1}{(k^2 + i\delta)((p+k)^2 + i\delta)} , \quad (3.4)$$

where the renormalization scale  $\mu$  is a dimensionful parameter needed to keep the integral dimensionless. Then the integral can be worked out by introducing Feynman parameters and Wick-rotating to give the analytical result

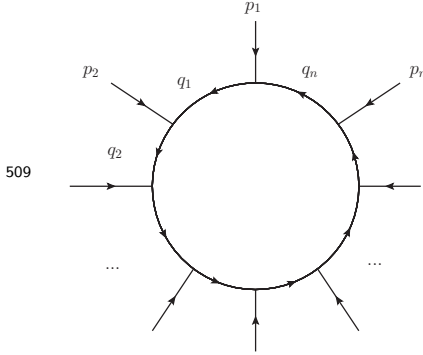
$$I_2(p^2; 0, 0) = \frac{1}{\epsilon} + \ln \frac{\mu^2}{-p^2 - i\delta} + 2 + \mathcal{O}(\epsilon) , \quad (3.5)$$

where the UV divergences now appear as (at most double, at one-loop) poles in the dimensional regulator  $\epsilon$ . A general dimensionally-regularized one-loop scalar integral with  $n$  external legs has the form:

---

<sup>1</sup>For a fun exercise of trying out different forms of cutoff (Gaussian, Dirac-delta,...), see Ref. [54] for the case of the vacuum polarization in the Casimir effect [59].

### 3.1 Divergences in Quantum-Field Theory



$$I = \mu^{n-d/2} \int \frac{d^d k}{(2\pi)^d} \prod_{j=1}^n \frac{1}{(q_j^2 - m_j^2 + i\delta)}, \quad (3.6)$$

510 where the internal momenta  $q_j = k + \sum_{i=1}^j p_i$  are expressed as a linear combination of  
 511 the loop momentum  $k$  and the external momenta  $p_i$ . Systematic Feynman parameters  
 512 can be found for the integral above, and generally it can be recast into the form

$$I = \Gamma(n - d/2) \prod_{i=1}^n \int_{0 \leq x_i \leq 1} dx_i \delta \left( 1 - \sum_{j=1}^n x_j \right) \frac{\mathcal{U}^{n-d}(\vec{x})}{\mathcal{F}^{n-d/2}(\vec{x}, p_i \cdot p_j, m_i^2)}. \quad (3.7)$$

513 The  $x_1, \dots, x_n$  are the Feynman parameters, and  $\mathcal{U}$ ,  $\mathcal{F}$  are the first, respectively  
 514 second Symanzik polynomials.<sup>2</sup> Then, one needs only perform the integration over the  
 515 Feynman parameters. Most importantly, all one-loop integrals can be reduced to a linear  
 516 combination of a set of *master integrals* that are at most box-diagrams, which are all  
 517 known analytically and implemented in integral libraries. Finally, for tensor integrals  
 518 where the numerator of Eq. (3.6) contains Lorentz indices, there exist methods for their  
 519 reduction to a set of scalar integrals, like the systematic Passarino-Veltman method [61]  
 520 which uses a form factor expansion to factorize the indices. For the interested reader,  
 521 Refs. [62–66] supply a comprehensive examination of various techniques for reducing and  
 522 evaluating Feynman integrals.

523 Dimensional regularization has lots of benefits, and the algebra is quite straightforward.  
 524 Its major disadvantage is that the Dirac algebra for fermions has to be analytically  
 525 extended to  $d = 4 - 2\epsilon$  space-time dimensions as well, which is not trivial. The Dirac  
 526 matrices can be made to obey an analytically continued Clifford algebra

$$\{\gamma^\mu, \gamma^\nu\} = 2g^{\mu\nu}, \quad (3.8)$$

527 with a  $d$ -dimensional metric,  $g^{\mu\nu}g_{\mu\nu} = d$ , where it is but unclear what happens to the  
 528 last Dirac matrix  $\gamma_5 = i\gamma_0\gamma_1\gamma_2\gamma_3$ . The different ways of treating  $\gamma_5$  and the helicities of  
 529 external and internal particle fields lead to different regularization schemes. Note that  
 530 physical observables do not depend on the chosen scheme. In the dimensional reduction  
 531 scheme (DRED) which we use for the predictions given in Chapters 6–11, the Dirac  
 532 algebra is left to  $d = 4$  dimensions, and the same holds for all external momenta and  
 533 helicities. Only the internal momenta are analytically continued to  $d$ -dimensions.

---

<sup>2</sup>Eq. (3.7) can also be generalized to a Feynman integral for  $l$  loops,  $n$  external and  $m$  internal momenta

534 **3.1.2 Renormalization**

535 As a way to treat the infinities arising from the UV region of integration, the bare param-  
 536 eters of the Lagrangian are redefined to absorb the divergent contributions. Although  
 537 this seems mathematically shaky, it is remarkable that the redefinition of a finite number  
 538 of parameters allows for the treatment of divergences order-by-order and for all Feynman  
 539 diagrams contributing to the amplitude of a renormalizable theory. In practice, renor-  
 540 malization of the Lagrangian is achieved by rewriting the bare masses and couplings  $m_0$   
 541 and  $g_0$ , as well as the fields themselves  $\psi_0$ , as a physical (measurable) parameter and a  
 542 counterterm

$$\begin{aligned} m_0 &= Z_m m = m + \delta m , \\ g_0 &= Z_g g = g + \delta g , \\ \psi_0 &= \sqrt{Z} \psi . \end{aligned} \tag{3.9}$$

543 The only requirement is that diagrams corresponding to the counterterms should can-  
 544 cel UV divergences stemming from the bare Lagrangian. In principle, the procedure does  
 545 not define how to handle the finite terms accompanying these diagrams: depending on  
 546 the additional criteria, several renormalization schemes can be chosen (on-shell, MS, MS,  
 547 or others). Here as well, the physical observables should be independent of the choice  
 548 of scheme (the top-quark mass is a fringe example and will be discussed summarily in  
 549 Chapter 6).

550 The physical parameters entering the Lagrangian, e.g. the masses and couplings  $m, g$ ,  
 551 have to be determined by experiment. By definition, they are measured at a given energy  
 552 scale. Colloquially, a renormalization starting point is chosen: the couplings/masses are  
 553 then said to *run* with the scale at which they are defined. Notably, the renormalized  
 554 field theory runs according to the Callan-Symanzik [67–69] equation, which governs the  
 555 dependence of the  $n$ -point correlation functions on the model's parameters by asking  
 556 that the bare Green's functions  $G_0^{(n)}(x_1, \dots, x_n; m_0, g_0)$  do not depend on the variations  
 557 given in Eq. (3.9):

$$\left( m \frac{\partial}{\partial m} + \beta(g) \frac{\partial}{\partial g} + n\gamma \right) G^{(n)}(x_1, \dots, x_n; m, g) = 0 , \tag{3.10}$$

558 where the  $\beta$ -function of the theory is defined as  $\beta(g) = \frac{m}{\delta m} \delta g$ , and the anomalous  
 559 dimension is given by  $\gamma = \frac{m}{\delta m} \frac{\delta \sqrt{Z}}{\sqrt{Z}}$ . Eq. (3.10) is an example of a broad class of evolution  
 560 equations called renormalization group equations (RGE).

561 **3.1.3 Perturbative expansion of Quantum Chromodynamics**

562 From the running of the strong coupling constant given by the QCD  $\beta$ -function,

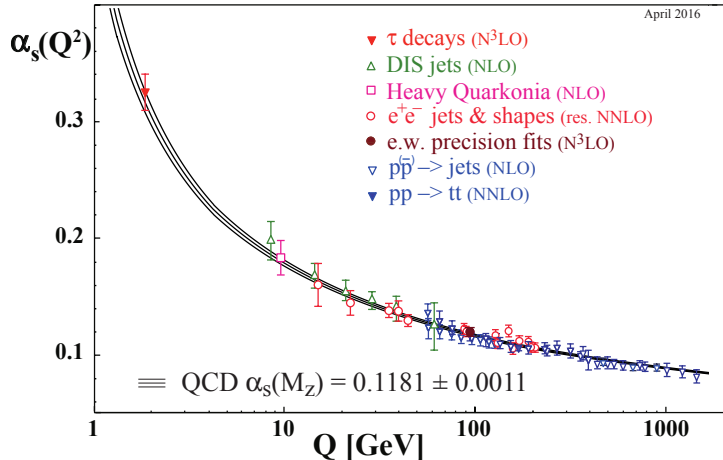
$$\mu_R^2 \frac{\partial \alpha_s}{\partial \mu_R^2} = \beta(\alpha_s) = - (b_0 \alpha_s^2 + b_1 \alpha_s^3 + \dots) , \tag{3.11}$$

### 3.1 Divergences in Quantum-Field Theory

one sees that because of the negative sign in Eq. (3.11), the strong coupling  $\alpha_s(\mu_R^2)$  becomes smaller at higher scales  $\mu_R^2$ . This running is manifest in Fig. 3.1, which shows measurements of the strong coupling  $\alpha_s$  at different energy scales  $Q$ , in agreement with the QCD theory prediction. Thus, with the measured value of the strong coupling at intermediate scales  $\alpha_s(M_Z) \approx 0.118$ , the interactions at high-energy hadron colliders can be treated perturbatively in  $\alpha_s$ . For any process cross-section  $\sigma_{ab \rightarrow X}$ , where  $a, b$ , and  $X$  are freely propagating initial-, respectively final-states, one can expand the cross-section in a Taylor series,

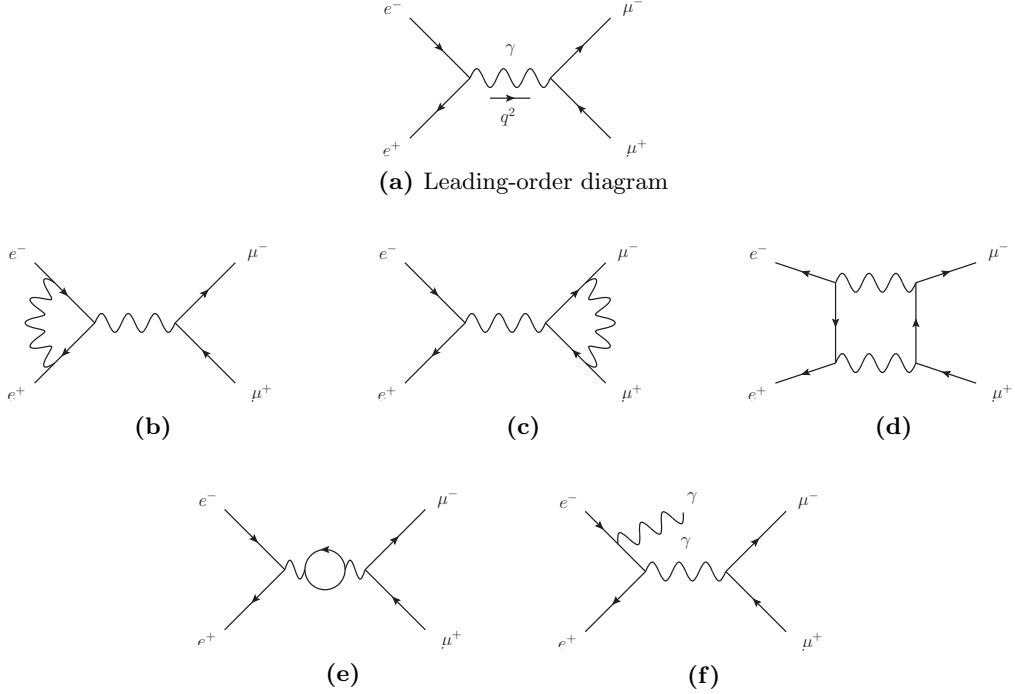
$$\hat{\sigma}_{ab \rightarrow X} = \alpha_s^k(\mu_R^2) (\hat{\sigma}_{\text{LO}}(p_i, p_f; \mu_R^2) + \alpha_s(\mu_R^2) \hat{\sigma}_{\text{NLO}}(p_i, p_f; \mu_R^2) + \mathcal{O}(\alpha_s^2(\mu_R^2)) + \dots) \quad (3.12)$$

At each order in the strong coupling  $\alpha_s$ , the cross-section can be computed and will depend on the choice of the renormalization scale. Usually it is chosen close to the expected momentum exchange  $Q^2$ . The systematic uncertainty related to the arbitrary choice of the scale is then estimated by varying the renormalization scale by factors of  $\frac{1}{2}$  and 2.



**Figure 3.1:** Various measurements of the strong coupling  $\alpha_s(Q^2)$  at different energy scales  $Q$  show the running behavior typical of QCD, with a coupling strength that becomes smaller at higher energies, and a Landau pole at the hadronization scale  $Q = \Lambda \sim 1 \text{ GeV}$ . Figure taken from Ref. [1].

The accuracy of a computation is given by the truncation order of the perturbative series in Eq. (3.12). In certain regions of phase-space, though, large prefactors can be introduced at all orders, when two far-away scales  $Q$  and  $q$  are involved. This usually spawns the appearance of large logarithms of the form  $\ln^n(Q^2/q^2)$ , which have to be resummed to a given *logarithmic* accuracy across all orders. Some details will be given in Section 4.2.

582 **3.2 Infrared divergences**


**Figure 3.2:** Feynman diagrams for  $e^+e^- \rightarrow \mu^+\mu^-$ . (a) The only leading-order diagram, with a photon in the  $s$ -channel (b-e) Virtual one-loop corrections. (f) Real-emission diagram

583 Starting from an example, let us consider the case of QED higher-order corrections to  
 584  $e^+e^- \rightarrow \mu^+\mu^-$  annihilation. Feynman diagrams up to  $\mathcal{O}(\alpha^3)$  are shown in Fig. 3.2. At  
 585 leading-order, the cross-section is given by

$$\sigma_{\text{LO}} = \int_{\Phi} d\Phi |\mathcal{M}_0|^2 = \frac{4\pi\alpha^2}{3q^2}, \quad (3.13)$$

586 where the squared amplitude  $|\mathcal{M}_0|^2$  has to be integrated over the phase-space  $\Phi$ , and  
 587  $q^2$  is the momentum carried by the exchanged photon. Let us assume the UV divergences  
 588 have been handled by the introduction of appropriate counterterms. That is, the UV  
 589 divergences stemming from the loop momentum integration from diagrams (b) and (c)  
 590 in Fig. 3.2 have been taken care of by renormalizing the electron charge and the muon  
 591 charge, respectively. Diagram (e) is also UV divergent but is nothing else than vacuum  
 592 polarization in QED (thus, it has no impact on any observable), while diagram (d) has  
 593 no UV divergence. Computing the amplitude, one realizes there is also an IR divergence  
 594 coming from the massless photon propagator in the loops.

595 First, the IR divergence needs regularizing. The simplest way to do that is to give the  
 596 photon a small, non-zero mass,  $m_\gamma > 0$ , and to take the limit  $m_\gamma \rightarrow 0$  at the end of the

### 3.3 The factorization theorem

597 calculation. Computing the virtual contribution,  $\sigma_V \propto (\mathcal{M}_V^\dagger \mathcal{M}_0 + \text{h.c.})$ , one arrives  
 598 at the result

$$\sigma_V = \frac{2}{3} \pi^2 \frac{\alpha^3}{q^2} \left( \frac{\pi^2}{5} - \frac{7}{2} - \ln^2 \left( \frac{m_\gamma^2}{q^2} \right) - 3 \ln \left( \frac{m_\gamma^2}{q^2} \right) \right). \quad (3.14)$$

599 The IR divergence is still present but it is explicit in  $\ln(m_\gamma)$ .<sup>3</sup> For the perturbative  
 600 expansion to be consistent, we have to include real-emission diagrams of  $\mathcal{O}(\alpha^3)$ , that is  
 601 diagrams of the sort pictured in Fig. 3.2f, where a photon is radiated either from the  
 602 initial- or the final-state. Doing so, one gets a contribution of the form  $\sigma_R \propto |\mathcal{M}_R|^2$ :

$$\sigma_R = \frac{2}{3} \pi^2 \frac{\alpha^3}{q^2} \left( -\frac{\pi^2}{5} + 5 + \ln^2 \left( \frac{m_\gamma^2}{q^2} \right) + 3 \ln \left( \frac{m_\gamma^2}{q^2} \right) \right). \quad (3.15)$$

603 Combining the different contributions to the cross-section, the IR divergences can-  
 604 cel between the virtual one-loop and the real-emission matrix-elements to give a finite  
 605 correction to the leading-order cross-section:

$$\sigma_{\text{NLO}} = \sigma_{\text{LO}} + \sigma_V + \sigma_R = \sigma_{\text{LO}} \left( 1 + \frac{3}{4\pi} \alpha \right). \quad (3.16)$$

606 This behavior is symptomatic of IR divergences and falls under the purview of the  
 607 Kinoshita–Lee–Nauenberg (KLN) theorem, which states that sufficiently inclusive ob-  
 608 servables are always IR-finite.

609 Although the cancellation of IR divergences is ensured by the KLN theorem, it is  
 610 non-trivial to realize it numerically (for example in the context of a Monte-Carlo event  
 611 generator). Section 4.1.2 will briefly develop this point.

## 612 3.3 The factorization theorem

613 The collision of composite states like the protons used at LHC implies interactions of  
 614 highly non-perturbative objects. It is not clear at first how to handle these theoretically:  
 615 color confinement does not allow for free quarks or gluons to be observed, thus the  
 616 initial-state in hadron colliders cannot *a priori* be defined perturbatively. At high-energy,  
 617 though, we can make use of the fact that the interaction with the highest momentum  
 618 exchange takes place over time scales that are far smaller than the typical time scale at  
 619 which the proton's constituents interact among themselves. The description of such a  
 620 collision can therefore be *factorized* in long- and short-distance (or short- and long-time  
 621 scale) physics: a hard collision of two freely propagating partons, and non-perturbative  
 622 interactions within hadrons. Mathematically, the cross-section  $\sigma_{pp \rightarrow X}$  for the production  
 623 of a state  $X$  from the collision of two protons can be written as

---

<sup>3</sup>The divergent terms are called Sudakov double logarithms and are systemic of collinear/soft emission (see Chapter 4).

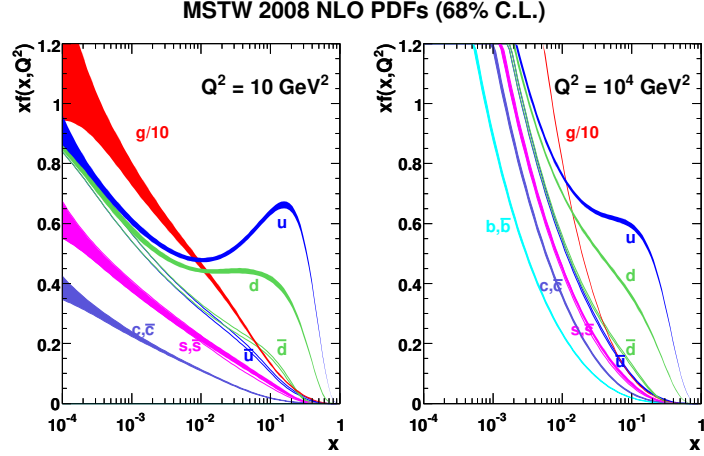


**Figure 3.3:** The MSTW 2008 NLO proton PDFs [70] as a function of the parent proton’s momentum fraction  $x$  at resolution scales  $Q^2 = 10 \text{ GeV}^2$  (left),  $Q^2 = 10^4 \text{ GeV}^2$  (right).

$$\sigma_{pp \rightarrow X} = \sum_{ab} \int dx_a f_{a/p}(x_a, \mu_F^2) \int dx_b f_{b/p}(x_b, \mu_F^2) \cdot \hat{\sigma}_{ab \rightarrow X}(x_a p_1, x_b p_2; \mu_F^2), \quad (3.17)$$

where  $a$  and  $b$  are possible constituents of the parent protons (sea or valence quarks and gluons),  $f_{a/p}$ ,  $f_{b/p}$  are encoding the non-perturbative origin of the partons in the parent protons, and  $\hat{\sigma}_{ab \rightarrow X}$  is the cross-section for the production of the final-state  $X$  from the collision of the free partons  $a$  and  $b$ , the latter of which can now be computed perturbatively in QCD. Eq. (3.17) is called the *factorization theorem* of Quantum Chromodynamics, and sets the basis for all cross-section predictions at LHC. The functions  $f_{a/p}$ ,  $f_{b/p}$ , which are called *parton distribution functions* (PDF), depend on the momentum fraction  $\xi_a$ ,  $\xi_b$  carried away by the parton from the parent proton, and on the resolution scale  $Q^2$ . Crudely said, the partonic content of the protons depends on the scale at which they are resolved.<sup>4</sup> The PDFs by definition cannot be computed perturbatively in QCD, but they can be measured from experimental data. As a matter of fact, a precise measurement of the proton’s PDF is crucial, and constitutes one of the main sources of uncertainty in theoretical predictions at the LHC. Fig. 3.3 depicts the measurement of the proton PDFs by the MSTW collaboration from a global fit of hard-scattering data [70].

---

<sup>4</sup>The PDFs also obey an evolution equation similar to the RGE called DGLAP equation: this evolution runs from a central scale choice, namely the *factorization scale*  $\mu_F$ .

## <sup>639</sup> 4 Monte-Carlo (MC) event generators

<sup>640</sup> To be able to compare a theory prediction for hadron colliders to an experimental mea-  
<sup>641</sup> surement released by e.g. the ATLAS experiment, theorists and experimentalists meet  
<sup>642</sup> on a common ground: the cross-section  $\sigma$ . The cross-section can be inclusive, and rep-  
<sup>643</sup> resents the total number of events for a given process after applying cuts and correcting  
<sup>644</sup> for the detector acceptance, or it can be a differential cross-section with respect to some  
<sup>645</sup> kinematic variable  $d\sigma/d\mathcal{O}$ , where  $\mathcal{O} = n_{\text{jets}}, m_{t\bar{t}}, \dots$  is any event observable. On one  
<sup>646</sup> side, the theorists need to compute a cross-section from a QFT starting point, namely  
<sup>647</sup> the Lagrangian: at the most basic level, this means implementing Fermi's golden rule  
<sup>648</sup> (Eq. (4.1)). On the other side, experimentalists have to count events and correct for  
<sup>649</sup> detector acceptance and resolution (Eq. (4.2)):

$$\sigma = \frac{1}{4E_a E_b v} \int \prod_f \left( \frac{d^3 p_f}{(2\pi)^3} \frac{1}{2E_f} \right) |\mathcal{M}_{fi}|^2 (2\pi)^4 \delta^4(p_a + p_b - \sum_f p_f), \quad (4.1)$$

$$\sigma = \frac{N_{\text{events}}}{\epsilon \cdot \mathcal{L}_{\text{int}}}, \quad (4.2)$$

<sup>650</sup> where  $E_a$  and  $E_b$  are the energies of the incoming particles  $a$  and  $b$ , the flux per unit  
<sup>651</sup> volume  $v = |\vec{v}_a - \vec{v}_b|$  is given by the relative 3-velocities of the particles and  $p_f, E_f$  are  
<sup>652</sup> the 3-momenta and energies of all final states. As a matter of fact, the infinitesimal  
<sup>653</sup> volume element above is relativistically invariant. Ultimately, the relativistic matrix-  
<sup>654</sup> element squared  $|\mathcal{M}_{fi}|^2$  has to be integrated over the whole phase-space while enforcing  
<sup>655</sup> 4-momentum conservation. Experimentally, in Eq. (4.2), the cross-section is equal to  
<sup>656</sup> the event count, corrected for phase-space acceptance, detector resolution and normal-  
<sup>657</sup> ized by the integrated luminosity  $\mathcal{L}_{\text{int}}$ . For the case of differential distributions, the  
<sup>658</sup> formula becomes more complicated, as binned events migrate depending on the detector  
<sup>659</sup> resolution. The discussion of this case is postponed to Chapter 8.

<sup>660</sup> There are two issues with the picture at hand. First, the matrix-element for a given  
<sup>661</sup> process can typically be computed only up to  $\mathcal{O}(\text{few})$  external legs. Because the mul-  
<sup>662</sup> tiplicity of final-state particles in a collider experiment like the LHC is of the order  
<sup>663</sup>  $\mathcal{O}(10^2 - 10^3)$ , it is virtually impossible to calculate such amplitudes. Second, the per-  
<sup>664</sup> turbative expansion presented in Chapter 3 breaks down when colored particles are  
<sup>665</sup> produced with small energies. In particular, around energy scales where free final-state  
<sup>666</sup> partons fall in the realm of non-perturbative interactions, they hadronize to form the  
<sup>667</sup> observable colorless bound states demanded by color confinement. Therefore, the struc-  
<sup>668</sup> ture of the whole collision has to be broken down into pieces across the several scales  
<sup>669</sup> involved, and the theoretical treatment of each piece is valid only in these subdomains  
<sup>670</sup> and subjected to different levels of approximation. The theory community developed

## 4 Monte-Carlo (MC) event generators

the necessary ingredients to improve the description of each stage and assembled them into mostly-automated programs called *Monte-Carlo (MC) event generators*.

MC event generators basically simulate the particle collisions as they would happen at the interaction points of an experiment like ATLAS or CMS. The MC program has to match multi-scale physics to simulate a collision, taking into account non-perturbative (PDF and quark fragmentation, hadron decay, underlying event, proton beam remnants) as well as perturbative (matrix-element and parton-shower matching) phenomena, as shown in Fig. 4.1.

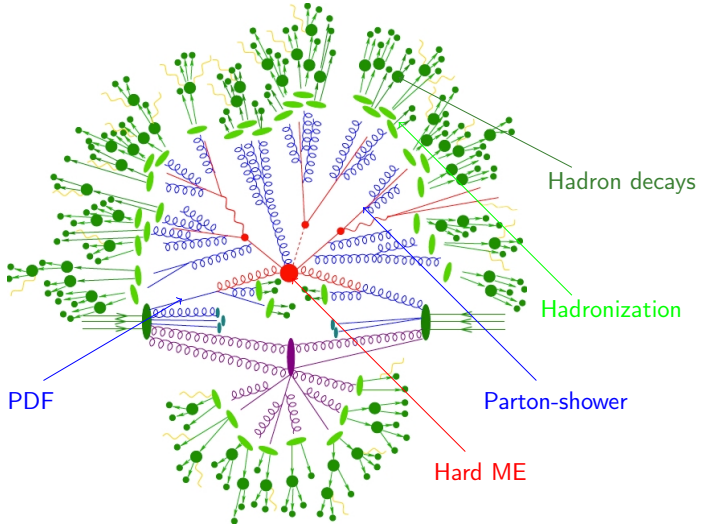


**Figure 4.1:** A typical MC event. Figure adapted from Ref. [71].

Under the hood of any Monte-Carlo program, the ingredients are essentially the same:

- **Monte-Carlo integrator:** The phase-space is sampled, usually with the help of an adaptive Monte-Carlo integration algorithm, to numerically perform the integral given in Eq. (4.1). As a notable example, the `Cuba` library [72] implements four multi-dimensional integration algorithms: `Vegas` [73], `Divonne` [74], `Suave` [72, 75] and `Cuhre` [76].
- **PDFs:** There is an extensive amount of PDF measurements varying in the used datasets, theoretical precision, combination strategy, handling of  $\alpha_s$ , or flavour thresholds. The `LHAPDF 6` package [77] interpolates PDF values from discrete measurement points in the  $(x, Q^2)$  phase-space and can be interfaced to the MC generator.

- **Hard matrix-element:** The core of the calculation is the computation of the matrix-element  $\mathcal{M}_{fi}$ . It determines the theoretical accuracy of the prediction to a given order in  $\alpha_s$ . More details are given in Sec. 4.1.
- **Parton shower:** As stated above, the high-multiplicity final-state is evolved from the few-parton hard matrix-element through subsequent radiative emission by a parton-shower algorithm. These routines base on first-principles QCD (and QED), but contain inherent approximations and parametric degrees of freedom that generate an uncertainty associated with the choice of algorithm. Section 4.2 will expand on the topic.
- **Hadronization and hadron decay:** Once the shower evolution is brought down to energies of the order of the hadronization scale (of order  $\mathcal{O}(1 \text{ GeV})$ ), the free partons bind to form colorless states. This is handled by a model on the only assumption that it should describe data to the best possible extent. Commonly, these models have a certain number of free parameters that are *tuned* to data. In Sec. 4.3, the Lund string and the cluster model are briefly detailed.
- **Multiple partonic interaction and underlying event:** Especially at small momentum fractions, it is possible that more than one parton from the same parent proton contribute to the interaction. The description of this phenomenon is also mostly based on MC modeling and has to be tuned to experimental data.

## 4.1 Matrix-element providers

The first programs for generating the matrix-element  $\mathcal{M}_{fi}$  needed in Eq. (4.1) were highly specialized. They would handle one specific process and would be mostly analytically hard-coded. At some point, authors from the theory community started to make their code available and the corresponding libraries would be assembled into multi-processes packages. This is the example of the NLOJet++ [78] and MCFM [79] packages. Nowadays, after a paradigm shift, the computation of the hard process matrix-element is decidedly automatized at one-loop level: programs like MADGRAPH [80], OPENLOOPS [81, 82] and GoSam [83, 84] can be interfaced directly to most MC generators and provide the amplitude given any phase-space point, while other programs focus on specific processes, as for example NJET [85], which calculates multijet amplitudes at NLO in massless QCD, VBFNLO [86–88] for vector-boson fusion in a number of processes, or HJETS++ [89] for Higgs boson production in association with one or more jets. We use GoSam-2.0 in all subsequent NLO computations, thus the mode of operation of the program is detailed in the next Section.

### 4.1.1 GoSam: MC interfacing of one-loop amplitudes

GoSam is a general-purpose package that computes one-loop amplitudes automatically and interfaces to any MC generator, provided it supports the Binoth-Les Houches Accord (BLHA1 [90] or BLHA2 [91]) format. The workflow of GoSam is shown in Fig. 4.2.

## 4 Monte-Carlo (MC) event generators

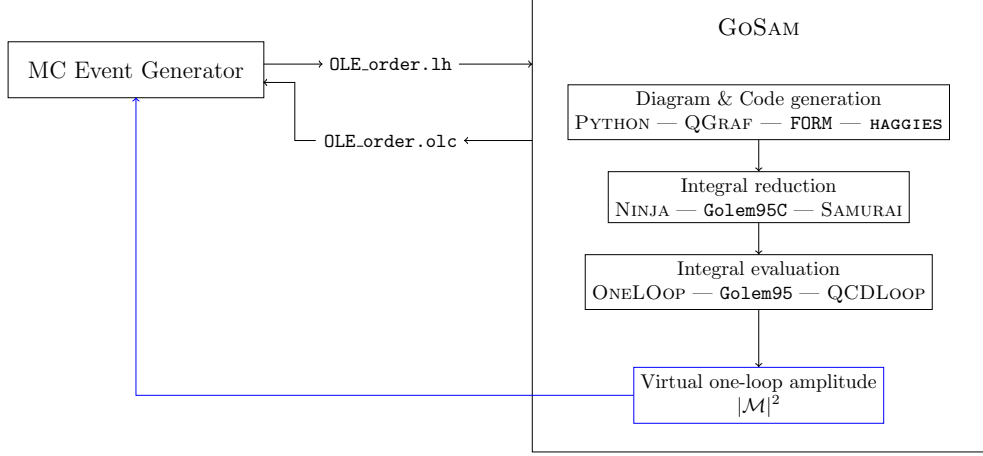


**Figure 4.2:** GoSAM relies on external packages to compute virtual one-loop amplitudes. Feynman diagrams are generated (and drawn) by QGRAF, and fortran code containing the terms relevant to each diagram is automatically written out in FORM. The various integral families are then reduced by either NINJA, Golem95C or SAMURAI libraries. Finally, the basis integrals are evaluated using either the ONELOOP, Golem95C or QCDLOOP packages.

Any process can be defined in the GoSAM input card, where only incoming and outgoing particles as well as the desired order in  $\alpha, \alpha_s$  for the generation of the Feynman diagrams have to be given. The PYTHON `gosam.py` executable is then called and a series of external packages handle the different steps of the computation: QGRAF [92] generates the Feynman diagrams, and filters for vertices or propagators can be applied, as well as manual removal of diagrams. Then, FORM [93] code containing the relevant expressions is generated automatically for all diagrams and helicities. Integral reduction is operated by any of three programs, namely NINJA [94], Golem95C [95, 96] or SAMURAI [97]. Finally, the evaluation of the set of basis integrals is checked out in one of the three external integral repositories QCDLOOP [98], ONELOOP [99] or Golem95C.

On a higher level, in compliance with BLHA, the MC generator produces a contract file `OLE_order.lh` containing the subprocesses to be computed by GoSAM. The latter is called and generates routines for all subprocesses. After checking the order file, GoSAM validates the contract and returns a control file `OLE_order.olc`. The generated libraries for all helicities are linked, and common functions are written in a `matrix.f90` file to be called by the MC generator. The physics parameters, like particles masses and couplings, can be set by an external call to the `OLP_Option` function. Then, for a set of 4-momenta  $(p_i)_{i=1,\dots,n}$ , the matrix-element is provided by calling the `OLP_EvalSubProcess({p_i})` function, which returns the full 1-loop amplitude coefficients  $c_{(-2)}$ ,  $c_{(-1)}$  and  $c_0$  (double, single pole and finite terms) as given in the Laurent series

$$|\mathcal{M}|^2 = \frac{\alpha_s}{2\pi} \frac{(4\pi)^\epsilon}{\Gamma(1-\epsilon)} \left( \frac{c_{(-2)}}{\epsilon^2} + \frac{c_{(-1)}}{\epsilon} + c_0 + \mathcal{O}(\epsilon) \right). \quad (4.3)$$

748     GO SAM is a very flexible package, and allows high-level control over the various sub-  
 749     tletties of higher-order computations (e.g. choice of regularization scheme, renormaliza-  
 750     tion counterterms, and so on). A rescue system for phase-space points that are numer-  
 751     ically badly behaved can be activated, and the amplitude for these is recomputed in  
 752     quadruple precision.

### 753 4.1.2 Infrared divergence cancellation

754     Having acquired the virtual contribution to the amplitude, one has to combine the Born,  
 755     virtual and real-emission contributions together. As was shown in Section 3.2, the sin-  
 756     gularities appearing in both virtual loop calculations and in soft/collinear configura-  
 757     tions of real emissions should combine to give finite quantities for any IR-safe observable.<sup>1</sup>  
 758     Although this is analytically true, in the case of MC computations, the different contri-  
 759     butions are first sampled over different phase-spaces, and only then combined. Symboli-  
 760     cally, we have, for the NLO cross-section  $\sigma^{\text{NLO}}$ :

$$\sigma^{\text{NLO}} = \int_{\Phi_m} d\sigma^B + \int_{\Phi_m} d\sigma^V + \int_{\Phi_{m+1}} d\sigma^R, \quad (4.4)$$

761     where  $d\sigma^B$ ,  $d\sigma^V$  and  $d\sigma^R$  are the Born, virtual and real contributions. Note that the  
 762     singularities in virtual and real contributions only cancel after integration. Numerically,  
 763     the cancellation of IR divergences is thus non-trivial. At NLO, there are two kinds of  
 764     algorithms to implement IR divergence cancellation: phase-space slicing and subtraction  
 765     methods. The Catani-Seymour (CS) automatized subtraction of IR divergences is mostly  
 766     used nowadays in NLO MC generators. The algorithm is outlined below and is used in  
 767     all calculations present from Chapter 6 on.

768     Consider the addition of a subtraction term  $d\sigma^S$  which approximates the ( $d = 4 - 2\epsilon$   
 769     regularized) real contribution and reproduces its IR singularity pattern in  $d$  dimensions:

$$d\sigma^V + d\sigma^R = d\sigma^V + d\sigma^S + (d\sigma^R - d\sigma^S). \quad (4.5)$$

770     Then, the ( $d = 4$ )-dimension limit can be taken directly for the integration of the real-  
 771     emission and the local counterterm cancels the divergence in the phase-space integrand.  
 772     The same is true for the virtual contribution, in general, only after integration. Returning  
 773     to the phase-space integrated result, the total NLO cross-section takes the form:

$$\sigma^{\text{NLO}} = \int_{\Phi_m} d\sigma^B + \int_{\Phi_m} \left( d\sigma^V + \int_{\Phi_1} d\sigma^S \right)_{\epsilon=0} + \int_{\Phi_{m+1}} (d\sigma^R|_{\epsilon=0} - d\sigma^S|_{\epsilon=0}), \quad (4.6)$$

774     where both of the last integrals are now separately finite. The CS dipole formal-  
 775     ism [100] is a factorization formula that allows the automatic generation of the subtrac-  
 776     tion term  $d\sigma^S$ . Universal dipole factors are introduced for any process, and setting the  
 777     subtraction term to

---

<sup>1</sup>Generally, at NLO, regularized poles appear either as double poles (soft and collinear), or single poles (soft, collinear, or UV).

## 4 Monte-Carlo (MC) event generators

$$d\sigma^S = \sum_{\text{dipoles}} d\sigma^B \otimes dV_{\text{dip}}, \quad (4.7)$$

$$\int_{\Phi_{m+1}} d\sigma^S = \sum_{\text{dipoles}} \int_{\Phi_m} d\sigma^B \otimes \int_{\Phi_1} dV_{\text{dip}} =: \int_{\Phi_m} d\sigma^B \otimes \mathbf{I} \quad (4.8)$$

778 allows one to compute the cross-section  $\sigma^{\text{NLO}}$  of any process:

$$\int_{\Phi_m} d\sigma^B + \int_{\Phi_m} (d\sigma^V + d\sigma^B \otimes \mathbf{I})|_{\epsilon=0} + \int_{\Phi_{m+1}} \left( d\sigma^R|_{\epsilon=0} - \sum_{\text{dipoles}} d\sigma^B \otimes dV_{\text{dip}}|_{\epsilon=0} \right) \quad (4.9)$$

779 with  $\mathbf{I}$  the integrated CS insertion operator. The universal dipole factors are obtained  
780 by considering the soft/collinear limits of a one-emission matrix-element with respect to  
781 the Born configuration:

$$|\mathcal{M}_{m+1}|^2 = \sum_{k \neq i,j} \mathcal{D}_{ij,k}(p_1, \dots, p_{m+1}) + (\text{regular in } p_i \cdot p_j \rightarrow 0) \quad (4.10)$$

$$= - \sum_{k \neq i,j} \frac{1}{2p_i \cdot p_j} \mathcal{M}_m^\dagger(i, j \rightarrow \tilde{i}\tilde{j}, \tilde{k}) \left( \frac{\mathbf{T}_k \cdot \mathbf{T}_{ij}}{\mathbf{T}_{ij}^2} \mathbf{V}_{ij,k} \right) \mathcal{M}_m(i, j \rightarrow \tilde{i}\tilde{j}, \tilde{k}) \\ + (\text{regular in } p_i \cdot p_j \rightarrow 0) \quad (4.11)$$

782 where the singular terms are collected in the dipoles  $D_{ij,k}$ . The  $\mathbf{T}_i$  are the generators of  
783 the colour algebra and  $\mathcal{M}_m$  is a general matrix-element corresponding to an  $m$ -particle  
784 final-state,  $\mathcal{M}_m = |1, \dots, m\rangle$ . Then Eq. (4.11) states that the matrix-element corre-  
785 sponding to an  $(m+1)$ -particle final-state factorizes into dipole factors  $\mathbf{V}_{ij,k}$  convo-  
786 luted with an underlying Born configuration where partons  $i$  and  $j$  are assembled into  
787 one parton  $(\tilde{i}\tilde{j})$  (the so-called *emitter*), and parton  $\tilde{k}$  (the *spectator*) absorbs the residual  
788 4-momentum. The formulae for the universal dipoles  $\mathbf{V}_{ij,k}$  are very closely related to  
789 the Altarelli-Parisi splitting functions, see Section 4.2.

790 In the case of the presence of initial-state hadrons like at the LHC, Eq. (4.11) is  
791 modified and an additional dipole term has to be added in Eq. (4.8),  $dV_{\text{dip}} \rightarrow dV_{\text{dip}} +$   
792  $dV'_{\text{dip}}$ . Eq. (4.8) then becomes

$$\int_{\Phi_{m+1}} d\sigma^S = \int_{\Phi_m} d\sigma^B \otimes \mathbf{I} + \int_0^1 dx \int_{\Phi_m} d\sigma_B(xp) \otimes (\mathbf{P} + \mathbf{K})(x), \quad (4.12)$$

793 where  $xp$  is the proton momentum fraction carried away by the parton, and  $\mathbf{P}, \mathbf{K}$  are  
794 insertion operators appearing from the convolution with the PDF.

## 4.2 Parton-shower models

### 4.2.1 Altarelli-Parisi splitting functions

Parts of the following Section are adapted from Ref. [101]. Inherently, the few-parton, high-energy final-state generated by the hard process matrix-element further produces both QCD and QED radiation. The parton-shower algorithm evolves partons from the collision scale  $Q^2$ , letting them radiate new partons (quarks and gluons), to a cutoff scale  $Q_{\min}^2$  that is set around the hadronization scale. At that point, the shower terminates and the final-state is passed on to the hadronization model. Schematically, the simplest shower algorithms are based on the so-called Dokshitzer–Gribov–Lipatov–Altarelli–Parisi (DGLAP) kernels [102–104] for  $1 \rightarrow 2$  collinear particle splitting  $P_{a \rightarrow bc}$ , as given in Fig. 4.3.

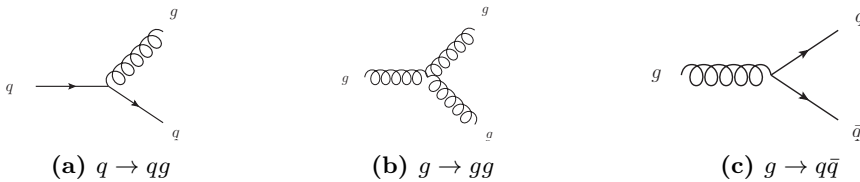


**Figure 4.3:** The QCD vertices for  $1 \rightarrow 2$  splittings allow to calculate the leading-order kernels appearing in the DGLAP evolution equation.

The (unregularized) LO kernels can be computed from the QCD interaction vertices as:

$$P_{q \rightarrow qg}(z) = C_F \frac{1+z^2}{1-z}, \quad (4.13)$$

$$P_{g \rightarrow gg}(z) = 2C_A \left( \frac{1-z}{z} + z(1-z) + \frac{z}{1-z} \right), \quad (4.14)$$

$$P_{g \rightarrow q\bar{q}}(z) = T_R(1 - 2z(1-z)). \quad (4.15)$$

with  $z$ ,  $0 \leq z \leq 1$ , the longitudinal momentum fraction of the parent parton  $a$ . Notice the undefined behavior of  $P_{q \rightarrow qg}$  and  $P_{g \rightarrow gg}$  for  $z \rightarrow 1$ : the splitting functions can be regularized from general constraints to:

$$P_{q \rightarrow qg}(z) = C_F \left( \frac{1+z^2}{(1-z)_+} + \frac{3}{2} \delta(z-1) \right), \quad (4.16)$$

$$P_{g \rightarrow gg}(z) = 2C_A \left( \frac{1-z}{z} + z(1-z) + \frac{z}{(1-z)_+} + \left( \frac{11}{12} - \frac{1}{3} \frac{T_R}{C_A} \right) \delta(z-1) \right), \quad (4.17)$$

$$P_{g \rightarrow q\bar{q}}(z) = T_R(1 - 2z(1-z)). \quad (4.18)$$

The factor  $(1-z)^{-1}$  is regularized in being interpreted as a plus-distribution  $(1-z)_+^{-1}$  such that for any test function  $f(z)$  sufficiently regular at  $z=0, z=1$ ,

## 4 Monte-Carlo (MC) event generators

$$\int_0^1 \frac{dz f(z)}{(1-z)_+} = \int_0^1 \frac{f(z) - f(1)}{1-z} . \quad (4.19)$$

813     The master equation governing the evolution of the collinear splitting of a parton  $a$   
 814     from a scale  $q^2$  to a scale  $q^2 + dq^2$  is then given by

$$dP_{a \rightarrow bc} = \frac{dq^2}{q^2} \frac{\alpha_s}{2\pi} P_{a \rightarrow bc}(z) dz , \quad (4.20)$$

815     where  $q^2$  is an arbitrary strong-ordered evolution variable. It can be the azimuthal  
 816     angle of emission  $E_a^2 \theta^2$ , or the particle's virtuality  $m^2$ , or the transverse momentum  
 817      $p_T^2$ . Different shower algorithms implement different choices of the evolution variable.  
 818     This will be of importance when considering parton-shower related uncertainties, see  
 819     Chapters 7 and 11.

### 820     4.2.2 The Sudakov form factor

821     Going from the one-emission to the multiple-emission case, and using broad assump-  
 822     tions<sup>2</sup>, the probability of no-emission between scales  $Q^2$  and  $Q_{\max}^2$  is given by the *Sudakov*  
 823     *form factor*:

$$dP_{a \rightarrow bc}(z) = \frac{dq^2}{q^2} \frac{\alpha_s}{2\pi} P_{a \rightarrow bc}(z) dz \times \exp \left( - \sum_b \int_{Q^2}^{Q_{\max}^2} \frac{dq'^2}{q'^2} \int \frac{\alpha_s}{2\pi} P_{a \rightarrow bc}(z') dz' \right) . \quad (4.21)$$

824     As explained in Sec. 3.1.3, the perturbative expansion of the cross-section in  $\alpha_s$  can  
 825     suffer from large enhancements in the soft/collinear regions of phase-space. In general,  
 826     double logarithms of the form  $\alpha_s^n \log^{2n}(Q^2/q^2)$  appear when a soft particle is emitted, or  
 827     when it becomes collinear to one of the incoming partons. Here,  $q^2$  is the scale describing  
 828     the soft/collinear emission, and  $Q^2$  is the global scale of the process. Generally, this tower  
 829     of large logarithms can be analytically resummed to all orders in  $\alpha_s$ . Instead, the parton  
 830     shower algorithm offers the possibility of resumming soft and collinear contributions  
 831     within the Monte-Carlo framework. Nowadays, most parton showers only guarantee  
 832     leading-logarithmic (LL) accuracy, although recent studies [105] have found differences  
 833     at LL (subleading number of colors  $N_C$ ), and NLL (leading- $N_C$ ) between parton-showers  
 834     and analytic resummations.

### 835     4.2.3 Parton-shower matching

836     The shower algorithm should respect the theoretical accuracy of the hard matrix-element,  
 837     and at the same time conserve the logarithmic accuracy of the parton-shower resumma-  
 838     tion in their respective limits. In particular, the cross-section after showering should

---

<sup>2</sup>Namely that the time between emissions can be sliced, and unitarity as well as multiplicativity (meaning the shower has no memory of past emissions) hold.

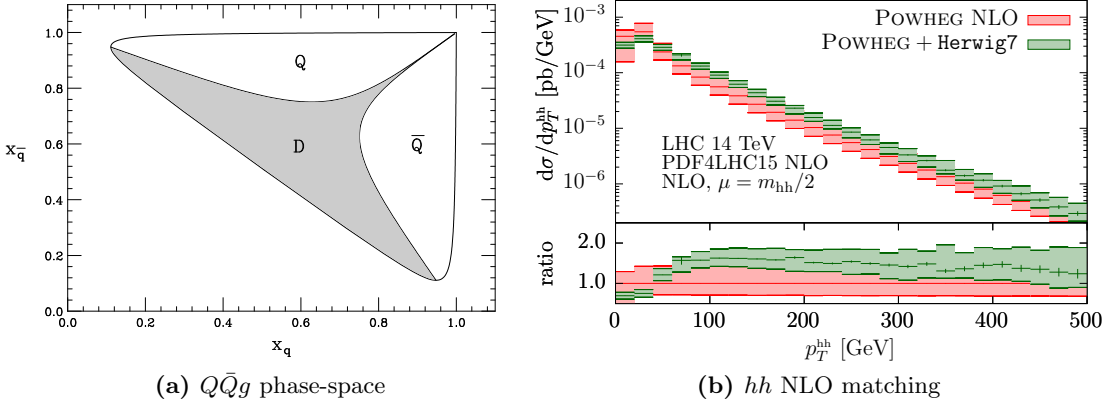


**Figure 4.4:** (a) Phase-space for a heavy-quark pair emitting a gluon, depicted as a function of the Dalitz plot variables ( $x_Q, x_{\bar{Q}}$ ). Figure adapted from Ref. [110]. (b) The transverse momentum  $p_T^{hh}$  of the Higgs pair system in di-Higgs production is compared for the fixed-order NLO prediction to a parton-shower matched calculation.

be identical to the fixed-order cross-section. Also, kinematic configurations that belong both to the hard matrix-element and the parton-shower final-states should not be double-counted. This whole procedure is called *matching*.

At NLO, the matching of the parton-shower algorithm to the fixed-order matrix-element handles both these issues. Roughly said, it interpolates between the two kinematic regions where the hard matrix-element, respectively the parton-shower, generate their respective dominant contributions. As an example, the phase-space for the production of two heavy quarks and one gluon-emission  $Q\bar{Q}g$  is given in Fig. 4.4a. The soft/collinear emission regions (where  $x_Q \rightarrow 1$  or  $x_{\bar{Q}} \rightarrow 1$ , with  $x_j = 2p \cdot q_j/p^2$ , and  $p$  is the initial center-of-mass 4-momentum) can be covered by the parton-shower while the dead region (shaded) describes a hard gluon-emission (matrix-element). In a correct matching, these regions should not overlap. An illustration of this fact is shown in Fig. 4.4b for the case of  $gg \rightarrow hh$  production, where a fixed-order NLO calculation is matched to the `Herwig7` [106, 107] parton-shower. There, the parton-shower correctly reproduces the NLO computation at high-transverse momentum and softens the low-momentum region (Sudakov suppression). Among the various matching procedures that keep in line with the above criteria, the subtractive `MC@NLO` [108] and the multiplicative Powheg [109] schemes are among the most used ones.

As examples of available parton-shower algorithms mostly used by the physics community, the `Pythia 8` [111, 112] and `Herwig7` codes implement a  $p_T$ -ordering, respectively an angular-ordering in the choice of the evolution variable. `Herwig` also uses a dipole shower as an alternative algorithm (which is based on a Catani-Seymour dipole formulation of  $2 \rightarrow 3$  splitting kernels). The `Sherpa` [113] generator implements two alternative parton-shower algorithms based on variations of the CS dipoles.

### 863 4.3 Hadronization

864 Once particles have been showered down to the hadronization scale, the hadronization  
 865 model takes over. By far, the two most used hadronization models are the Lund string  
 866 model and the cluster model.

#### 867 4.3.1 Lund string model

868 The Lund string model [114] is based on the principle of quark color confinement. When  
 869 two quarks are separated by a distance  $r$ , the potential takes the form:

$$U(r) = -\frac{4}{3} \frac{\alpha_s}{r} + \kappa r, \quad (4.22)$$

870 and the linear confinement contribution dominates for larger distances, with  $\kappa \sim$   
 871 1 GeV/fm. In analogy to a classical elastic potential, the field lines build up a stretched  
 872 *string*. When the distance between a quark-pair increases, the string tension grows  
 873 until the string breaks: the freed energy creates another quark-antiquark pair appearing  
 874 from the vacuum. The creation of the quark-pair happens with a Gaussian probability  
 875 (similarly to quantum tunnelling) in the quark transverse mass  $m_T^2 = m^2 + p_T^2$ . From  
 876 Lorentz invariance, causality and left-right symmetry, the fragmentation function  $f(z)$   
 877 can be constrained and fixes the longitudinal momentum fraction  $z$  carried away by the  
 878 created hadron:

$$\mathcal{P} \propto \exp\left(-\frac{\sigma m_T^2}{\kappa}\right), \quad f(z) \propto \frac{(1-z)^a}{z} \exp\left(-\frac{bm_T^2}{z}\right). \quad (4.23)$$

879 The Lund string model is implemented in the **Pythia 8** generator and the main pa-  
 880 rameters  $a, b, \sigma$  are determined by tuning to data. For the more complex case of baryons,  
 881 the three quarks can be pictured in a quark-diquark frame. Finally, the gluons appear  
 882 as kinks on strings. For more details and improvements to the model, see the **Pythia**  
 883 manual [115].

#### 884 4.3.2 Cluster model

885 Instead of building on color confinement, the cluster model [116, 117] makes the as-  
 886 sumption that gluons can be viewed as carrying color and anticolor and behaving as a  
 887  $q\bar{q}$  pair. Color singlets usually obey a mass spectrum that peaks at low mass due to  
 888 the property of preconfinement of the parton shower [118], i.e. they are closer to one  
 889 another in phase-space. The model then clusters these color singlets together and splits  
 890 them per the following procedure: if a cluster of mass  $M$ , with parton constituents of  
 891 masses  $m_1, m_2$ , satisfies

$$M^{C_{\text{pow}}} > C_{\text{max}}^{C_{\text{pow}}} + (m_1 + m_2)^{C_{\text{pow}}}, \quad (4.24)$$

892 the algorithm splits it and the masses get redistributed. To split a cluster, the model  
 893 pops a  $q\bar{q}$  pair from the vacuum and forms two new clusters with one original parton  
 894 each, and masses distributed according to

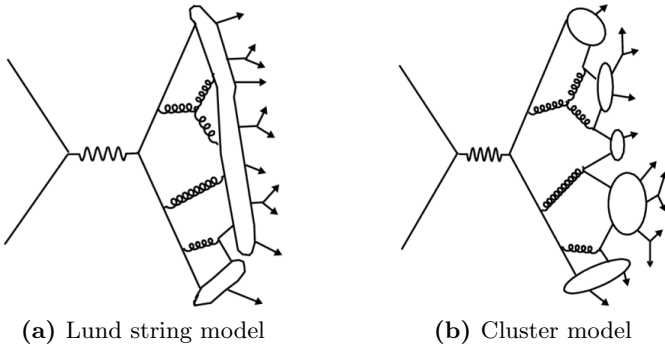


**Figure 4.5:** A pictorial representation of both hadronization models. (a) In the Lund model, the potential energy from the color field between two quarks increases linearly with the distance, like in a string. When a string breaks, a new quark-antiquark pair is created. (b) The cluster model groups color-connected partons together into clusters and lets them decay isotropically.

$$M_{1,2} = m_{1,2} + (M - m_{1,2} - m_q) \mathcal{R}_{1,2}^{P_{\text{split}}}, \quad (4.25)$$

with  $\mathcal{R}_{1,2} \in [0, 1]$  two random numbers. Again, the parameters  $C_{\text{pow}}$ ,  $C_{\text{max}}$  and  $P_{\text{split}}$  have to be tuned to data.

Notice that the cluster model does not propagate any spin information: the hadronized clusters therefore decay isotropically. Historically, the cluster model was implemented in the **Herwig** event generator. Fig. 4.5 summarizes the conceptual differences between the Lund string and the cluster model.

As a concluding remark, the MC event generators represent the basis of a large fraction of experimental measurements. They are quite complex systems whose constituents are all inter-correlated: the different pieces interact and the matching between all appearing physical scales is not always explicit at the end of the simulation. Typically, the parton-shower output influences the hadronization tune, and it is in general difficult to disentangle their respective contributions. As such, variations in the MC setup are linked to large uncertainties which should, in principle, be taken into account with their full correlations.



## 909 5 The LHC and the ATLAS detector

910 The Large Hadron Collider, or LHC, is currently the most powerful particle accelerator  
911 worldwide and is located at the Centre Européen pour la Recherche Nucléaire (CERN)  
912 on the French-Swiss border, near Geneva. Historically, it replaced the Large Electron-  
913 Positron (LEP) collider after it was decommissioned in 2000, and is being housed in  
914 the same tunnel. In this Chapter, we shall briefly review the main working parts of  
915 the accelerator complex, and then dive in more detail into the structure of the ATLAS  
916 detector. A short overview of the trigger and data acquisition system, as well as the  
917 object reconstruction and MC simulation, will close the subject.

### 918 5.1 The Large Hadron Collider

919 The LHC's main collider ring [119–121] is installed in a circular tunnel of  $\sim 27$  km  
920 circumference and a depth varying between 45 m and 170 m under ground level. It is  
921 designed to accelerate protons to a design center-of-mass energy of 14 TeV at a peak  
922 luminosity of  $10^{34} \text{ cm}^{-2} \text{ s}^{-1}$ . As a side note, the LHC also collides heavy ions, and in  
923 the past a few runs of lead-lead, proton-lead and xenon-xenon collisions have also given  
924 interesting complementary physics results.

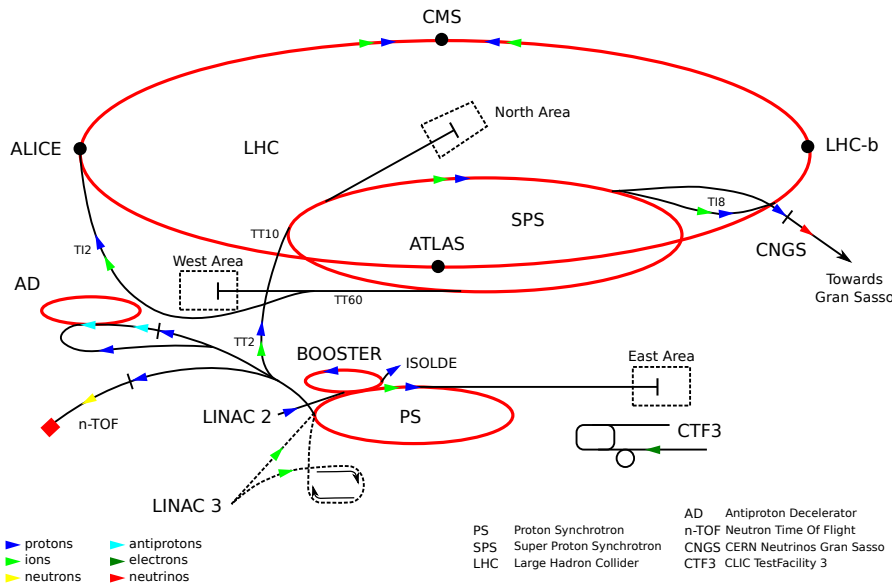


Figure 5.1: The LHC accelerator complex [122].

## 5 The LHC and the ATLAS detector

To accelerate protons to the design center-of-mass energy, a sequence of pre-accelerators boosts the proton beams before injecting them into the next link. A schematic of the full accelerator complex is presented in Fig. 5.1. Upon being produced and pre-collimated, the protons are accelerated to 50 MeV in the Linac2, then to 1.4 GeV in the Proton Synchrotron (PS) Booster, and to 26 GeV in the PS. Within the PS, the protons are collimated into 25 ns-spaced (7.5 m) bunches of around  $1.15 \cdot 10^{11}$  protons per bunch. From there, the Super Proton Synchrotron ramps up the energy to 450 GeV, and injects both beams in opposite directions into the LHC itself. After approximately 20 minutes of acceleration in the main LHC beampipe by 16 radiofrequency (RF) cavities, the proton bunches achieve the current energy of 6.5 TeV per beam.

Equipped with 1232 superconducting main dipole magnets, the LHC operates with magnetic fields of  $\sim 8.3$  T to keep the proton bunches on their circular trajectory. The main dipoles are supplemented by higher-multipole magnets to correct for edge imperfections in the dipole field. Along the LHC lattice, 392 main quadrupole magnets are used to re-focus the proton beams.

Once at the nominal energy, the two circulating proton beams are made to collide at four different interaction points, corresponding to the four biggest LHC experiments: ATLAS, CMS, ALICE and LHCb. Out of these, ATLAS and CMS are general-purpose detectors designed to discover higher-mass particles like the Higgs boson or possible supersymmetric resonances, as well as to produce high-precision measurements of particles like the top-quark, whose properties were poorly resolved in earlier experiments. ALICE and LHCb, on the other hand, are dedicated to studies of heavy-ion collisions and focus on high-density QCD bound states and flavor physics. From the start of Run II in 2015 until the Long Shutdown of December 2018, the LHC delivered a total integrated luminosity of  $147 \text{ fb}^{-1}$  at a center-of-mass energy of 13 TeV and a peak luminosity of  $2.1 \cdot 10^{34} \text{ cm}^{-2} \text{ s}^{-1}$ , even surpassing the design value. In the next Section, we will concentrate on the ATLAS detector substructure.

## 5.2 The ATLAS detector

A Toroidal LHC ApparatuS (ATLAS) [123] aims for high-energy precision measurements of the SM in all possible sectors: with the help of the enormous amount of data produced at LHC and the precision of the tracking detectors and calorimeters, it allows for measurements of particle masses and SM couplings (from the CKM matrix to the Higgs boson coupling to other particles,  $\alpha_s$  measurements and PDF fits) or cross-section measurements, but also the observation of rare SM processes (like  $t\bar{t}h$  production [124], light-by-light scattering [125] or  $B_s^0 \rightarrow \mu^+ \mu^-$  decays [126]). These high-precision tests of the SM are intrinsically linked to searches for Beyond the SM (BSM) physics: higher-scale BSM particles participating in loop corrections to the SM can have an impact on the cross-sections or kinematic observables, and any observed deviation from the SM predictions would hint at New Physics not far from the TeV scale. In general, though, direct searches are employed to discover potential high-mass resonances.

The ATLAS detector, situated at the LHC beam interaction point 1 near Meyrin, Switzerland, is an onion-shell structure comprised of particle trackers, an electromagnetic and hadronic calorimeter, and a muon detector: from inner to outer radii, the produced particles encounter the Inner Detector (ID), the Liquid Argon (LAr) and the Tile Calorimeter (TileCal), and finally the Muon Spectrometer. The detector itself is 44 m long and has a diameter of 25 m, and weighs more than 7000 tons. Fig. 5.2 shows a rendering of the ATLAS detector. To bend the charged-particle tracks for momentum measurement, ATLAS relies on four magnets: a 2 T central solenoid close to the interaction point, an 8-coil barrel toroid that is cylindrically placed around the detector generating a magnetic field of 4 T, and two other 8-coil toroid magnets at the detector endcaps which provide a 4 T magnetic field. The geometry of the magnet coils is shown in Fig. 5.3.

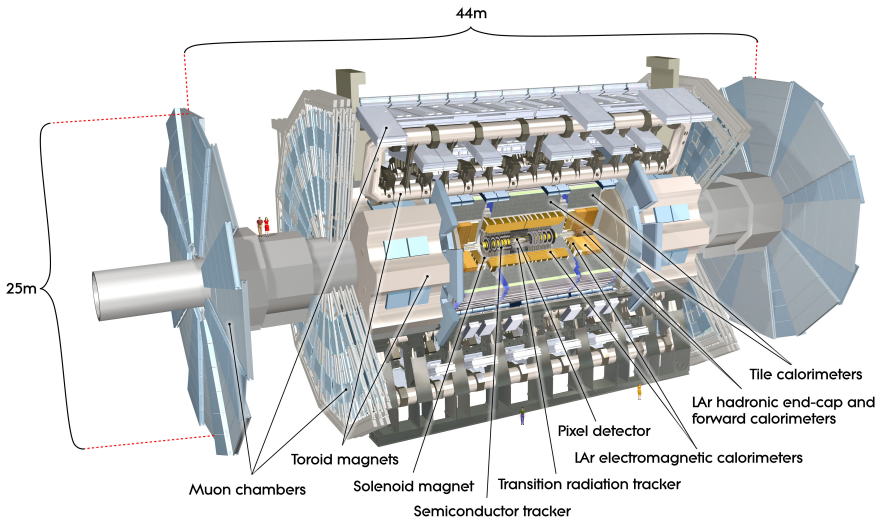


**Figure 5.2:** A cut-away view of the ATLAS detector. Figure from Ref. [123].

The ATLAS coordinate system is defined as right-handed and centered at the interaction point, with the beam axis chosen as the  $z$ -axis, and the  $x$ -axis pointing towards the center of the LHC ring.

### 5.2.1 The Inner Detector

Being the piece of equipment closest to the beampipe, the Inner Detector (ID) [127, 128] must fulfill several criteria for the reconstruction of charged-particles four-momenta, as well as for the identification of secondary vertices due to the decay of bottom-flavored particles and the measurement of the impact parameter. The ID is further divided into a Silicon Pixel Detector (SPD) [129], a Semiconductor Tracker (SCT) [130] and a Transition Radiation Tracker (TRT) [131, 132]. In Fig. 5.4, the structure of the ID is presented in a cut view along the beampipe (with the notable absence of the new insertable  $B$ -layer, or IBL).

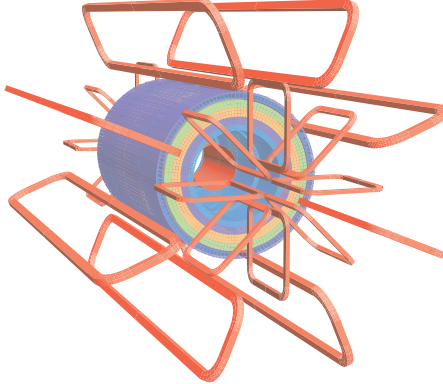


**Figure 5.3:** The geometry of the coils used to produce the magnetic field in the ATLAS detector. A solenoid magnet (2 T) is installed cylindrically around the beampipe, surrounded by a toroid magnet (4 T) and two endcap toroid magnets (4 T). Figure from Ref. [123].

The SPD has a total of  $86 \cdot 10^6$  channels and is the element closest to the interaction point. Four concentric layers of silicon pixel detectors are laid out around the beam axis in so-called barrel layers. The innermost layer is called the insertable  $B$ -layer (IBL) and was installed during the first Long Shutdown. It is only 3.3 cm away from the interaction point and allows for precise measurements of secondary vertex positions. It was designed to work in a high-radiation environment. Three other layers (including the old  $B$ -layer) are disposed concentrically around the beampipe, while three pixel disks are mounted on each endcap. The barrel layer and endcap disks have a resolution of  $12 \mu\text{m} \times 87 \mu\text{m}$ , respectively  $13 \mu\text{m} \times 78 \mu\text{m}$  in the transverse-, respectively longitudinal- ( $T, L$ ) directions.

At intermediate radius, the SCT is a silicon microstrip tracker and provides, out of  $6.2 \cdot 10^6$  readout channels, a measurement of the  $(\phi, r, z)$  track points. Four SCT barrel layers are disposed at radii between 299 mm and 514 mm away from the beampipe, while 18 more planar discs are placed at the endcaps. The barrel modules have a resolution of  $15 \mu\text{m} \times 530 \mu\text{m}$ .

Finally, at the outer layer, the TRTs are made of thin-walled straw tubes and give information for distinguishing between electrons and pions, as well as contribute to the transverse position measurement for a total of  $350 \cdot 10^3$  readout channels. A straw tube is a 4 mm-diameter cylinder filled with gaseous xenon and a gold-plated tungsten wire strung through the center. With the inner tube wall (cathode) and the wire (anode) held at 1.5kV of voltage difference, a charged particle passing through ionizes the gas, and the freed electrons drift to the wire: the drift time can then be used to determine the distance from the anode. Moreover, electron identification succeeds by transition-radiation photons created between the straws and converted in the xenon gas. The probability of transition radiation is proportional to the relativistic factor  $\gamma$ , which is usually higher for electrons and positrons. The TRTs determine the transverse position at a resolution of  $\sim 100 \mu\text{m}$ .

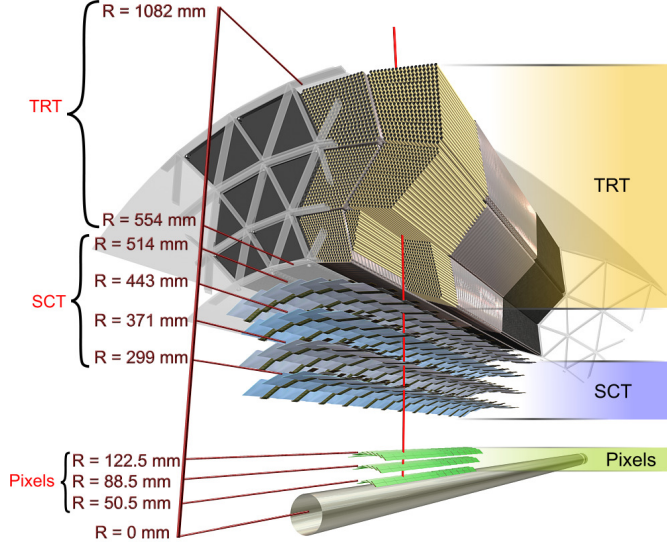


**Figure 5.4:** Cross-sectional view of the Inner Detector (ID). The ID particle tracker is made up of the Silicon Pixel Detector, the microstrip Semiconductor Tracker (SCT), and the Transition Radiation Tracker (TRT). Figure from Ref. [123].

### 1016 5.2.2 The Liquid Argon (LAr) Calorimeter

1017 Both the electromagnetic (EM) and the hadronic calorimeters are found between the ID  
 1018 and the muon spectrometer. Fig. 5.5 depicts the LAr calorimeter [133] in yellow, which is  
 1019 closest to the ID and enveloped by the Tile Calorimeter (see Section 5.2.3). The calorime-  
 1020 ters mainly measure the energy deposited by the particles, but they also contribute to  
 1021 position measurements and particle identification as well as to the measurement of the  
 1022 missing transverse energy. The LAr calorimeter contains both EM and hadronic de-  
 1023 tectors. In principle, a passing electron or photon produces an electromagnetic shower  
 1024 in the EM calorimeter mainly through bremsstrahlung and electron-positron pair cre-  
 1025 ation. In comparison, hadrons generate further hadronic activity by primary nuclear  
 1026 reactions and spallation, and also produce EM showers. The LAr calorimeter functions  
 1027 as a system of alternating lead/stainless steel absorbers and electrodes measuring the  
 1028 signal drift-time, with the whole system immersed in liquid argon which plays the role  
 1029 of active medium.

1030 The electromagnetic barrel (EMB,  $|\eta| < 1.475$ ) and endcap (EMEC,  $1.375 < |\eta| < 3.2$ )  
 1031 calorimeters use the same absorber material and geometry. In the forward region (FCal)  
 1032 at rapidities  $3.1 < |\eta| < 4.9$ , a copper-based absorber covers EM activity while a tungsten  
 1033 module provides measurement of hadronic energy deposition. Finally, a hadronic LAr  
 1034 calorimeter is also placed at the endcaps (HEC) and complements readings from the Tile  
 1035 Calorimeter.

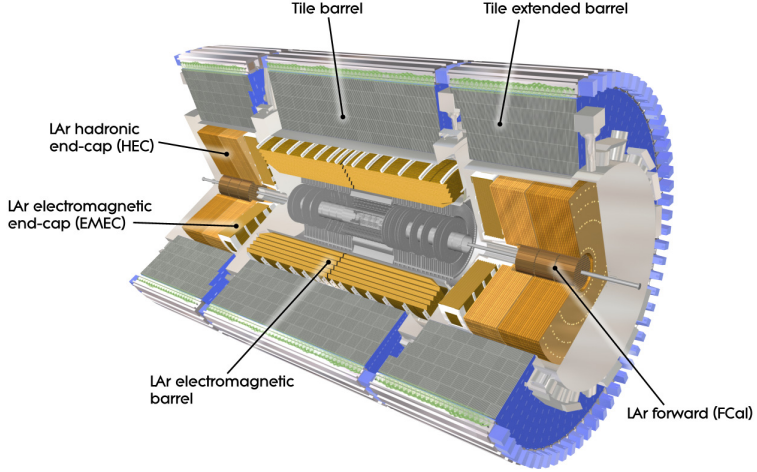


**Figure 5.5:** The ATLAS calorimetry system is composed of the inner Liquid Argon calorimeter (yellow) and the outer Tile Calorimeter (gray). Figure from Ref. [123].

### 1036 5.2.3 The Tile Calorimeter (TileCal)

1037 The central and two extended barrel regions are covered by the TileCal [134], which  
 1038 is cylindrically disposed around the beampipe (see Fig. 5.5) and is made of iron plate  
 1039 absorbers and plastic scintillators as the active medium. The scintillating light created  
 1040 by hadronic energy deposition is wavelength-shifted and led to photomultiplier tubes  
 1041 that amplify the signal.

### 1042 5.2.4 The Muon Spectrometer

1043 At the outmost layer of the ATLAS detector, the Muon Spectrometer (MS) [135] is  
 1044 designed to deliver high-precision measurements of the muons' transverse momentum.  
 1045 It uses four different techniques to trigger and detect the produced muons: resistive-  
 1046 plate chambers (RPC) [136], cathode strip chambers (CSC) [137], monitored drift tubes  
 1047 (MDT) [138] and thin-gap chambers (TGC) [139], shown in Fig. 5.6. The muons are bent  
 1048 by three air-core toroid magnets for a rapidity-dependent bending power between 1 – 7.5  
 1049 Tm. This amounts to a resolution of  $\sim 10\%$  in the transverse momentum of high-energy  
 1050 muons at around 1 TeV. Both the RPCs and the TGCs are used as a first-level trigger  
 1051 on well-resolved, high- $p_T$  muons in the barrel region, respectively the endcaps. On the  
 1052 other hand, the MDTs which are laid out in the barrel and endcap regions, and the  
 1053 CSCs in the forward region, measure the position of the incoming muons in the bending  
 1054 plane.

### 1055 5.2.5 Trigger and Data acquisition

1056 The collision rate at high-energy collider experiments like ATLAS poses enormous com-  
 1057 puting and storage problems. At LHC, the proton bunch crossing rate at the current

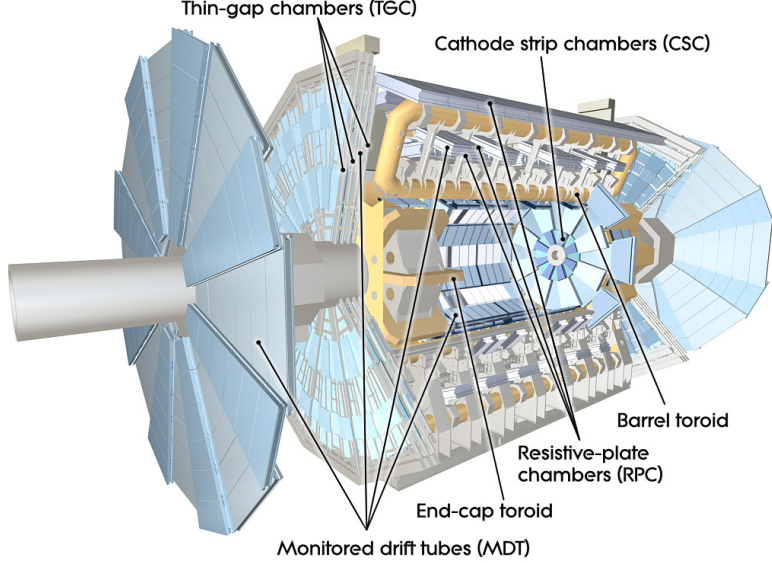


**Figure 5.6:** The ATLAS muon spectrometer. Figure from Ref. [123].

luminosity towers at a vertiginous 40 MHz. With a data content of  $\sim 1.6$  MB per event, the storage of all events would produce  $\sim 60$  TB per second. Thus the event rate needs to be reduced to an affordable storage and readout rate. The ATLAS trigger and data acquisition system [140, 141] lowers the stored event rate using certain quality criteria from the detectors. The trigger system is organized in three sublevels:

- **Level 1:** The first layer triggers at the hardware level already, and uses both calorimetry information (cluster energy sum / isolation criteria) and data from the muon trigger chambers to reduce the event rate from 40 MHz to  $\sim 75$  kHz.
- **Level 2:** At the software level, the Level 2 Trigger uses regions-of-interest identified by Level 1 and combines information from all subdetectors to focus on the physics objects. The event rate is then reduced from 75 kHz to  $\sim 1$  kHz.
- **Event Filter:** The full event data is analyzed online and the Level 2 selection is refined by the Event Filter (EF), which can also perform full event reconstruction at this stage. Accepted events are then stored permanently on disk at a rate of  $\sim 200$  Hz for an acceptable total storage rate of around 300 MB per second.

Since Run II, the ATLAS software trigger comprises a single high-level trigger (HLT) farm, instead of the separate Level 2 and EF trigger levels, reducing the Level 1 total event rate from 100 kHz to 1 – 1.5 kHz. The raw data is then stored first in the central CERN data center. These sites make up the so-called Tier-0 system. The whole LHC Computing Grid is composed of several levels (tiers). After the central CERN data center at Tier-0, the data is redistributed to 13 other computer storage and analysis sites forming the Tier-1, which store and process the raw data into refined formats

## 5 The LHC and the ATLAS detector

1080 and distributes it along to Tier-2 computer sites (university/institute clusters). Tier-  
1081 3 sites are composed of local computers for analysis purposes. Mostly, analysts use  
1082 pre-processed data that simplifies the description of physics objects.

### 1083 5.2.5.1 Data formats and Event reconstruction

1084 From the raw data saved on-site to the final format available to analysts, several levels of  
1085 data processing and reconstruction are implemented to derive a meaningful identification  
1086 of physics objects that can be used as such in an analysis. Below are presented the  
1087 successive file formats and their content:

- 1088 • **RAW**: The raw data from the trigger output are stored as primary information  
1089 from the subdetectors: these complete events contain useless or redundant infor-  
1090 mation and metadata for the final analyses.
- 1091 • **ESD**: The detector output present in the RAW events is fed to the reconstruction  
1092 algorithm, and all the information needed for particle identification, track fitting,  
1093 jet calibration is summarized in so-called Event Summary Data (ESD) files.
- 1094 • **xAOD**: More information is pruned away, and only the physics objects (electrons,  
1095 muons, jets, MET, ...) are summarized in containers and saved as ROOT files  
1096 called Analysis Object Data (xAOD).
- 1097 • **DxAOD**: The xAOD files are further reduced to analysis-dependent (Top, Higgs,  
1098 SUSY ...) event subsets, the derived AODs (DxAOD). The goal is to reduce  
1099 file size and analysis computing times. Derived AODs are produced by either  
1100 removing uninteresting events (so-called *skimming*), eliminating entire variables  
1101 or object collections from all events (*slimming*), or removing particular objects in  
1102 some events (*thinning*). Analyses handle directly the derived xAOD files as input.

1103 Without entering into much detail, reconstruction algorithms for electrons and pho-  
1104 tons [142], muons [143], jets and MET [144, 145] mostly use information from calorimeter  
1105 energy clusters matched to one or several tracks identified in the Inner Detector. The  
1106 various common physics objects are reconstructed via trigger selection, identifica-  
1107 tion and isolation criteria, and classified with the help of different quality definitions: **Loose**,  
1108 **Medium**, **Tight** (and other for e.g. muons). Identification (ID) efficiency factors can  
1109 be determined from comparisons of MC simulations against data standard candles: for  
1110 example, lepton ID efficiencies are calibrated with the help of  $J/\psi \rightarrow \ell\ell$  and  $Z \rightarrow \ell\ell$   
1111 events. The latter also serve for calibrating energy/momentum scale and resolution fac-  
1112 tors (which correct, respectively quantify the systematic uncertainty on the measured  
1113 4-momenta). In the case of jets, their reconstructed energy also has to be calibrated.  
1114 The determination of energy scale factors and uncertainties is more complicated and  
1115 comprises several steps, in particular MC-based followed by *in situ* energy calibration.<sup>1</sup>

---

<sup>1</sup>This type of energy calibration uses events where a well-known reference object recoils against one measured jet, e.g.  $Z(\rightarrow \ell\ell) + j, \gamma + j$ .

1116 **5.2.5.2 MC simulation**

1117 Common MC event generation was explained in Chapter 4. In the following, we define a  
 1118 *parton-level* event as the set of particles (with their well-defined 4-momenta) produced  
 1119 by the hard-scattering matrix-element or by the parton-shower algorithm applied to  
 1120 the hard collision, but before hadronization. We will differentiate between both cases  
 1121 explicitly when necessary. Such parton-level events are unphysical since they do not  
 1122 obey color confinement. The output of a full-fledged MC program after hadronization  
 1123 is a collection of events at *particle-level*: this is usually the point of comparison between  
 1124 theory and experiment. Finally, accounting for the further evolution of particles in the  
 1125 magnetic field of a specific experiment, as well as geometric acceptance and detection  
 1126 efficiencies, defines measurable events at *detector-level*. The full process of producing sets  
 1127 of events at detector-level from the theory input will be referred to as MC simulation.

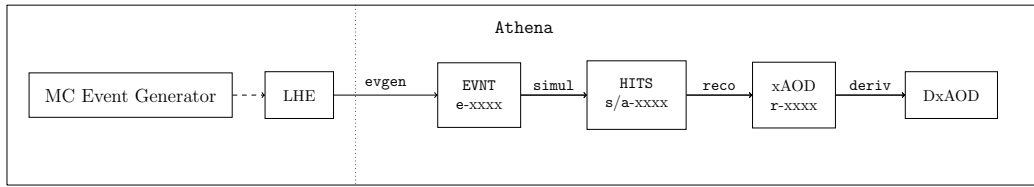


**Figure 5.7:** The Athena workflow for MC event generation and simulation.

1128 In the ATLAS experiment, this production chain is implemented in the **Athena** frame-  
 1129 work, and comprises several steps outlined in Fig. 5.7. The event output at each stage  
 1130 is identified by a tag. For a given process, the first step consists of basic MC produc-  
 1131 tion using the programs available on the market (SHERPA, Herwig7, Pythia8, and so  
 1132 on). The **AthGeneration** subpackage handles the interfacing of public MC programs in  
 1133 the ATLAS infrastructure, so as to ensure the use of common parameters, like particle  
 1134 masses and decay widths, and to facilitate reproducibility. From job option scripts at  
 1135 the user-level, the interface writes the standard input cards readable by the MC pro-  
 1136 grams, and launches the event generation itself. The intermediate output at parton-level  
 1137 (from the hard ME) is saved as Les Houches Event (LHE) files, and the generation of  
 1138 fully showered and hadronized particle-level events (EVNT/e-tag) is referred to as **evgen**.  
 1139 Next, the simulation of events from particle- to detector-level happens in two phases:  
 1140 **simul** (s/a-tags) and **reco** (r-tag). The actual simulation (the evolution of the particles  
 1141 in the ATLAS magnetic field and the generation of the detector response) is handled  
 1142 by the GEANT4 [146] program: it contains the whole detector geometry and reproduces  
 1143 the particle hits in the subdetectors, accounting for detection efficiency. Because of the  
 1144 enormous computing time needed to produce hits from the hundreds of particles at play,  
 1145 an alternative is to parametrize the detector response without running a full event sim-  
 1146 ulation (so-called ATLFAST [147] simulation). The output of the **simul** step is a **HITS**  
 1147 file. Then, as happens with the real data in the **reco** stage, signals simulated in the  
 1148 subdetectors are digitized, and the physics objects reconstructed to produce the **xAOD**  
 1149 format mentioned above. DxAODs derivations can be constructed for the latter and  
 1150 serve as input to the analyses, like the datasets which will be introduced in Chapter 9.



1151

## Part II

1152

# Top-Quark Mass Determinations



## 6 Theoretical predictions for $t\bar{t}$ final-states

The top-quark pairs created e.g. at the LHC are not observable *per se*. The only directly measurable quantities are the kinematic properties of their decay products. The top-quark has a decay branching ratio of 99.8% for  $t \rightarrow W^+ b$ ,  $\bar{t} \rightarrow W^- \bar{b}$ . So, the final-state contains two  $b$ -jets that can be experimentally tagged, and depends only on the decay mode of the  $W$  bosons. In the case of top-quark pair production, both  $W$  bosons can decay either hadronically or leptonically, with branching ratios  $\Gamma(W \rightarrow q\bar{q}') = 0.67$ ,  $\Gamma(W \rightarrow \ell\nu_\ell) = 0.33$ : the final-state can either be dileptonic, monoleptonic (lepton+jets) or all-hadronic, and the top-quark properties must then be reconstructed from the measured final-states. Fig. 6.1 depicts the topology of the three decay channels and Table 6.1 gives an overview of their respective cross-sections, advantages and disadvantages.

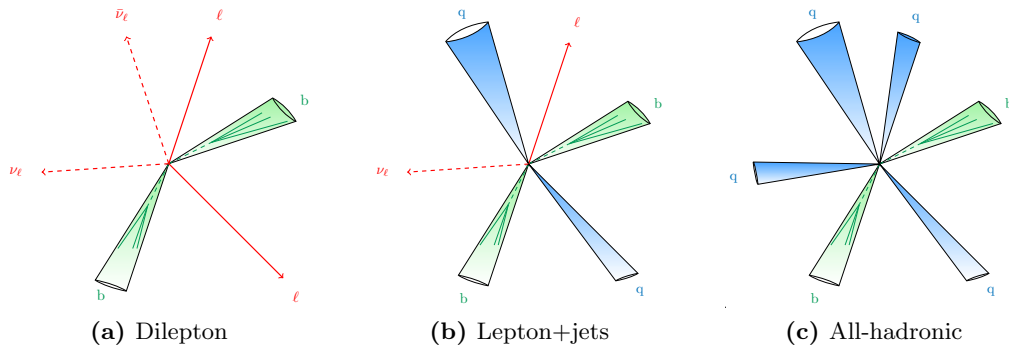


**Figure 6.1:** Topologies for  $t\bar{t}$  events are either stemming from (a) dileptonic, (b) monoleptonic or (c) all-hadronic decays.

A precise computation for top-quark pair production cross-section and differential observables is of paramount importance for the extraction of top-quark properties. Most theoretical systematic uncertainties are well under control and have been the subject of various studies in the last few years [157–160]. In this Chapter, we first review the different theoretical descriptions of  $pp \rightarrow t\bar{t}$  production, summarize the most important issues and discuss their potential impact on the extraction of top-quark properties from data, with a special focus on the top-quark observables. To do so in a realistic and quantitative way, we setup an analysis close to the ATLAS 8 TeV top-quark mass extraction in the dilepton channel. The dilepton channel is the cleanest decay mode for an experimental measurement of the top-quark mass with the possibility of requiring two high-momentum leptons whose momenta are well-reconstructed. It has the advantage of a small background (coming mainly from fake leptons, diboson and  $Z$ +jets production) and a clean signature, but suffers from the small branching fraction ( $\Gamma \sim 4.8\%$  for  $e/\mu$  in

## 6 Theoretical predictions for $t\bar{t}$ final-states

Final-state $X$	dilepton (w. $\tau^+\tau^-$ )	$\ell+$ jets (w. $\tau+j$ )	all-hadronic	all channels
$\Gamma(t\bar{t} \rightarrow X) [\%]$	10.89	44.02	44.89	100.0
$\sigma_{\text{NNLO}} [\text{pb}]$	90.58	366.14	373.38	$831.76^{+2.37\%}_{-3.51\%}$
Advantages	Clean signature	Full reconstruction	Largest branching	
Drawbacks	No full reconstruction	Jet-scale uncertainties	QCD background	
References	[148–150], [151, 152]	[149, 153], [5]	[154], [155]	

**Table 6.1:** For the three decay channels in  $t\bar{t}$  production, the branching ratios and inclusive theoretical cross-sections at QCD NNLO were computed with the Top++ program [156] for a top-quark mass  $m_t = 172.5$  GeV. Advantages and drawbacks of (any) top-quark measurement in said channel are given. References for ATLAS measurements of the top-quark mass in particular are also laid out for each subchannel for the top-quark pole mass (in black), and for the MC mass (in blue) from template fits.

the final-state). Cross-sections for all considered theoretical descriptions of  $t\bar{t}$  final-states are given at the end of the Chapter for the fiducial cuts employed in our analysis.

### 6.1 The narrow-width approximation (NWA)

Considering the intermediate state  $W^+W^-b\bar{b}$ , it makes sense at first to approximate it and examine only on-shell, doubly-resonant top-quark diagrams: the cross-section contribution stemming from non-resonant diagrams is expected to be of the order of  $\mathcal{O}(\Gamma_t/m_t) \leq 1\%$ , and usually neglecting other contributions is fine. This description is called the *narrow-width approximation* (NWA), and it builds on the limit  $\Gamma_t \rightarrow 0$ , where the top-quark propagator can then be written as

$$\lim_{\Gamma_t \rightarrow 0} \frac{1}{(p^2 - m_t^2) + m_t^2 \Gamma_t^2} = \frac{\pi}{m_t \Gamma_t} \delta(p^2 - m_t^2) + \mathcal{O}\left(\frac{\Gamma_t}{m_t}\right). \quad (6.1)$$

That is, top-quark production and decay entirely factorize, i.e.:

$$\begin{aligned} \mathcal{M}_{pp \rightarrow W^+W^-b\bar{b}} &= \mathcal{M}_{pp \rightarrow t\bar{t} \rightarrow W^+W^-b\bar{b}}^{\text{NWA}} + \mathcal{O}(\Gamma_t/m_t) \\ &= \mathcal{P}_{pp \rightarrow t\bar{t}} \otimes \mathcal{D}_{t \rightarrow W^+b} \otimes \mathcal{D}_{\bar{t} \rightarrow W^-\bar{b}} + \mathcal{O}(\Gamma_t/m_t), \end{aligned} \quad (6.2)$$

where  $\mathcal{P}$  denotes the  $t\bar{t}$  production and  $\mathcal{D}$  the top-quark decay dynamics, and the spin correlations are correctly taken into account as indicated by the symbol  $\otimes$ . The corresponding three LO Feynman diagrams, as well as a few examples of one-loop diagrams for  $gg \rightarrow t\bar{t}$  production, are shown in Fig. 6.2. Nowadays, most of the theoretical predictions used for the extraction of top-quark properties in experimental analyses rely on NLO matrix-elements for top-quark pair production only. The top-quark decay and all subsequent radiation is left to the MC generator, with the approximations it entails: particle decay usually only has LO accuracy, spin correlations (in particular in the parton-shower) were only recently implemented, and resummation is as good as the shower algorithm's

## 6.1 The narrow-width approximation (NWA)

accuracy. Even so, there exists a number of more complete MC implementations for  $t\bar{t}$  production in the NWA: the effects of NLO corrections to both production and decay were investigated in the POWHEG-BOX-v2 [17–19] framework called `ttb_NLO_dec` [161]. The `Herwig7.1` MC generator supports a new multijet merging algorithm adapted to  $t\bar{t}$  production at NLO [162], and finally the `SHERPA` generator allows for the matching of the CS shower to  $t\bar{t}$  production with 1-, 2- and 3-jets at NLO [163, 164].

Furthermore, some dedicated calculations have appeared over the years. In particular, QCD NNLO corrections for  $t\bar{t}$  production have been calculated for differential distributions [165–167], and combined with NLO EW corrections [168]. For a review of NLO EW effects, see Refs. [169–171]. Leaving corrections in top-quark pair production and considering now the top-quark decay, it was later shown that higher-order corrections to the top-quark decay have a measurable impact on differential distributions in certain regions of phase-space. NLO radiative corrections to the top-quark decays were computed [172–174] and completed by NNLO QCD corrections [175, 176], NNLL resummation and other improvements above higher-order corrections in  $\alpha_s$  [177–182]. Within the NWA, the calculation of QCD NNLO + NNLL' (soft-gluon and small-mass resummation) corrections for differential distributions was combined with NLO EW corrections and is the most complete fixed-order calculation up-to-date [183].

For the results shown in Section 6.5 in the NWA, the top-quark pair production is described at NLO QCD and factorizes from the top-quark decay. Furthermore, we consider only the  $e\mu$  dilepton channel, that is  $pp \rightarrow (e^+\nu_e)(\mu^-\bar{\nu}_\mu)b\bar{b}$  production for the analysis presented in Chapter 7. The top-quark decay accuracy is handled in three different ways.

- (1) Top-quark decay at LO is realized in the fixed-order `SHERPA` setup, as in Ref. [184] (referred to as **NLO<sub>NWA</sub><sup>LOdec</sup>** from now on).
- (2) The top-quark decay at NLO is computed in Ref. [173], and is shortly described below (**NLO<sub>NWA</sub><sup>NLOdec</sup>**).
- (3) The top-quark decay is handled by the parton-shower, namely through the `SHERPA` CSS shower (**NLO<sub>PS</sub>**).

Briefly, the **NLO<sub>NWA</sub><sup>NLOdec</sup>** calculation in the NWA is based on the following formula [173] where top-quark pair production and decay factorize. Taking the perturbative expansion of Eq. (6.2) to NLO gives

$$\begin{aligned} \mathcal{M}_{ij \rightarrow t\bar{t} \rightarrow b\bar{b}2\ell 2\nu}^{NWA, NLO} = & \mathcal{P}_{ij \rightarrow t\bar{t}}^{\text{LO}} \otimes \mathcal{D}_{t \rightarrow b\ell^+\nu}^{\text{LO}} \otimes \mathcal{D}_{\bar{t} \rightarrow \bar{b}\ell^-\bar{\nu}}^{\text{LO}} + \mathcal{P}_{ij \rightarrow t\bar{t}}^{\delta\text{NLO}} \otimes \mathcal{D}_{t \rightarrow b\ell^+\nu}^{\text{LO}} \otimes \mathcal{D}_{\bar{t} \rightarrow \bar{b}\ell^-\bar{\nu}}^{\text{LO}} \\ & + \mathcal{P}_{ij \rightarrow t\bar{t}}^{\text{LO}} \otimes \left( \mathcal{D}_{t \rightarrow b\ell^+\nu}^{\delta\text{NLO}} \otimes \mathcal{D}_{\bar{t} \rightarrow \bar{b}\ell^-\bar{\nu}}^{\text{LO}} + \mathcal{D}_{t \rightarrow b\ell^+\nu}^{\text{LO}} \otimes \mathcal{D}_{\bar{t} \rightarrow \bar{b}\ell^-\bar{\nu}}^{\delta\text{NLO}} \right), \end{aligned} \quad (6.3)$$

where LO,  $\delta$ NLO represent the LO, respectively NLO contributions to the  $t\bar{t}$  production and top-quark decays.

As mentioned above, the NWA is expected to be precise enough for most calculations and yet, NLO and off-shell effects in the top-quark decay can have an important impact

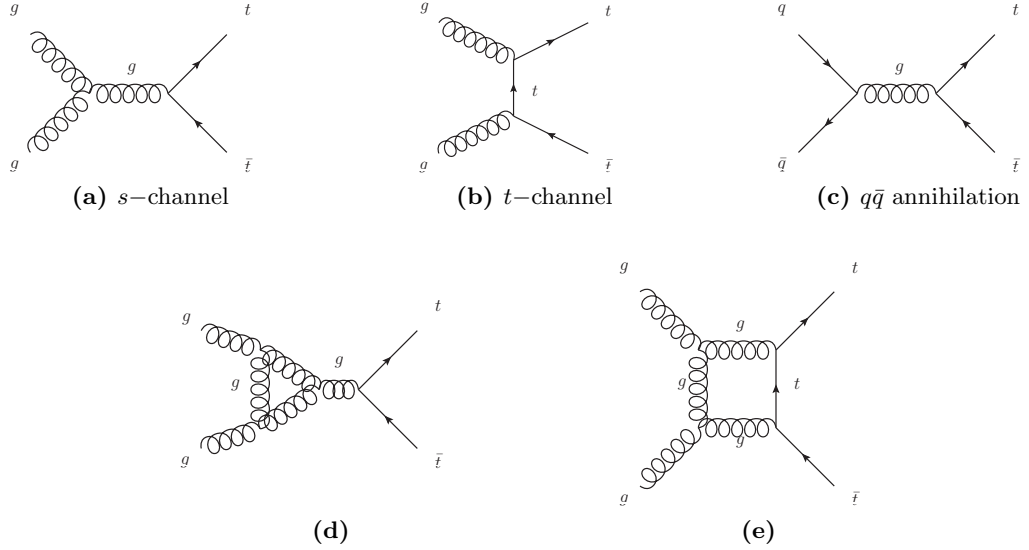


**Figure 6.2:** (a-c) Leading-order diagrams for  $t\bar{t}$  production and (d-e) two examples of NLO QCD one-loop diagrams for  $gg \rightarrow t\bar{t}$

on sensitive regions of phase-space. In practice, experimental analyses do account for part of the non-doubly-resonant contributions: they include single-top quark production in the signal, since it contributes to the same final-state at NLO, or they subtract it consistently as background. To take care of the interference between  $t\bar{t}$  and single-top diagrams, this is generally accomplished with the help of a diagram subtraction (DS) or diagram removal (DR) scheme [185]. This procedure is not entirely free of quirks and violates gauge-invariance. To get an entirely consistent theoretical prediction, it is therefore preferable to produce the full intermediate state  $pp \rightarrow W^+W^-b\bar{b}$ , which contains the fully complete set of Feynman diagrams at NLO.

## 6.2 $W^+W^-b\bar{b}$ production: review of existing calculations

In this Section, we shall describe the setup used for calculating NLO QCD corrections to the  $pp \rightarrow W^+W^-b\bar{b}$  process, which is computationally more demanding than  $pp \rightarrow t\bar{t}$  production in the NWA. The full calculation at NLO contains all doubly-resonant top-quark diagrams, but also non-doubly resonant as well as non-factorizing contributions. Fig. 6.3 illustrates some of the additional Feynman diagrams.

At LO, the full  $W^+W^-b\bar{b}$  final-state including the non-resonant diagrams has been computed in Refs. [184, 186–188]. In general, the calculation of NLO corrections poses some technical problems because of the existence of  $b$ -quarks in both initial- and final-state. In the 5-flavour scheme (5FNS), where  $b$ -quarks are treated as massless, collinear  $g \rightarrow b\bar{b}$  splittings contribute to the final-state and the corresponding IR divergence has to be handled (see Section 6.3). Considering massive  $b$ -quarks (4FNS) has the

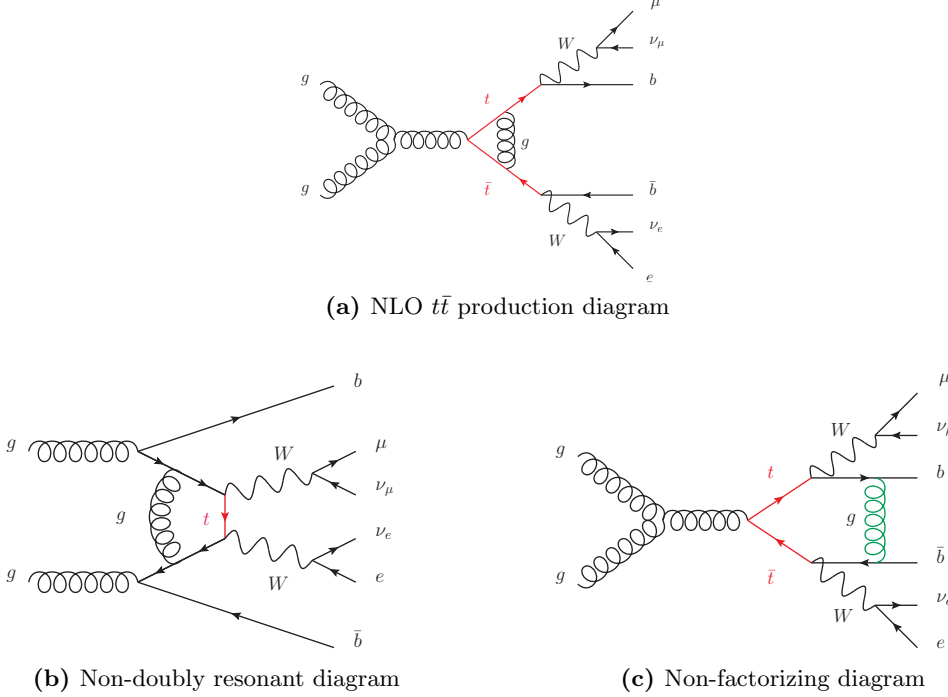


**Figure 6.3:** One-loop diagrams for  $pp \rightarrow W^+W^-b\bar{b}$  production contain (a) NLO corrections to standard NWA  $t\bar{t}$  production, but also (b) diagrams with one or no top-quark propagators and (c) resonant diagrams with non-factorizing legs

advantage of allowing any phase space restrictions on the  $b$ -quarks without endangering infrared safety, and thus allows to consider exclusive 0, 1- and 2-jet bins for  $pp \rightarrow (e^+\nu_e)(\mu^-\bar{\nu}_\mu)b\bar{b}$  in the same setup. On the other hand, massive  $b$ -quarks are accompanied by an additional mass scale to the one-loop integrals and thus renders the integral evaluation less straightforward. In Refs. [189, 190], NLO calculations in the 4FNS have been performed.

Often, the  $W^+W^-b\bar{b}$  prediction differs from the NWA in phase-space regions accessible only at NLO or sensitive to the top-quark decay kinematics. In Ref. [184], particular emphasis has been put on the impact of the non-factorising contributions on the top quark mass measurements in the dilepton channel. Recently the calculation of the NLO QCD corrections to  $W^+W^-b\bar{b}$  production with full off-shell effects has also been achieved in the lepton+jets channel [191].

### 6.3 $W^+W^-b\bar{b}$ calculation setup at NLO QCD

The calculation is analogous to the one described in Ref. [192]. We compute the NLO QCD corrections to the  $pp \rightarrow W^+W^-b\bar{b} \rightarrow (e^+\nu_e)(\mu^-\bar{\nu}_\mu)b\bar{b}$  process, i.e. up to  $\mathcal{O}(\alpha_s^2\alpha^2)$ , in the 5-flavour scheme. This means that interference from (massless)  $b$ -quarks in the initial-state is taken into account. Top-quark finite width effects are fully included. The

## 6 Theoretical predictions for $t\bar{t}$ final-states

1270 complex mass scheme is used to incorporate the width in a gauge-invariant way, where  
 1271 the top-quark mass is replaced by a complex number  $\mu_t$ :

$$\mu_t^2 = m_t^2 - im_t\Gamma_t. \quad (6.4)$$

1272 The  $W$  and intermediate  $Z$  bosons also acquire a complex mass. Note that we consider  
 1273 only resonant  $W$  boson diagrams: non-resonant contributions and finite- $W$ -width effects  
 1274 were found to be small compared to top-quark effects [193]. The calculation is realized  
 1275 at parton-level within the SHERPA v2.2.3 framework,<sup>1</sup> where we used tree-level and real  
 1276 amplitudes from SHERPA matrix-element generators COMIX and AMEGIC. The one-loop  
 1277 amplitudes are compiled by GoSAM and linked to SHERPA via the BLHA interface.  
 1278 Finally, the IR divergences are subtracted with the help of the Catani-Seymour dipole  
 1279 formalism as automated in SHERPA.

1280 There are 334 diagrams contributing to the  $q\bar{q} \rightarrow W^+W^-b\bar{b}$  virtual corrections, where  
 1281  $q$  are the light quarks  $u, d, s, c$ , and 1068 diagrams contributing to  $gg \rightarrow W^+W^-b\bar{b}$ .  
 1282 Additionally, because of the  $b$ -quarks present in the initial-state, 668 one-loop diagrams  
 1283 contribute to  $b\bar{b} \rightarrow W^+W^-b\bar{b}$ .

1284 In the results presented in Chapters 7 and 8, the full  $pp \rightarrow W^+W^-b\bar{b} \rightarrow (e^+\nu_e)(\mu^-\bar{\nu}_\mu)b\bar{b}$   
 1285 QCD NLO prediction is compared with various  $t\bar{t}$  predictions in the NWA. To disentangle the effects from production and decay corrections (as well as extra radiation in  
 1286 a parton-shower resummed approximation), the four theoretical descriptions considered  
 1287 in the next Chapter are summarized again for completeness:

1289 **NLO<sub>full</sub>**: full NLO corrections to  $pp \rightarrow W^+W^-b\bar{b}$  with leptonic  $W$ -decays,

1290 **NLO<sub>NWA</sub><sup>NLOdec</sup>**: NLO  $t\bar{t}$  production  $\otimes$  NLO decay,

1291 **NLO<sub>NWA</sub><sup>LOdec</sup>**: NLO  $t\bar{t}$  production  $\otimes$  LO decay,

1292 **NLO<sub>PS</sub>**: NLO  $t\bar{t}$  production+shower  $\otimes$  decay via parton showering.

1293 Note that the three first theoretical descriptions are not matched to a parton-shower  
 1294 at all. The PDF4LHC15\_nlo\_30\_pdfas sets are interfaced to SHERPA via LHAPDF and  
 1295 events are produced at a center-of-mass energy of  $\sqrt{s} = 13$  TeV. The central top-quark  
 1296 mass was set to  $m_t = 172.5$  GeV and the  $G_\mu$ -electroweak scheme was used with the  
 1297 following numerical values:

$$G_\mu = 1.16637 \cdot 10^{-5} \text{ GeV}^{-2}, \quad M_W = 80.385 \text{ GeV}, \quad M_Z = 91.1876 \text{ GeV}, \quad (6.5)$$

$$\begin{aligned} \Gamma_t^{\text{LO}} &= & 1.4806 \text{ GeV}, & \Gamma_t^{\text{NLO}} &= & 1.3535 \text{ GeV}, \\ \Gamma_W^{\text{LO}} &= & 2.0454 \text{ GeV}, & \Gamma_W^{\text{NLO}} &= & 2.1155 \text{ GeV}, \\ \Gamma_Z &= & 2.4952 \text{ GeV}, \end{aligned} \quad (6.6)$$

1298 where the LO (NLO) widths were used for the LO (NLO) decays, respectively.

---

<sup>1</sup>A patched version [194] was used for the CSS shower, with the correct eikonal expressions for radiating off massive top-quarks (relevant only for the NLO<sub>PS</sub> description).

## 1299 6.4 Event requirements

1300 To give a more quantitative assessment of the difference between our predictions with  
 1301 respect to the extracted top-quark mass, we implement an analysis that is similar to  
 1302 the ATLAS top-quark mass measurement in the dilepton channel at 8 TeV [195], where  
 1303 the trigger cuts on leptons and jets are adapted to the ATLAS 13 TeV standards. For  
 1304 details of the analysis, the reader is referred to Chapter 7. We require:

- 1305 •  $n_{b,\text{jets}} = 2$  with  $p_T^{\text{jet}} > 25 \text{ GeV}$  and  $|\eta^{\text{jet}}| < 2.5$ . Jets are clustered with **FastJet** [196,  
 1306 197] using a jet radius parameter of  $\Delta R = 0.4$ . Jets containing a  $b\bar{b}$  pair are also  
 1307 defined as  $b$ -jets.

- 1308 • exactly two oppositely charged leptons which fulfill  $p_T^\mu > 28 \text{ GeV}$ ,  $|\eta^\mu| < 2.5$  for  
 1309 muons and  $p_T^e > 28 \text{ GeV}$ ,  $|\eta^e| < 2.47$  for electrons excluding the dead region  
 1310  $1.37 < |\eta^e| < 1.52$  between barrel and endcap EM calorimeters. For charged  
 1311 leptons we require a separation of  $\Delta R(\ell, \text{jet}) > 0.4$  to any jet.

- 1312 •  $p_T^{\ell b} > 120 \text{ GeV}$ . Using the same lepton- $b$ -jet assignments as for  $m_{\ell b}$ , we define  $p_T^{\ell b}$   
 1313 as the average transverse momentum of both lepton- $b$ -jet systems.

1314 We chose  $\mu_R = \mu_F = m_t$  as our central scale. The scale variation bands are obtained  
 1315 by varying  $\mu_{R,F} = c_{R,F} m_t$ , with  $(c_R, c_F) \in \{(0.5, 0.5), (2, 2)\}$ .<sup>2</sup>

In the NWA parton-shower results, the central scale was also compared to a dynamic scale called  $\mu_{t\bar{t}}$ . The latter is a “colour-flow inspired” QCD scale suggested in Ref. [198]. For the Mandelstam invariants  $s$ ,  $t$  and  $u$ , the dynamic scale is given by

$$\mu_{t\bar{t}}^2(q\bar{q} \rightarrow t\bar{t}) = 2 p_q p_t = m_t^2 - t , \quad (6.7)$$

$$\mu_{t\bar{t}}^2(\bar{q}q \rightarrow t\bar{t}) = 2 p_{\bar{q}} p_t = m_t^2 - u , \quad (6.8)$$

$$\mu_{t\bar{t}}^2(gg \rightarrow t\bar{t}) = \begin{cases} m_t^2 - t & w_1 \propto \frac{u-m_t^2}{t-m_t^2} + \frac{m_t^2}{m_t^2-t} \left\{ \frac{4t}{t-m_t^2} + \frac{m_t^2}{s} \right\} \\ m_t^2 - u & w_2 \propto \frac{t-m_t^2}{u-m_t^2} + \frac{m_t^2}{m_t^2-u} \left\{ \frac{4u}{u-m_t^2} + \frac{m_t^2}{s} \right\} \end{cases} \quad (6.9)$$

- 1316 the value of  $\mu_{t\bar{t}}$  being chosen with a probability proportional to the two weights  $w_1$ ,  $w_2$ .

---

<sup>2</sup>Also, 7-point variations were considered but the simultaneous variations are identical to their envelope.

## 1317 6.5 Total cross-section results

1318 The fiducial cross-sections after applying the aforementioned cuts are given in Table 6.2  
 1319 for all considered predictions, where we also add production at LO accuracy for com-  
 1320 pleteness. The renormalization and factorization scale uncertainties are given in percent.

	X=LO [fb]	X=NLO [fb]
$\mathbf{X}_{\text{full}}$	$(739.5 \pm 0.3)^{+31.5\%}_{-22.4\%}$	$(914 \pm 3)^{+2.1\%}_{-7.6\%}$
$\mathbf{X}_{\text{NWA}}^{\text{LOdec}}$	$(727.3 \pm 0.2)^{+31.4\%}_{-22.3\%}$	$(1029 \pm 1)^{+10.4\%}_{-11.5\%}$
$\mathbf{X}_{\text{NWA}}^{\text{NLOdec}}$	-	$(905 \pm 1)^{+2.3\%}_{-7.7\%}$
$\mathbf{X}_{\text{PS}}, \mu = m_t$	$(637.7 \pm 0.9)^{+29.7\%}_{-21.0\%}$	$(886 \pm 1)^{+8.5\%}_{-9.3\%}$
$\mathbf{X}_{\text{PS}}, \mu = \mu_{t\bar{t}}$	$(499.7 \pm 0.7)^{+27.6\%}_{-19.3\%}$	$(805.2 \pm 0.9)^{+12.3\%}_{-10.9\%}$

1321 **Table 6.2:** Cross-sections for all predictions at LO, respectively NLO in production, where the  
 1322 top-quark mass  $m_t = 172.5$  GeV. The uncertainty stemming from MC integration  
 1323 is given in parentheses, and scale variation uncertainties are shown in percent.

1324 While the cross-sections for NLO<sub>full</sub> and NLO<sub>NWA</sub><sup>NLOdec</sup> agree with each other within  
 1325 expectations, the NLO<sub>NWA</sub><sup>LOdec</sup> cross-section is about 13% higher than the latter. The  
 1326 NLO<sub>PS</sub> cross-section, in comparison, is smaller because of the softening of  $b$ -jets which  
 1327 leads to a higher rejection rate when taking jet requirements into account. The  $\mu_{t\bar{t}}$   
 1328 scale is larger than the central scale  $m_t$ , thus the even smaller cross-section for this  
 1329 scale choice. Notice also the reduction in the renormalization and factorization scale  
 1330 uncertainties when including NLO corrections to the top-quark decay. Usually, rather  
 1331 than total inclusive cross-sections, the most sensitive top-quark mass measurements  
 1332 rely on differential distributions, where mostly the distributions for  $t\bar{t}$  final-states are  
 1333 MC-generated and *fitted* to extract the top-quark mass (see the full explanation of  
 1334 the method in Chapter 7). One caveat of considering differential distributions is that  
 1335 the measured top-quark mass is rather represented by the MC input top-quark mass  
 1336 parameter  $m_t^{\text{MC}}$ , instead of the top-quark pole mass (or any other QFT-defined mass)  
 1337 measured in inclusive  $t\bar{t}$  measurements.

1338 Leaving the difference between heavy-quark mass schemes aside, we detail the exact  
 1339 procedure used in current ATLAS analyses for measuring the MC top-quark mass in  
 1340 the next Chapter, along with quantitative comparisons of the theoretical predictions  
 1341 outlined above.

# <sup>1339</sup> 7 NWA versus $W^+W^-b\bar{b}$ : Top-quark mass <sup>1340</sup> uncertainties at parton-level

<sup>1341</sup> This Chapter shall investigate quantitatively the effect of using the different theoretical  
<sup>1342</sup> predictions presented above in a top-quark mass extraction. We base our measurement  
<sup>1343</sup> method on the ATLAS 8 TeV analysis in the dilepton channel [195], where we adapted  
<sup>1344</sup> the ATLAS cuts to the 13 TeV center-of-mass energy. This Chapter first introduces  
<sup>1345</sup> the template fit method that was used in the experimental measurement. After a short  
<sup>1346</sup> discussion of important features of the considered observables, the results for the fit of  
<sup>1347</sup> the top-quark mass and its dependence on the different theoretical descriptions of the  
<sup>1348</sup>  $t\bar{t}$  dilepton final-state are laid out.

## <sup>1349</sup> 7.1 The template fit method

<sup>1350</sup> In the dilepton channel, the top-quark momenta cannot be fully reconstructed in the  
<sup>1351</sup> experiment because of the two-particle spectrum spread given by the neutrinos from both  
<sup>1352</sup>  $W$ -decays. One successful method is to use a differential distribution that is sensitive  
<sup>1353</sup> to the top-quark mass instead and which can be defined without having to properly  
<sup>1354</sup> reconstruct the top-quark intermediate states. The procedure is the following:

- <sup>1355</sup> • Choose a distribution that is sensitive to the theoretical top-quark mass: for ex-  
<sup>1356</sup> ample, we choose the average invariant mass of the lepton- $b$ -jet system  $m_{\ell b}$  (which  
<sup>1357</sup> make up the visible top-quark decay products) as a function of the top-quark mass  
<sup>1358</sup> set in the MC event generator.
- <sup>1359</sup> • Generate distributions for different input top-quark masses  $m_t^{\text{in}}$ . These are called  
<sup>1360</sup> *template* distributions.
- <sup>1361</sup> • Individually fit the template distributions simulated for the input masses  $m_t^{\text{in}}$  with  
<sup>1362</sup> an appropriate function. If we consider the simple example of a Gaussian fit, this  
<sup>1363</sup> gives:

$$\mathcal{G}(A, \mu, \sigma; m_t^{\text{in}}) = A(m_t^{\text{in}}) \exp \left( -\frac{(\mu(m_t^{\text{in}}) - m_t^{\text{in}})^2}{2\sigma^2(m_t^{\text{in}})} \right), \quad (7.1)$$

<sup>1364</sup> where the parameters  $A, \mu, \sigma$  are fit to the distributions generated for each input  
<sup>1365</sup> mass.

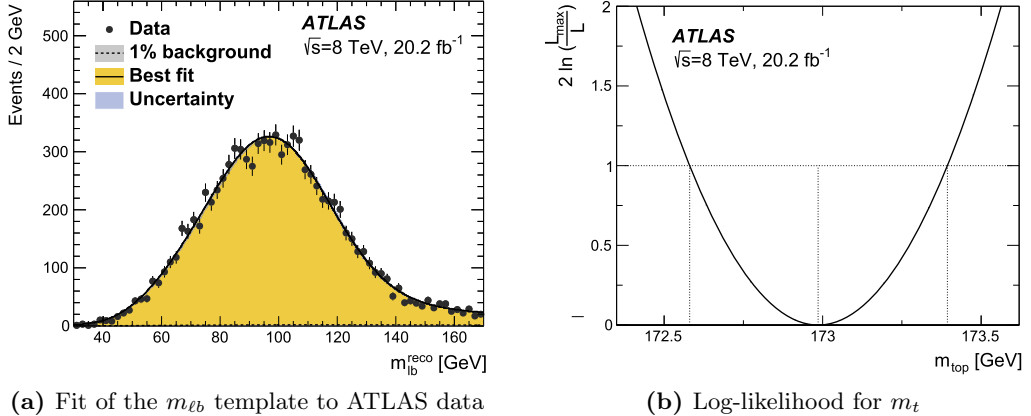


**Figure 7.1:** (a) The ATLAS 8 TeV analysis generates template distributions for  $m_{lb}$  for different input top-quark masses. These are fitted by a suitable function which parameters are expressed as linearly-dependent functions of  $m_t$ . (b) The likelihood function for  $m_t$  is then maximized in an unbinned fit to the measured  $m_{lb}$  distribution to extract the top-quark mass (Figures from Ref. [195]).

1366 This step is called *calibration* in the following paragraphs, and the functions for each  
 1367 of the input top-quark masses are called calibration functions. The dependence of the  
 1368 parameters on  $m_t^{\text{in}}$  is assumed to be linear, a fact that is checked against the MC  
 1369 prediction. Once it is confirmed, the linear dependence is imposed (in our example,  
 1370  $A(m_t^{\text{in}}) = a + b \cdot m_t^{\text{in}}$  with  $a$  and  $b$  fixed, and analogously for  $\mu(m_t^{\text{in}})$ ,  $\sigma(m_t^{\text{in}})$ ). The  
 1371 underlying linear parameters are then kept constant, and the only free parameter is the  
 1372 extracted top-quark mass  $m_t = m_t^{\text{out}}$  to be measured. This function can then be used  
 1373 directly in an unbinned likelihood fit to the distribution measured in experimental data,  
 1374 as shown in Fig. 7.1 as an illustration from the ATLAS 8 TeV measurement.

1375 For a satisfying modeling of the  $m_{lb}$  distribution, the sum of a Gaussian and a Landau  
 1376 distribution is used in the analysis. In practice, the overall normalization factor is fit to  
 1377 the measured cross-section after cuts are applied. In the rest of this Chapter, we repeat  
 1378 the extraction from a custom analysis implemented in *Rivet* [199] similar to the one  
 1379 performed by ATLAS, for the four different theoretical setups presented in Chapter 6  
 1380 at parton-level (at particle-level for the parton-showered  $t\bar{t}$  results). We also compare  
 1381 different observables in addition to  $m_{lb}$ .

## 1382 7.2 Definition of the observables

1383 The results presented in the rest of this Chapter were published in Ref. [200]. The reader  
 1384 is referred to the latter for details that are omitted in the following. We study a list of  
 1385 observables that should in principle be maximally sensitive to the top-quark mass while  
 1386 minimally sensitive to theoretical systematic uncertainties (that is, including differences  
 1387 between NWA and full  $W^+W^-b\bar{b}$  predictions):

## 7.2 Definition of the observables

- 1388 •  $m_{\ell b}$  – the invariant mass of the two lepton- and  $b$ -jet systems

$$m_{\ell b}^2 = (p_\ell + p_b)^2. \quad (7.2)$$

1389 Since both top-quarks decay leptonically and there is no possibility to determine  
 1390 the charge of the  $b$ -jets experimentally, there is an ambiguity in the assignment of  
 1391 the lepton and  $b$ -jet to the two top-quarks. We use here the same criterion as the  
 1392 ATLAS analysis: the two possible pairs for the lepton- $b$ -jet system  $(\ell^+ b_1, \ell^- b_2)$  are  
 1393 tried out, and we choose the pairing that minimizes the sum of the two  $m_{\ell b}$  values  
 1394 per event, and take the average of both.

- 1395 •  $m_{T2}$  – following Refs. [201, 202] in the case of the final-state  $(e^+\nu_e)(\mu^-\bar{\nu}_\mu)b\bar{b}$ , the  
 1396 definition of this variable is given by

$$m_{T2}^2 = \min_{p_T^{\nu_1} + p_T^{\nu_2} = p_T^{\text{miss}}} \left[ \max \left\{ m_T^2 \left( p_T^{(\ell^+ b_1)}, p_T^{\nu_1} \right), m_T^2 \left( p_T^{(\ell^- b_2)}, p_T^{\nu_2} \right) \right\} \right]. \quad (7.3)$$

1397 The same pairing as for  $m_{\ell b}$  is chosen for the lepton and  $b$ -jet systems, and the  
 1398 transverse mass is defined as

$$m_T^2 \left( p_T^{(\ell b_i)}, p_T^{\nu_i} \right) = m_{(\ell b_i)}^2 + 2 \left( E_T^{(\ell b_i)} E_T^{\nu_i} - p_T^{(\ell b_i)} p_T^{\nu_i} \right), \quad (7.4)$$

1399 with  $E_T = \sqrt{|p_T|^2 + m^2}$  and we set  $m_{\nu_i} = 0$ .

- 1400 •  $E_T^{\Delta R}$  – the lepton transverse energy weighted by the angular distance to the cor-  
 1401 responding  $b$ -jet

$$E_T^{\Delta R} = \frac{1}{2} \left( E_T^{l_1} \Delta R(l_1, b_1) + E_T^{l_2} \Delta R(l_2, b_2) \right), \quad (7.5)$$

1402 where again the above  $m_{\ell b}$  criterion is used.

- 1403 •  $m_{\ell\ell}$  – the invariant mass of the two-lepton system.

1404 For the NLO<sub>NWA</sub><sup>LOdec</sup>, NLO<sub>NWA</sub><sup>NLOdec</sup> and NLO<sub>full</sub> calculations, only the parton-level is con-  
 1405 sidered, including the decay products from the  $W$  bosons. The  $b$ -jets are identified with  
 1406 the  $b$ -quarks in that case. For the NLO<sub>PS</sub> prediction, the cuts and observables are de-  
 1407 fined on the parton-level output of the shower algorithm, before any hadronization but  
 1408 with the full-particle final-state. Sets of MC samples were produced for input top-quark  
 1409 masses

$$m_t \in \{165.0, 172.5, 180.0\} [\text{GeV}]. \quad (7.6)$$

1410 The dependence on the input top-quark mass  $m_t$  is shown for all four observables in  
 1411 Fig. 7.2. Whereas  $m_{\ell b}$  and  $m_{T2}$  are the most sensitive to  $m_t$  with a ratio to the central  
 1412 choice of the order  $\mathcal{O}(2-3)$  for the considered masses, the dependence of the  $E_T^{\Delta R}$  and  
 1413  $m_{\ell\ell}$  observables on the top-quark mass is rather weak.

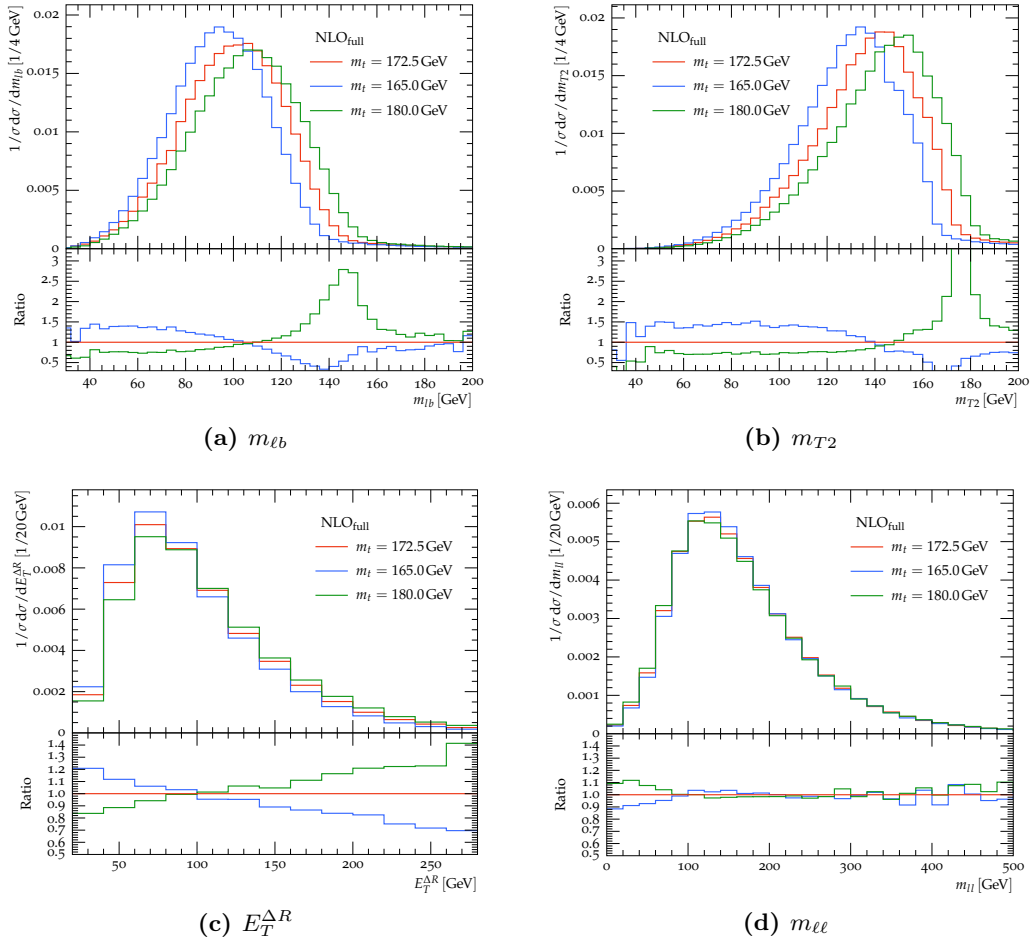


**Figure 7.2:** Differential observables are shown for three different top-mass points chosen symmetrically around  $m_t = 172.5$  GeV for the full  $W^+W^-b\bar{b}$  NLO prediction. While the (a)  $m_{lb}$  and the (b)  $m_{T2}$  observables show the highest top-mass dependence, the observables (c)  $E_T^{\Delta R}$  and (d)  $m_{\ell\ell}$  are not sensitive enough to the top-mass to be considered for the template fit.

### 1414 7.3 Comparison of the different theoretical descriptions

1415 The normalized differential cross-section for the  $m_{lb}$  observable is outlined in Fig. 7.3 for  
 1416 the four theoretical predictions presented in Chapter 6. We show the ratio to the com-  
 1417 plete  $W^+W^-b\bar{b}$  NLO<sub>full</sub> calculation, where the latter's scale uncertainties are represented  
 1418 by gray bands in the plot. Note that the  $m_{lb}$  distribution has a sharp kinematic edge at  
 1419  $m_{lb}^{\text{edge}} = \sqrt{m_t^2 - m_W^2} \sim 153$  GeV. Beyond the kinematic edge, the bins are only popu-  
 1420 lated by wrong lepton- $b$ -jet pairing, additional radiation from the initial-state clustered  
 1421 along the lepton- $b$ -jet system, and non-resonant contributions. The LO cross-section  
 1422 for  $t\bar{t}$  production vanishes in this phase-space region. Thus, because NLO corrections

### 7.3 Comparison of the different theoretical descriptions

represent the first non-trivial order contributing to this region, differences between the theoretical descriptions considered here are expected to be sizeable around and above this kinematic edge. On the other hand, as seen in Fig. 7.2, this region also displays the highest sensitivity to the top-quark mass.

In Fig. 7.3, all predictions for  $m_{\ell b}$  agree within a few percent in the bulk of the distribution,  $40 \text{ GeV} \leq m_{\ell b} \leq 140 \text{ GeV}$ , except for  $\text{NLO}_{\text{NWA}}^{\text{LOdec}}$ . The latter introduces a positive slope around and above the peak with differences of  $\mathcal{O}(-10\%)$  at small masses up to  $+20\%$  at  $\sim 140 \text{ GeV}$ , effectively shifting the peak to higher values of  $m_{\ell b}$ . This translates into an artificially higher extracted mass for the top-quark when using LO decay predictions. In contrast,  $\text{NLO}_{\text{NWA}}^{\text{NLOdec}}$  is found within 4% of the  $\text{NLO}_{\text{full}}$  prediction for the bulk of the distribution, starting to differ above the kinematic edge and stagnating at  $-50\%$  of the full prediction in the tail, as expected. Finally, for the  $\text{NLO}_{\text{PS}}$  case, the tail at high  $m_{\ell b}$ -values is populated by the additional radiation from the parton-shower, and is driven closer to  $\text{NLO}_{\text{full}}$  while it mostly lies between  $\text{NLO}_{\text{NWA}}^{\text{LOdec}}$  and  $\text{NLO}_{\text{NWA}}^{\text{NLOdec}}$  in the rest of the distribution.

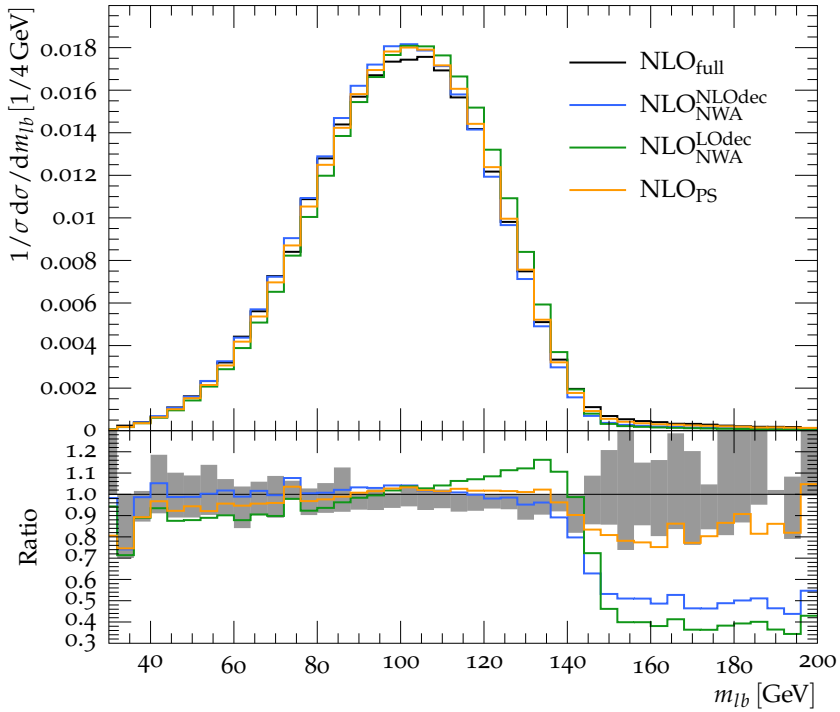


**Figure 7.3:** The normalized differential lepton- $b$ -jet system invariant mass  $m_{\ell b}$  is shown for all four theoretical predictions considered at 13 TeV, with their ratio to the  $\text{NLO}_{\text{full}}$  prediction. The gray band represents the latter's scale variation uncertainty.

Similar features can be observed for the normalized distribution of  $m_{T2}$  in Fig. 7.4 on a larger range up to the kinematic edge at  $m_{T2}^{\text{edge}} = m_t$ . In Figs. 7.5a and 7.5b, the normalized  $E_T^{\Delta R}$  and  $m_{\ell\ell}$  distributions show smaller differences between the theoretical predictions, with maximal deviations of  $\mathcal{O}(10 - 12\%)$  in the regions of lowest cross-section. Since they are much less sensitive to the top-quark mass, though, we do not consider them for the template fitting procedure in the results below.

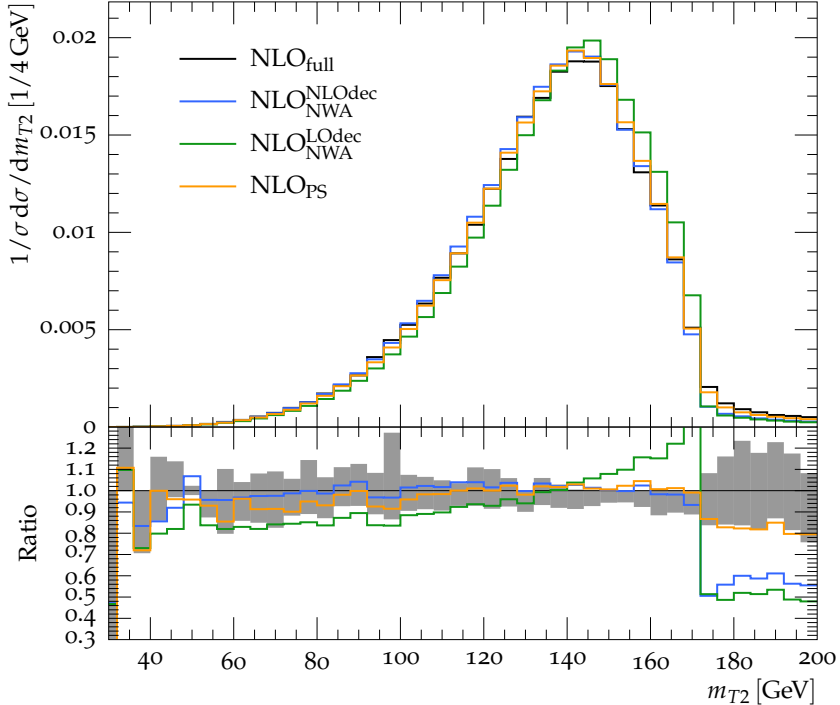


**Figure 7.4:** The normalized  $m_{T2}$  distribution is depicted for the four theoretical predictions, and shows a behavior similar to  $m_{\ell b}$ .

It is also enlightening to look at the scale dependence of our four theoretical descriptions for LO and NLO production. In Fig. 7.6a, the ratio of the  $W^+W^-b\bar{b}$  prediction  $\text{NLO}_{\text{full}}$  to  $\text{LO}_{\text{full}}$  is shown for the  $m_{\ell b}$  observable. Although large corrections are expected above the kinematic edge when going from LO to NLO in production, one finds unexpectedly important corrections in the low-mass region as well, where differences between both orders of accuracy in production are not covered by the scale uncertainties. In the NWA case shown in Fig. 7.6b, describing the top-quark decays at NLO also pushes the prediction out of the  $\text{NLO}_{\text{NWA}}^{\text{LOdec}}$  scale uncertainties. The differences between the  $\text{NLO}_{\text{NWA}}^{\text{LOdec}}$  and  $\text{NLO}_{\text{NWA}}^{\text{NLOdec}}$ , respectively  $\text{NLO}_{\text{PS}}$  are also not covered around the kinematic edge. In general, scale uncertainties in the NWA are shown to be misguidedly small in the tails of the  $m_{\ell b}$  and  $m_{T2}$  distributions. The behavior of scale-varied predictions is depicted for  $m_{T2}$ ,  $E_T^{\Delta R}$  and  $m_{\ell\ell}$  in Figs. 7.7–7.9.

Comparing the mass sensitivity in Fig. 7.2a and the systematic differences between predictions in Fig. 7.6a, the template fit strategy should be optimized to maximize the

### 7.3 Comparison of the different theoretical descriptions

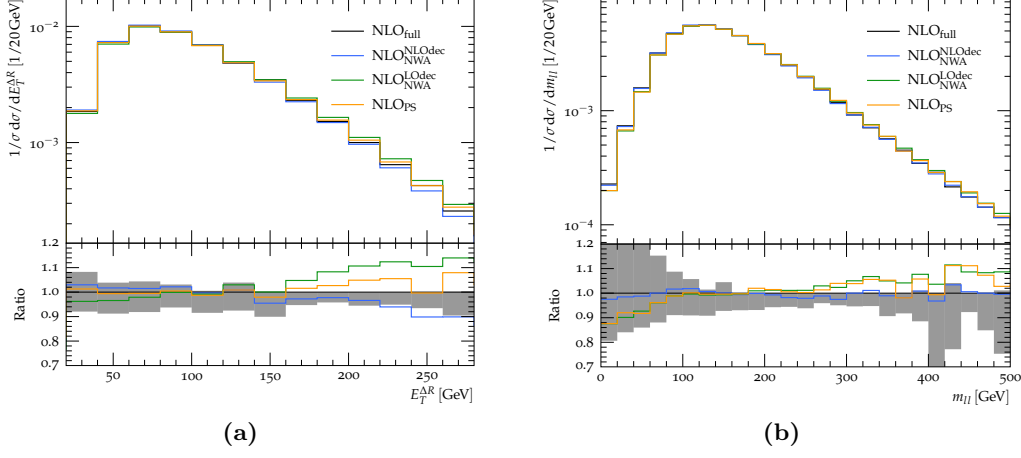


**Figure 7.5:** The normalized differential cross-sections for the (a)  $E_T^{\Delta R}$  and (b)  $m_{\ell\ell}$  distributions with all four theoretical predictions.

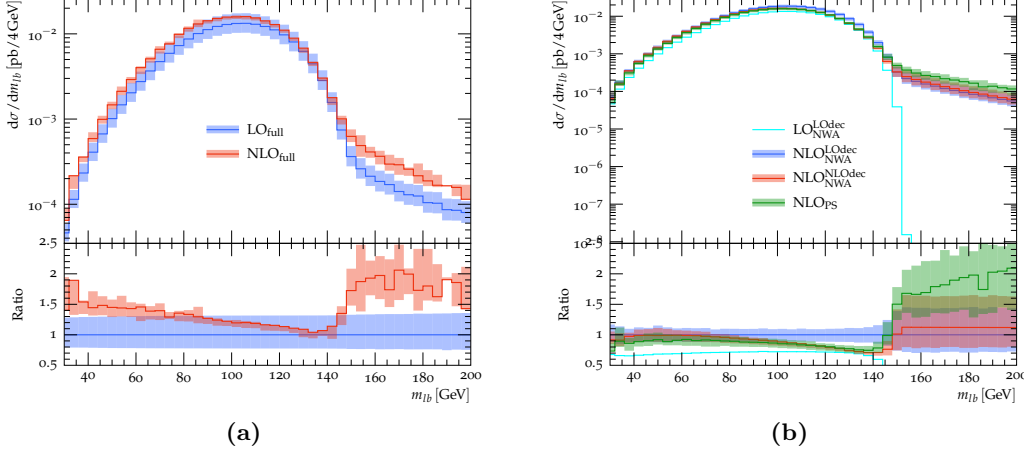


**Figure 7.6:** Results including scale variation bands for  $m_{lb}$ , for (a) the LO<sub>full</sub> and NLO<sub>full</sub> calculations, (b) the calculations based on the NWA. The ratios with respect to (a) LO<sub>full</sub> and (b) NLO<sub>NWA</sub><sup>LOdec</sup> are also shown.

1458 top-quark mass sensitivity while keeping the systematic uncertainty associated to the  
1459 theoretical predictions to a minimum. We chose the fit range to be

$$40 \text{ GeV} \leq m_{lb} \leq 160 \text{ GeV}, \quad (7.7)$$

$$80 \text{ GeV} \leq m_{T2} \leq 180 \text{ GeV}.$$

1460 The exact dependence on the fit range was investigated, where the results were repro-  
1461 duced once with a restricted range of  $m_{lb} \leq 140 \text{ GeV}$ , and numerical values were found  
1462 to be stable.

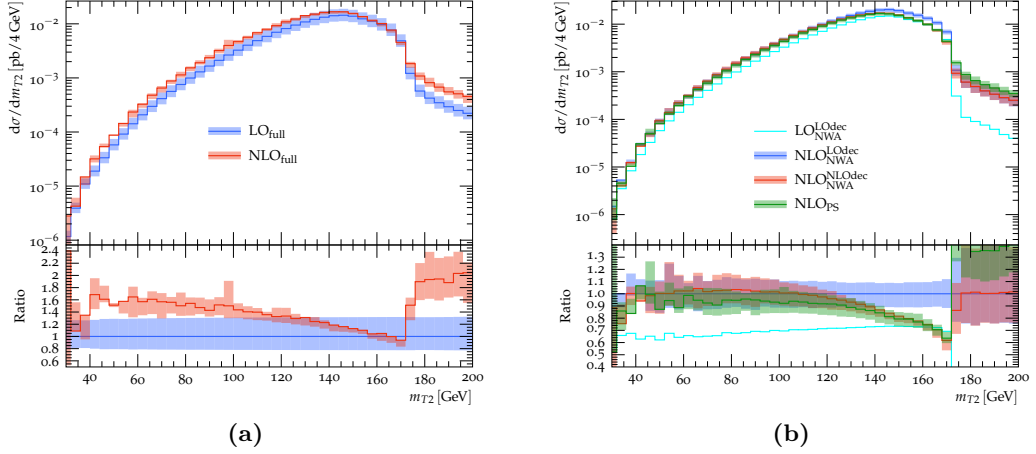


**Figure 7.7:** Results including scale variation bands for  $m_{T2}$ , for (a) the LO<sub>full</sub> and NLO<sub>full</sub> calculations, and (b) the calculations based on the NWA. The ratios are defined as in Fig. 7.6.

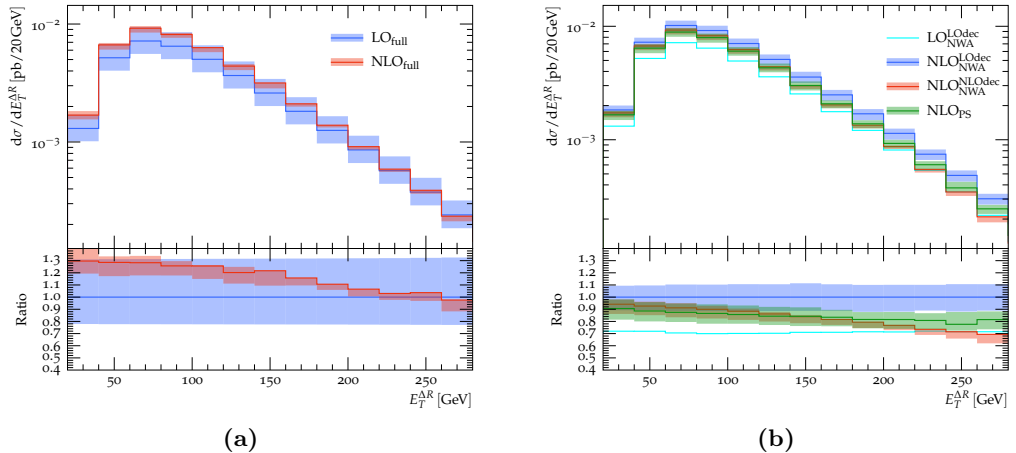


**Figure 7.8:** Results including scale variation bands for  $E_T^{\Delta R}$  for (a) the LO<sub>full</sub> and NLO<sub>full</sub> calculations, and (b) the calculations based on the NWA. The ratios are defined as in Fig. 7.6.

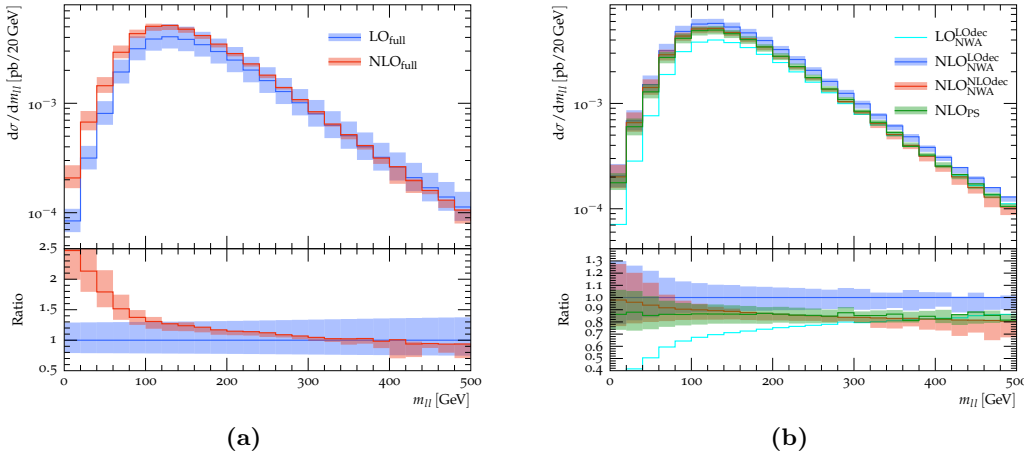


**Figure 7.9:** Results including scale variation bands for  $m_{ll}$ , for (a) the LO<sub>full</sub> and NLO<sub>full</sub> calculations, and (b) the calculations based on the NWA. The ratios are defined as in Fig. 7.6.

## 1463 7.4 Template fit results

After the qualitative discussion of differential results in the last Section, we now turn to the template fitting procedure and compare numerical values for the extracted top-quark mass from our different theoretical descriptions. To this effect, since we did not have data to compare to, we adapt the procedure outlined in Section 7.1 and apply the following approach to produce plots like the ones displayed in Fig. 7.10:

- **Simulation** : The distributions for  $m_{tb}$  and  $m_{T2}$  are produced at parton-level with the three input top-quark masses  $m_t^{\text{in}}$  for all theoretical descriptions.
  - **Template calibration:** The template distributions produced in the first step are individually fitted to the sum of a Gaussian and a Landau function. The theoretical description used as a basis for the distribution is called the calibration set. In the example of Fig. 7.10a, the calibration sets are described by the red/blue reference points in the legend.
  - **Pseudo-data:** From the different theoretical descriptions, a subset of events is drawn and labeled as *pseudo-data*. This sample corresponds to a luminosity of  $50 \text{ fb}^{-1}$ . In Fig. 7.10a, the theoretical description used for producing pseudo-data is given at the top of the plot. In general, the pseudo-data set is drawn from the more complete of the two predictions, which should be closer to real data. Pseudo-experiments are performed by repeating the random drawing of the pseudo-data 1000 times from the subset of all events, for a given theory prediction.
  - **$m_t$  extraction:** For each of the input top-quark masses  $m_t^{\text{in}}$ , an unbinned likelihood fit is applied to the pseudo-data, using the corresponding calibration set, to determine the extracted value of the top-quark mass  $m_t^{\text{out}}$ .

1486 The normalization of the histograms is chosen to reproduce the pseudo-data cross-  
 1487 section in the fit range, so that the result of template fits only depend on differences in  
 1488 the distribution shape. Looking again at Fig. 7.10a for reference, the red/blue points  
 1489 indicate the offset of the extracted top-quark mass with respect to the MC input mass  
 1490  $\Delta m_t^{\text{MC}} = m_t^{\text{out}} - m_t^{\text{in}}$ . When using the calibration function generated from the same  
 1491 theoretical prediction as used to produce the pseudo-data, the offset  $\Delta m_t$  should be close  
 1492 to zero and serves as a cross-check that no systematic bias exists in the fitting procedure.  
 1493 The error bars indicate the statistical uncertainty associated with the finite pseudo-data  
 1494 sample. The results from the three mass points are then fitted to a constant, and the  
 1495 numerical offset for  $\Delta m_t$  is given for each prediction in the legend, accompanied by its  
 1496 statistical uncertainty. Finally, the systematic uncertainty bands are provided by fitting  
 1497 the calibration set to the scale-varied pseudo-data.

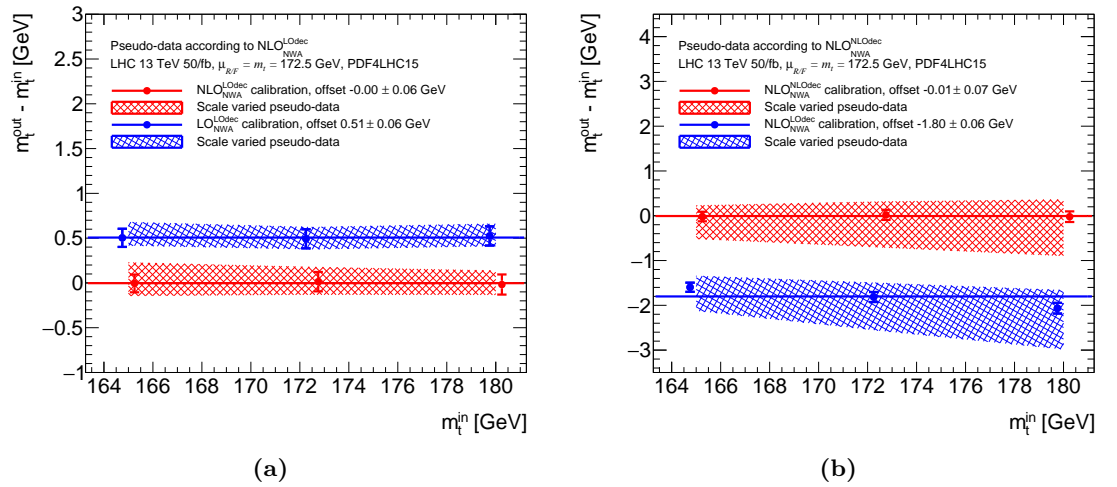
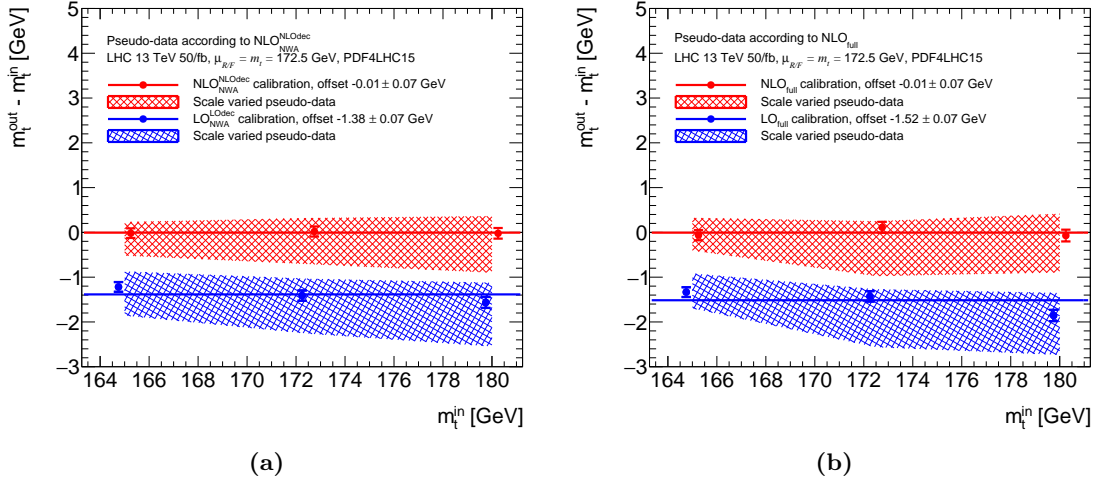


**Figure 7.10:** Pseudo-data is drawn according to (a)  $\text{NLO}_{\text{NWA}}^{\text{LOdec}}$  and (b)  $\text{NLO}_{\text{NWA}}^{\text{NLOdec}}$  for the three input top-quark masses, and the difference between the input mass and the template output is shown for each mass point. In each  $m_{t\bar{b}}$  subplot, the calibration set from the same prediction (red) is used to show the absence of systematic bias in the template fit. The calibration set from (a)  $\text{LO}_{\text{NWA}}^{\text{LOdec}}$  and (b)  $\text{NLO}_{\text{NWA}}^{\text{LOdec}}$  yields an offset (blue) in the top-quark mass extracted from the theoretically more complete respective pseudo-data of (a) 0.51 GeV and (b)  $-1.80$  GeV.

1498 Fig. 7.10a shows the offset between extracted and input top-quark masses when gen-  
 1499 erating pseudo-data according to the  $\text{NLO}_{\text{NWA}}^{\text{LOdec}}$  prediction, and using the calibration  
 1500 function fitted from  $\text{LO}_{\text{NWA}}^{\text{LOdec}}$  MC templates in blue. The offset in  $m_t$  produced by going  
 1501 from LO to NLO in  $t\bar{t}$  production amounts to 0.51 GeV. For comparison, Fig. 7.10b gives  
 1502 the offset from fitting the  $\text{NLO}_{\text{NWA}}^{\text{NLOdec}}$  pseudo-data with the  $\text{NLO}_{\text{NWA}}^{\text{LOdec}}$  calibration func-  
 1503 tion: higher-order corrections in the top-quark decay lead to a  $m_t$ -offset of  $-1.80$  GeV.  
 1504 Moreover, the NLO decay corrections in Fig. 7.10b lead to larger uncertainty bands, be-  
 1505 cause the scale variations produce non-uniform shape differences. These results already

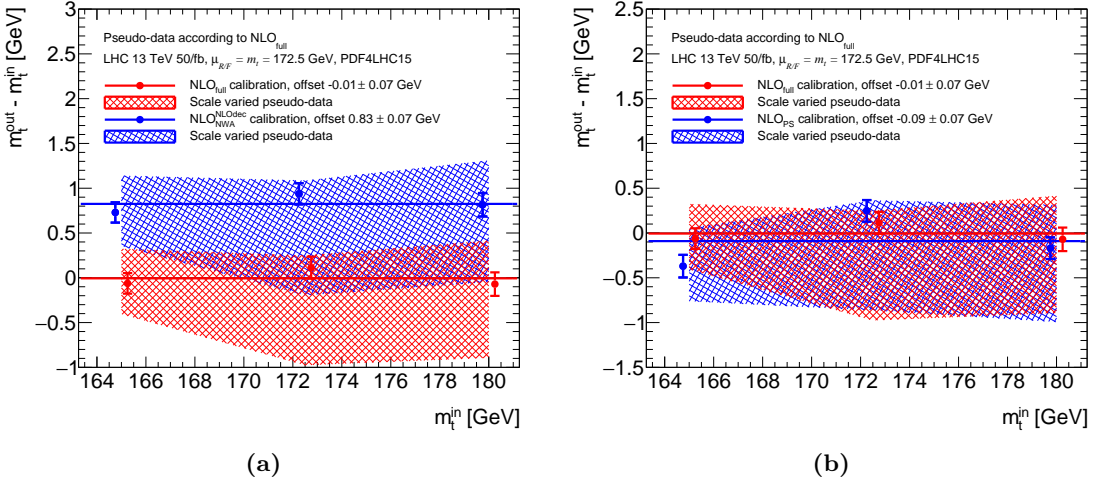
highlight the importance of higher-order corrections to the top-quark decay in a mass measurement based on  $m_{\ell b}$ .

Fig. 7.11 gives results for the extracted top-quark mass offsets when considering higher-order corrections in both production and decay, shown in Fig. 7.11a for the NWA case and in Fig. 7.11b for the full  $W^+W^-b\bar{b}$  case. The factorization of production and decay in the NWA approximation yields an offset of  $-1.38$  GeV, corresponding to the sum of the offsets in NLO production and decay shown in Fig. 7.10a, respectively Fig. 7.10b.



**Figure 7.11:** From fitting the  $m_{\ell b}$  distribution, the offset for the extracted top-quark mass based on (a)  $\text{NLO}_{\text{NWA}}^{\text{NLOdec}}$  and (b)  $\text{NLO}_{\text{full}}^{\text{NLOdec}}$  pseudo-data underlines the effect of taking NLO contributions for production and decay into account.

Finally, we consider the offsets in  $m_t$  produced when fitting the  $\text{NLO}_{\text{full}}^{\text{NLOdec}}$  pseudo-data set with the calibration from the  $\text{NLO}_{\text{NWA}}^{\text{NLOdec}}$  and the  $\text{NLO}_{\text{PS}}$  predictions in Fig. 7.12a, respectively Fig. 7.12b. While  $\text{NLO}_{\text{NWA}}^{\text{NLOdec}}$  still yields a sizeable offset of  $0.83$  GeV, the uncertainty bands now overlap. In the case of the  $\text{NLO}_{\text{PS}}$  calibration, the offset with respect to  $\text{NLO}_{\text{full}}^{\text{NLOdec}}$  pseudo-data is compatible with zero within statistical uncertainties. Although the  $\text{NLO}_{\text{PS}}$  prediction does not describe the top-quark decay at NLO accuracy beyond the soft limit, it still largely reproduces the full  $W^+W^-b\bar{b}$  description for the most part of the  $m_{\ell b}$  fit range, as can be seen in Fig. 7.3. Further studies were performed to understand if the discrepancy between  $\text{NLO}_{\text{NWA}}^{\text{NLOdec}}$  and  $\text{NLO}_{\text{PS}}$  originates in the parton-shower resummation. More details are given in Appendix A, where the parton-shower number of emissions in both the  $t\bar{t}$  production and decay is gradually restricted, and offsets in  $m_t$  are compared to the  $\text{NLO}_{\text{NWA}}^{\text{NLOdec}}$  prediction. Reducing the number of emissions to one in both production and decay showers moves the  $\text{NLO}_{\text{PS}}$  fitted  $m_t$ -value close to the  $\text{NLO}_{\text{NWA}}^{\text{NLOdec}}$  prediction. It is the general softening of  $m_{\ell b}$  around the kinematic edge, originating in the successive emissions from the parton-shower, that drives the top-quark mass fitted from the  $\text{NLO}_{\text{PS}}$  prediction towards the  $\text{NLO}_{\text{full}}$  value.



**Figure 7.12:** Top-quark mass offsets from  $m_{tb}$  for pseudo-data generated from the NLO<sub>full</sub> prediction are reduced when considering the case of (a) NLO<sub>NWA</sub><sup>NLOdec</sup> and (b) NLO<sub>PS</sub> calibration functions.

Similar results are also shown for the  $m_{T2}$  distribution in Appendix A. The numerical offsets for all comparisons are summarized in Table 7.1, together with a combined  $\chi^2$  computed from both  $m_{\ell b}$  and  $m_{T2}$  offsets for the same theoretical predictions. The value of  $\chi^2$  is defined as  $\chi^2 = (o_1 - o_2)^2 / (u_1^2 + u_2^2)$ , with  $i = 1, 2 = m_{\ell b}, m_{T2}$  and  $o_i \pm u_i$  are the corresponding offsets and their (uncorrelated) uncertainties. While almost all  $\chi^2$  values are consistent with zero, the comparison between NLO<sub>NWA</sub><sup>NLOdec</sup> and NLOPS differs significantly: the  $m_{T2}$  estimator for the top-quark mass is simply less sensitive to differences between the two latter predictions.

In conclusion, while NWA predictions are not disallowed, this study shows that higher-order corrections to the top-quark decays are at least as important as corrections to  $t\bar{t}$  production. The comparisons presented above suffer from a few shortcomings: in particular, further showering and hadronization effects, as well as detector efficiencies are expected to partly wash out the differences observed in the extracted top-quark mass. This is the subject of Chapter 9, which treats the topic in an even closer experimental setup with the help of a folding procedure in the ATLAS framework.

Pseudo-data	Calibration	Offset [GeV]		Figure		$\chi^2$
		$m_{\ell b}$	$m_{T2}$	$m_{\ell b}$	$m_{T2}$	
NLO <sub>NWA</sub> <sup>LOdec</sup>	LO <sub>NWA</sub> <sup>LOdec</sup>	+0.51 ± 0.06	+0.48 ± 0.04	7.10a	A.5a	0.17
NLO <sub>NWA</sub> <sup>NLOdec</sup>	NLO <sub>NWA</sub> <sup>LOdec</sup>	-1.80 ± 0.06	-1.67 ± 0.04	7.10b	A.5b	3.25
NLO <sub>NWA</sub> <sup>NLOdec</sup>	LO <sub>NWA</sub> <sup>LOdec</sup>	-1.38 ± 0.07	-1.24 ± 0.05	7.11a	A.5c	2.65
NLOfull	LOfull	-1.52 ± 0.07	-1.62 ± 0.05	7.11b	A.5d	1.35
NLOfull	NLO <sub>NWA</sub> <sup>NLOdec</sup>	+0.83 ± 0.07	+0.60 ± 0.06	7.12a	A.5e	6.22
NLOfull	NLO <sub>PS</sub>	-0.09 ± 0.07	-0.07 ± 0.06	7.12b	A.5f	0.05
NLO <sub>PS</sub>	NLO <sub>NWA</sub> <sup>LOdec</sup>	-0.92 ± 0.07	-1.17 ± 0.05	A.4a	A.5g	8.45
NLO <sub>PS</sub>	NLO <sub>NWA</sub> <sup>NLOdec</sup>	+0.96 ± 0.07	+0.68 ± 0.05	A.4b	A.5h	10.59
NLO <sub>PS</sub>	NLO <sub>PS</sub> ( $\mu_{tt}$ )	-0.03 ± 0.07	+0.02 ± 0.05	A.6b	A.6d	0.34

**Table 7.1:** The offsets from the top-quark mass extraction are given in GeV for pairs of the considered theoretical descriptions, from which the pseudo-data is generated, respectively the calibration function produced. The results are given for both the  $m_{\ell b}$  and  $m_{T2}$  distributions, along with the corresponding plot references (see also Appendix A). A  $\chi^2$  value is computed between offsets procured from fits of  $m_{\ell b}$  and  $m_{T2}$ .



# 8 Experimental resolution and bin migration

In the following Chapter, we reproduce the results outlined above with full particle-level predictions and compare the NLO<sub>full</sub> calculation to  $t\bar{t}$  results in the ATLAS Athena framework at detector-level. To study the extracted values of the top-quark mass from reconstructed events in a fast-simulation style, all distributions are folded from particle-level to detector-level in a custom implementation. We focus entirely on the dilepton channel in this Chapter, but the folding setup can be used in all decay channels.

## 8.1 Inverse problems

Usually, to compare experimentally measured cross-sections to a theoretical prediction, background contributions are first subtracted from data, and the corresponding signal distributions are unfolded to particle-level so that available measurements can be directly compared by theorists to their own predictions. The unfolding procedure is a particular example of so-called inverse problems: having a true distribution  $f(x)$  for some observable  $\Omega$ ,  $x \in [\Omega_{\min}, \Omega_{\max}]$ , the measured distribution  $g(y)$  is given by the Fredholm integral equation:

$$g(y) = \int_{\Omega_{\min}}^{\Omega_{\max}} K(x, y) f(x) dx , \quad (8.1)$$

where the kernel  $K(x, y)$  is a continuous function. For binned results, discretizing Eq. (8.1) gives a linear equation for  $\mathbf{x}$ ,  $\mathbf{y}$  the  $n$ -, respectively  $m$ -bin histograms corresponding to the true, respectively the measured distribution:

$$y_j = \sum_{i=1}^n A_{ij} x_i, \quad j \in \{1, \dots, m\} , \quad (8.2)$$

where  $\mathbf{A}$  is the bin migration matrix. The problem of inverting Eq. (8.2), that is to uncover the true distribution  $\mathbf{x}$  of an observable  $\Omega$  from the measured signal distribution  $\mathbf{y}$ , is the foundation of unfolding procedures. Because noise in the measured function can lead to instabilities in the inversion of the response matrix  $\mathbf{A}$ , the procedure has to be regularized. There are two distinct unfolding methods: direct unfolding procedures, which usually implement some regularization parameter for a smooth inversion of Eq. (8.2), and iterative methods. For a short review of unfolding methods in particle physics, see Ref. [203].

Conversely, instead of unfolding the data to particle-level, the chosen strategy for the 13 TeV ATLAS top-quark mass analysis in both lepton+jets and dilepton channels is to produce the distribution templates and perform the likelihood fit only at detector-level, for several reasons. In particular, the top-quark mass extraction in the lepton+jets channel suffers mostly from jet and  $b$ -jet energy scale uncertainties (see Section 5.2.5.1). To try and reduce the latter, the lepton+jets analysis contains a 3D-fit where the template parametrization depends on the top-quark mass  $m_t$  and both the jet and  $b$ -jet energy scale factors (JSF and  $b$ -JSF). All three parameters are then simultaneously measured from a fit to data. It is therefore simpler to simulate all samples up to detector-level, and directly perform the fit of all three parameters without having to handle a 3D-unfolding. This procedure also avoids numerical instabilities inherent to the chosen unfolding algorithm. The main disadvantage of the direct method lies in the computing time: indeed, all MC samples ( $m_t$ -varied central predictions, systematics-varied samples, and background) have to be simulated up to detector-level. Instead, we propose as a complementary alternative the use of direct folding, as in Eq. (8.2), to provide distributions at detector-level from the samples generated at particle-level. Thus, the costly ATLAS simulation is avoided and one can quickly quantify effects of systematic uncertainties on e.g. the extracted top-quark mass.

## 8.2 Folding setup in ATLAS

Considering the results of Chapter 7, our goal is to use the folding setup in ATLAS to estimate the uncertainty in using the incomplete  $t\bar{t}$  prediction instead of a full parton-showered  $W^+W^-b\bar{b}$  event set. It is clear that simulating all MC samples from particle-to detector-level is time-consuming: with one theoretical central prediction (for example POWHEG + Pythia8) and one parameter for the template fit (e.g. the top-quark mass  $m_t$ ), one has to produce and simulate as many samples as top-quark mass points.

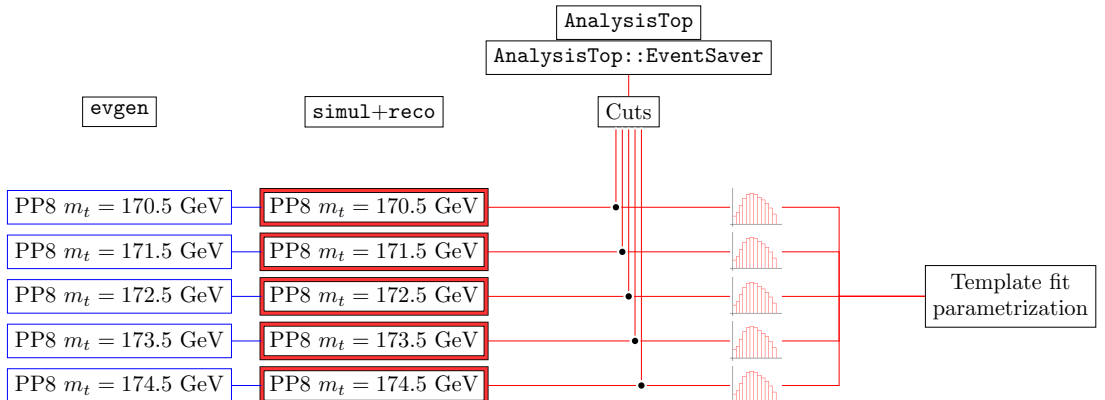


**Figure 8.1:** The workflow for a template fit of the central prediction POWHEG+Pythia8 (PP8) and five top-quark mass points.

Fig. 8.1 illustrates the current analysis workflow for five top-quark mass points. Each of the samples is produced at particle-level first (`evgen` in blue on the far left) and has to be simulated (`simul+reco` in red). In the ATLAS 13 TeV analysis, all samples entering the template fit parametrization are fast-simulated with the ATLFAST package. The analysis is run, and distributions are produced for the individual top-mass samples. A custom event saver from the `AnalysisTop` package applies the cuts outlined in Section 8.4 and saves histograms for control purposes, as well as the final observables entering the top-quark mass fit: for the dilepton case, we are only interested in the  $m_{\ell b}$  distribution in this respect. Histograms of the  $m_{\ell b}$  distribution for all individual mass points are then fed to the template parametrization.

To estimate systematic uncertainties, MC variation samples currently go through the same routine. For example, MC samples with variations of radiative parameters (for example `hdamp` in PowHeg, or `Pythia8` versus `Herwig7` for the shower-algorithm) are also simulated and template-parametrized, and the result of the template fit is taken as a systematic uncertainty on the central sample for the extracted top-quark mass. For a swifter evaluation of the associated systematics, we directly fold histograms of variation samples (e.g. `hdamp_var` and `shower_var`, or  $W^+W^-b\bar{b}$ ) from particle- to detector-level, and use the output in the template fit for an estimate of the systematic uncertainty on the extracted top-quark mass.

We will use a simple version of Eq. (8.2), where pure bin migration is implemented by a right stochastic matrix  $\mathbf{A}$ , and the detector efficiencies are represented by two bin-by-bin probability vectors  $\epsilon^{\text{eff}}$  and  $f^{\text{acc}}$ :

$$\mathcal{R}_i = \frac{1}{f_i^{\text{acc}}} A_{ij} \times \left( \mathcal{P}_j \epsilon_j^{\text{eff}} \right) , \quad (8.3)$$

where  $\mathcal{R}_i$  is the number of events at detector-level in bin  $i$  (for an arbitrary differential distribution), and  $\mathcal{P}_j$  is the number of events at particle-level in bin  $j$ . The migration matrix  $A_{ij}$  is the probability for an event in bin  $j$  at particle-level to move to bin  $i$  at detector-level, provided the event is reconstructed. Finally, the efficiency  $\epsilon_j^{\text{eff}}$  is the probability for an event in bin  $j$  at particle-level to be reconstructed in the detector, and  $f_i^{\text{acc}}$  the probability of an event in bin  $i$  at detector-level to stem from a fake signal (i.e. it has no existing counterpart at particle-level). The migration matrices and detector efficiencies only encode the experimental resolution simulated by GEANT4 [146] (or by the ATLFAST [147] parametrization).

This alternative procedure is depicted in Fig. 8.2. The central PowHeg+Pythia8 (PP8) sample is simulated once: histograms at both detector-level (in red) and particle-level (in blue) are fed to the custom folding package (green nodes). The `build.py` script produces the migration matrices and detector efficiencies defined above. In principle, for a given top-quark mass, pure theoretical uncertainties can then be estimated by applying the migration matrices and efficiencies from the central- to variation samples, since detector effects do not depend on the MC theory variations themselves. The `upfold.py` script implements Eq. (8.3) and generates folded detector-level histograms from the particle-level of MC-varied samples, and writes them out for future use in the template fit. More over, consistency and statistical cross-checks are performed by

1637 a `tests.py` script. Now, in addition to the usual systematic variations, we want to  
 1638 estimate the uncertainty stemming from the non-resonant and non-factorizing diagrams  
 1639 in the full  $W^+W^-b\bar{b}$  calculation.

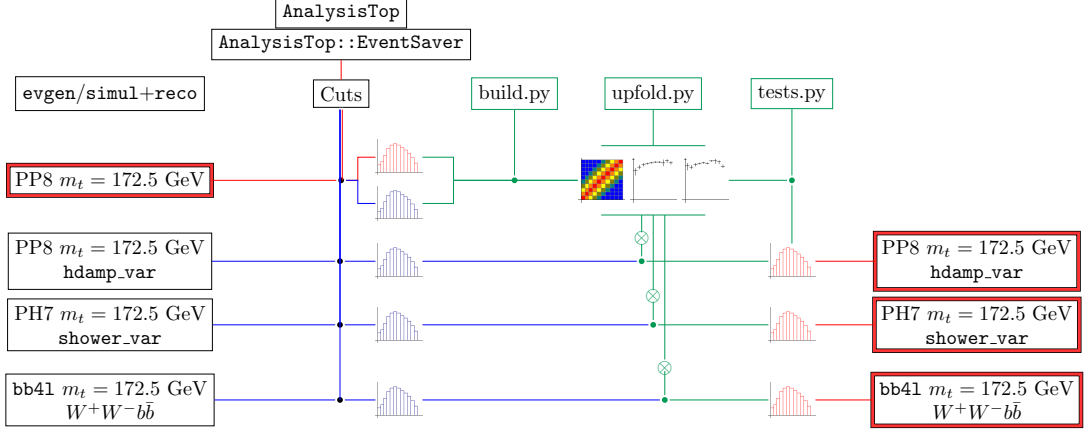


**Figure 8.2:** The folding package builds migration matrices and efficiency histograms from the simulated detector- and the particle-level of a central sample, for example POWHEG + Pythia8 with  $m_t = 172.5$  GeV. They are used to fold particle-level histograms from MC-varied samples to detector-level.

### 1640 8.3 Theoretical descriptions and MC samples

1641 The MC derivation samples (DxAOD) used for all subsequent studies were produced offi-  
 1642 cially by ATLAS during the MC16a campaign (that is, they should describe the 2015/2016  
 1643 data) and are summarized in Table 8.1. The nominal samples for NLO  $t\bar{t}$  in the NWA  
 1644 are generated by POWHEG (for the matrix-element) and parton-showered with Pythia8  
 1645 for four different mass points.<sup>1</sup> These samples are simulated to detector-level with the  
 1646 ATLFast algorithm, but a cross-check is done with respect to the full GEANT4 simula-  
 1647 tion for one mass point. To be able to have a fairer comparison of the full  $W^+W^-b\bar{b}$   
 1648 prediction to the  $t\bar{t}$  NWA description, the single-top  $Wt$  channel is added to the  $t\bar{t}$   
 1649 sample. Finally, in order to generate  $W^+W^-b\bar{b}$  predictions at particle-level, we use the  
 1650 following setup:

- 1651 • **Parton-level production:** The full dilepton final-state  $(e^+\nu_e)(\mu^-\bar{\nu}_\mu)b\bar{b}$  is gen-  
 1652 erated by SHERPA v2.2.6 at NLO in production with a setup similar to the one  
 1653 presented in Chapter 6. The generated events are recomputed with the ATLAS  
 1654 top-quark mass points, and the  $p_T^{lb}$  cut introduced in our former analysis is removed.  
 1655 As an alternative, we produce events at parton-level with a local installation of the  
 1656 bb4l generator in Powheg-Box-RES. The latter events are generated outside

<sup>1</sup>Samples with nine top-quark mass points were officially produced, but we use the same mass points as for  $W^+W^-b\bar{b}$ .

### 8.3 Theoretical descriptions and MC samples

Sample DSID	Generator (ME + PS/Had)	$m_t$ [GeV]	Simulation tags
<b>NLO <math>t\bar{t}</math> (NWA)</b>			
411053	POWHEG+Pythia8	171	e6696_a875_r9364_p3629
411054	POWHEG+Pythia8	172	e6696_a875_r9364_p3629
411057	POWHEG+Pythia8	173	e6696_a875_r9364_p3629
411058	POWHEG+Pythia8	174	e6696_a875_r9364_p3629
<b>NLO <math>W^+W^-b\bar{b}</math></b>			
999991	bb4l+Herwig7	171	—
999992	bb4l+Herwig7	172	—
999993	bb4l+Herwig7	173	—
999994	bb4l+Herwig7	174	—
<b>NLO single-top <math>W^-t</math> (DR)</b>			
411109	POWHEG+Pythia8	171	e6852_a875_r9364_p3629
411111	POWHEG+Pythia8	172	e6852_a875_r9364_p3629
411117	POWHEG+Pythia8	173	e6852_a875_r9364_p3629
411119	POWHEG+Pythia8	174	e6852_a875_r9364_p3629
<b>NLO single-top <math>W^+\bar{t}</math> (DR)</b>			
411110	POWHEG+Pythia8	171	e6852_a875_r9364_p3629
411112	POWHEG+Pythia8	172	e6852_a875_r9364_p3629
411118	POWHEG+Pythia8	173	e6852_a875_r9364_p3629
411120	POWHEG+Pythia8	174	e6852_a875_r9364_p3629
<b><math>t\bar{t}</math> variation samples</b>			
410472	POWHEG+Pythia8	172.5	e6348_a875_r9364_p3629
410472	POWHEG+Pythia8	172.5	e6348_s3126_r9364_p3629
410558	POWHEG+Herwig7.0.4	172.5	e6366_a875_r9364_p3629

**Table 8.1:** Summary of the MC derivations used as input to the top-quark mass analysis.

of **Athena** since the implementation of the **bb4l** program has not been validated yet.

- **Particle-level production:** Because the SHERPA CSS parton-shower does not contain the necessary  $g \rightarrow b\bar{b}$  dipoles to produce the desired endstate, we write out LHE files and run the **Herwig7.1.3** angular-ordered parton-shower (with hadronization included sequentially) later on in the **Athena** framework. These LHE files are generated separately for the Born and virtual part (BVI), respectively for the real-subtracted emissions (RS), and added together in an intermediate step. Finally, because SHERPA does not write out any color flow information in the intermediate LHE output files, we select one color flow configuration for each of the subprocesses. This arbitrary choice does not make any difference for the parton-showered kinematic distributions considered in the template fit (the

## 8 Experimental resolution and bin migration

exact configurations and comparisons between variations of them are shown in Appendix B). The same parton-shower is applied in `Athena` to the parton-level events produced with `bb41`.

- **Analysis pre-step:** The `Athena` MC simulation step produces a so-called event (EVNT) file containing the particle information and kinematics. To be able to run the `AnalysisTop` routine on the sample, one needs to transform it to a DAOD derivation format. The truth information is propagated to the derivation-level by running the `Reco_tf.py` script in `Athena` with `Truth1` level, which means the derivation output basically contains thinned MC truth information.

For first studies, we only generate predictions for four mass points, both for the  $t\bar{t}$  NWA and the  $W^+W^-b\bar{b}$  prediction (as well as for single-top  $Wt$  samples):

$$m_t \in \{171, 172, 173, 174\} [\text{GeV}] . \quad (8.4)$$

### 8.4 The AnalysisTop setup

In the `Athena` framework, the `AnalysisTop` package contains all the ingredients that are useful for general top-quark measurements. It is regularly updated with respect to latest calibration methods and numerical results, and serves as an interface between detector quantities and the final derivations. In our case, except when explicitly stated otherwise, the version used is `AnalysisTop 21.2.61`. Within the latter, we use some slightly modified version of the `TopMass_13TeV_FrMu` ATLAS analysis at 13 TeV. As mentioned earlier, the code executes both lepton+jets and dilepton routines simultaneously.

The `AnalysisTop` package is run with the `top-xaod` command, which takes a list of derivations and a cuts file as input. The various MC samples were presented above. As for the cuts, we require:

- Two oppositely charged leptons with exactly one electron and one muon which fulfill  $p_T^\ell > 28 \text{ GeV}$ . For reconstructed events, the lepton criteria for passing the trigger requirements are taken from the Top Trigger Group recommendation. These depend on the luminosity and are different for 2015 and 2016 data. They are set to:

```
1696   HLT_e24_lhmedium_L1EM20VH HLT_e60_lhmedium HLT_e120_lhloose
1697   HLT_mu20_iloose_L1MU15 HLT_mu50
```

for the 2015 data, respectively for the 2016 data:

```
1699   HLT_e26_lhtight_nod0_ivarloose HLT_e60_lhmedium_nod0
1700   HLT_e140_lhloose_nod0 HLT_mu26_ivarmedium HLT_mu50 .
```

- $H_T = \sum_i p_{T,i} > 120 \text{ GeV}$  with  $H_T$  the event's total transverse momentum.
- $n_{\text{jets}} \geq 2$  for the total number of jets with  $p_T^{\text{jet}} > 25 \text{ GeV}$ .

#### 8.4 The *AnalysisTop* setup

- 1703 •  $n_{b,\text{jets}} = 2$ : exactly two  $b$ -jets with  $p_T^{\text{jet}} > 25 \text{ GeV}$ . For reconstructed events, a 70%  
1704  $b$ -tagging working point is chosen for the MV2c10 [204, 205]  $b$ -tagging algorithm.  
1705 We define a  $b$ -jet within particle-level events using the JET\_N\_GHOST criterion in  
1706 **AnalysisTop**, for which a jet is  $b$ -tagged if it contains a  $B$ -hadron.
- 1707 •  $m_{\ell\ell} > 15 \text{ GeV}$  for the invariant mass of the two-lepton system.



## **9 Determination of the top-quark mass at detector-level**

The simulated  $t\bar{t}$  NWA predictions are compared at particle- and detector-level for control- and for the  $m_{\ell b}$  distributions, and migration matrices and detector efficiencies derived from those samples are plotted. After some simple cross-checks of the setup, the  $W^+W^-b\bar{b}$  folded results and template parametrization are presented, along with numerical comparisons of both theoretical descriptions for the extraction of the top-quark mass.

### **9.1 Differential results at particle- and detector-level**

(a)  $t\bar{t}$  (b)  $t\bar{t}$   
particle detector-  
level level

**Figure 9.1**

(a)  $t\bar{t}$  (b)  $W^+W^-b\bar{b}$

**Figure 9.2**

(a)  $W^+W^-b\bar{b}$  (b)  $W^+W^-b\bar{b}$   
particle detector-  
level level

**Figure 9.3**

### **9.2 Statistical and systematic cross-checks**

*9 Determination of the top-quark mass at detector-level*

<sub>1718</sub> [2]

<sub>1719</sub> **9.3 Folded results and template parametrization**

<sub>1720</sub> [2]

<sub>1721</sub> **9.4 Numerical result for top-quark mass uncertainties**



1722

## Part III

1723

# Top-Quark Mass Effects in Higgs Pair Production

1724



# 1725 10 Top-mass dependence in Higgs pair 1726 production at NLO

1727 The top-quark mass also has substantial effects in the Higgs sector. After the discovery  
 1728 of the Higgs boson by both ATLAS [206] and CMS [207] experiments in 2012, which was  
 1729 the crowning completion of one of LHC’s foremost goals, the experimental community  
 1730 set to measure its properties to further test if it was compatible with the SM predicted  
 1731 Higgs boson. As of today, some of the Higgs boson properties are very well-measured (as  
 1732 for the example of its mass, spin, or couplings to heavier fermions and gauge bosons).  
 1733 Still, because of lower branching ratios and irreducible backgrounds, the measurement  
 1734 of the Higgs boson couplings to light fermions, as well as the Higgs self-coupling, is still  
 1735 accompanied by large uncertainties of the order of  $\mathcal{O}(10 - 20\%)$ . This leaves room for  
 1736 New Physics to appear. The latest ATLAS constraint on the Higgs boson self-coupling,  
 1737 in ratio to its predicted value from the SM  $c_{hhh} = \lambda/\lambda_{\text{SM}}$ , is  $-5.0 \leq c_{hhh} \leq 12.1$  [16]  
 1738 at 95% confidence level (CL), from a combination of three searches for the  $hh$  final-  
 1739 states  $b\bar{b}b\bar{b}$ ,  $b\bar{b}\tau^+\tau^-$  and  $b\bar{b}\gamma\gamma$ . These limits assume the other Higgs couplings to be SM-  
 1740 like. In the future, with the accumulation of statistics at high-luminosity (HL)-LHC,  
 1741 the experimental bounds are expected to improve, and the measurement of differential  
 1742 distributions (with a small number of total events) is even conceivable. In the rest of  
 1743 this Chapter, we review the theoretical standpoint of  $hh$  production, and show how New  
 1744 Physics can strongly affect this process in the framework of a non-linear EFT.

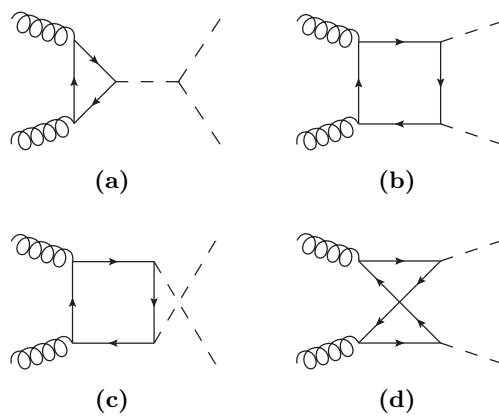


**Figure 10.1:** (a-d) LO Feynman diagrams for  $hh$  production by gluon-fusion.

## 10.1 Theoretical descriptions of $hh$ production

At the LHC, Higgs bosons (and in particular Higgs boson pairs, which we consider in the next Chapters) are produced mainly via a top-quark loop. Fig. 10.1 displays the LO Feynman diagrams for di-Higgs production in gluon-fusion: diagrams that contain the Higgs self-coupling  $\lambda$  are called *triangle-like* (as in Fig. 10.1a), and diagrams that do not *box-like* (as in Figs 10.1b–10.1d).<sup>1</sup> Because  $gg \rightarrow hh$  production is loop-induced, NLO corrections start at two-loop order already and pose a challenge to compute. The matrix-element for  $g(p_1, \mu, a) + g(p_2, \nu, b) \rightarrow h(p_3) + h(p_4)$  production decomposes into two form factors (with  $p_i$  the 4-momenta, Greek letters for the Lorentz indices and roman letters for the color indices):

$$\mathcal{M}_{ab}^{\mu\nu} = \frac{\alpha_s}{8\pi v^2} \delta_{ab} \epsilon_\mu \epsilon_\nu (F_1(\hat{s}, \hat{t}, m_h^2, m_t^2, d) T_1^{\mu\nu} + F_2(\hat{s}, \hat{t}, m_h^2, m_t^2, d) T_2^{\mu\nu}), \quad (10.1)$$

where the Lorentz structure is contained in the tensors  $T_1$ ,  $T_2$  and the functions  $F_1$ ,  $F_2$  depend on four physical scales altogether (two kinematic invariants and both particle mass scales, as well as on the analytically-continued dimension  $d$ ). Finally, the first form factor can be further split into a contribution stemming only from triangle-like diagrams, respectively only box-like diagrams:

$$F_1 = F_\Delta + F_\square, \quad (10.2)$$

and the box diagrams contribute to both  $F_\square$  and  $F_2$ . Historically, the LO one-loop total cross-section has been known analytically for a long time [208], and the triangular form factor given in Eq. (10.2), for  $\tau = 4m_t^2/\hat{s}$ , takes the form

$$F_\Delta = \frac{6m_h^2 \lambda \hat{s}}{\hat{s} - m_h^2} \tau (1 + (1 - \tau)f(\tau)), \quad (10.3)$$

$$f(\tau) := \begin{cases} \arcsin^2(\frac{1}{\sqrt{\tau}}) & \tau \geq 1 \\ -\frac{1}{4} \left( \log\left(\frac{1+\sqrt{1-\tau}}{1-\sqrt{1-\tau}}\right) - i\pi \right)^2 & \tau < 1. \end{cases}$$

The triangle diagrams can be reduced to single Higgs production and subsequent attachment of the triple Higgs vertex, where all the NLO integrals (massive two-loop up to three-point) have been computed with the full top-mass dependence [209–211]. The two-loop massive four-point integrals to  $gg \rightarrow hh$  are known analytically only partly [212–214]. Some computations exist with expansions in given kinematic limits (large top-quark mass [212], top-quark threshold [215], small Higgs transverse momentum [216], and high-energy expansion [217, 218]). We consider in the following only the heavy-top limit  $m_t \rightarrow \infty$ , without any expansion in  $1/m_t^{2n}$ , as well as several approximations that include part of the full-theory result at NLO QCD.

---

<sup>1</sup>At two-loop level, some diagrams do not contain the coupling  $\lambda$  but have triangular topologies, see e.g. the last diagram in Fig. 10.4.

1772 **10.1.1 Approximations in the heavy-top limit ( $m_t \rightarrow \infty$ )**

1773 To circumvent the direct computation of the difficult NLO QCD corrections to  $gg \rightarrow hh$ ,  
 1774 one neat approach that was applied successfully in Higgs production (as well as in a  
 1775 whole collection of other processes) is to collapse one top-quark loop to an effective  
 1776 coupling between gluons and Higgs bosons within a so-called Effective Field Theory  
 1777 (EFT). This is the so-called heavy-top limit (HTL). EFTs are usually employed to  
 1778 describe physics entering at a higher-scale than the typical scales of the process at  
 1779 hand. In an agnostic approach, one assumes nothing about new particles whatsoever and  
 1780 instead computes effective couplings between known particles, that are only indirectly  
 1781 affected by more massive particles. Their exact degrees of freedom are thus integrated  
 1782 out of the calculation. This was for example the basic framework of the Fermi theory  
 1783 before  $W$  and  $Z$  bosons were discovered, where one assumes a 4-particle interaction  
 1784 vertex between fermions coupling with strength  $G_F$ . In the case of di-Higgs production,  
 1785 the top-quark degrees of freedom are integrated out and an effective coupling between  
 1786 gluons and Higgs bosons is introduced. There exist different consistent formulations  
 1787 of a theory with effective coupling vertices between gluons and Higgs bosons: usually,  
 1788 one introduces higher-dimension contact operators into the SM Lagrangian, with an  
 1789 EFT expansion in the New Physics scale  $1/\Lambda$ .<sup>2</sup> An alternative EFT formulation will be  
 1790 introduced in Section 10.2.

1791 In the next Sections, comparisons are shown between predictions for the full theory  
 1792 at QCD NLO and various approximations based on the heavy-top limit for variations of  
 1793 the Higgs couplings.<sup>3</sup> In order of increasing accuracy, these are:

- 1794 • **Pure HTL:** all top-quark loops are shrunk to an effective vertex between gluons  
 1795 and Higgs bosons. At LO, the form factors given in Eqs. (10.1), (10.3), for  $\tau \rightarrow \infty$ ,  
 1796 reduce to

$$F_{\Delta} \rightarrow \frac{3m_h^2 \lambda}{\hat{s} - m_h^2} \left( \frac{4}{3} \hat{s} \right) , \quad (10.5)$$

$$F_{\square} \rightarrow -\frac{4}{3} \hat{s} , \quad (10.6)$$

$$F_2 \rightarrow 0 . \quad (10.7)$$

1797 At NLO, they are at most given by one-loop diagrams.

- 1798 • **Born-improved HTL:** the virtual and real contributions are calculated within  
 1799 HTL, but reweighted on an event-by-event basis with the ratio of the full-theory  
 1800 Born to the HTL Born contribution,

---

<sup>2</sup>Mostly, nowadays, analyses consider only dimension-6 operators, because the only dimension-5 operator violates lepton number conservation.

<sup>3</sup>In the SM case, there are already important differences between the considered approximations [219].

$$\mathrm{d}\sigma_{V,R}^{\mathrm{B.-i.}} = \mathrm{d}\sigma_{V,R}^{\mathrm{HTL}} \frac{\mathrm{d}\sigma_B^{\mathrm{FT}}}{\mathrm{d}\sigma_B^{\mathrm{HTL}}} . \quad (10.8)$$

- 1801 • **FT<sub>approx</sub>** : the same prescription as given in Eq. (10.8) is applied for the virtual  
 1802 contribution, but the real-emission matrix-element is computed in the full theory  
 1803 (these are at most one-loop diagrams).
- 1804 • **Full theory:** the full two-loop virtual contribution is computed numerically.

### 1805 10.1.2 Two-loop contribution in the SM

1806 The first full computation of NLO QCD corrections to  $gg \rightarrow hh$  production in the SM  
 1807 was presented in Ref. [219]. All BSM results shown in Sections 10.3 and 11.2 are based  
 1808 on two-loop amplitudes calculated numerically for the SM.

1809 As a brief description of the calculation, the two-loop contribution to the SM amplitude  
 1810 was generated by an extended version of GoSAM called GoSAM-2LOOP. The reduction  
 1811 to master integrals was operated with REDUZE 2 [220], and the integral evaluation per-  
 1812 formed with the help of sector decomposition in SECDEC 3 [221–223]. In particular,  
 1813 the integration itself was implemented within a rank-one lattice quasi-Monte-Carlo rule  
 1814 (QMC) that is described in more detail in Ref. [224]. The Higgs and the top-quark mass  
 1815 are fixed, so that the integrals depend only on the two kinematic invariants  $\hat{s}$  and  $\hat{t}$ .<sup>4</sup>

1816 Examples of the SM two-loop Feynman diagrams are given in the first, third and last  
 1817 rows of Fig. 10.4. The amplitude was calculated for a pre-sampled set of 5372 phase-  
 1818 space points in  $(\hat{s}, \hat{t})$  at 14 TeV and 1343 points at 100 TeV, which are rescaled for  
 1819 non-SM values of the Higgs couplings (see Section 10.2). IR subtraction was performed  
 1820 within the CS dipole formalism, where for the  $gg$  channel, the insertion operator **I** is  
 1821 given by

$$\mathbf{I}_{gg} = \frac{\alpha_s}{2\pi} \frac{(4\pi)^\epsilon}{\Gamma(1-\epsilon)} \left( \frac{\mu_R^2}{2p_1 \cdot p_2} \right)^\epsilon \cdot 2 \left( \frac{C_A}{\epsilon^2} + \frac{\beta_0}{2\epsilon} - C_A \frac{\pi^2}{3} + \frac{\beta_0}{2} + K_g \right) , \quad (10.9)$$

1822 with  $\beta_0 = \frac{11}{6}C_A - \frac{2}{3}T_R N_f$  and  $K_g = \left( \frac{67}{18} - \frac{\pi^2}{6} \right) C_A - \frac{10}{9}T_R N_f$ . As a side note, the IR  
 1823 singular pattern is the same between the SM and the BSM case presented below. When  
 1824 inserting the CS operator into the Born term, see Eq. (4.8), the poles from the virtual  
 1825 contribution should cancel. To get the correct finite terms, thus, the Born has to be  
 1826 expanded up to  $\mathcal{O}(\epsilon^2)$ . The explicit cancellation of poles in  $\epsilon$  is checked numerically.

## 1827 10.2 The Electroweak Chiral Lagrangian

1828 Since we are interested in variations of the Higgs couplings, we consider the case of one  
 1829 particular extension of the SM called the Electroweak Chiral Lagrangian (EWChL) [226,

---

<sup>4</sup>The top-quark mass is renormalized on-shell. Dependence of the numerical results on the top-mass scheme are investigated in Ref. [225].

227]. The latter framework is a non-linear realization of an EFT which will be described  
 1830 in some detail below. The EWChL, to leading-order, is given as  
 1831

$$\begin{aligned} \mathcal{L}_2 = & -\frac{1}{2}\langle G_{\mu\nu}G^{\mu\nu}\rangle - \frac{1}{2}\langle W_{\mu\nu}W^{\mu\nu}\rangle - \frac{1}{4}B_{\mu\nu}B^{\mu\nu} + \sum_{\psi=q_L,l_L,u_R,d_R,e_R} \bar{\psi}iD\psi \\ & + \frac{v^2}{4} \langle D_\mu U^\dagger D^\mu U \rangle (1 + F_U(h)) + \frac{1}{2}\partial_\mu h \partial^\mu h - V(h) \\ & - v \left[ \bar{q}_L \left( Y_u + \sum_{n=1}^{\infty} Y_u^{(n)} \left( \frac{h}{v} \right)^n \right) UP_+ q_R + \bar{q}_L \left( Y_d + \sum_{n=1}^{\infty} Y_d^{(n)} \left( \frac{h}{v} \right)^n \right) UP_- q_R \right. \\ & \left. + \bar{l}_L \left( Y_e + \sum_{n=1}^{\infty} Y_e^{(n)} \left( \frac{h}{v} \right)^n \right) UP_- l_R + \text{h.c.} \right], \end{aligned} \quad (10.10)$$

1832 where  $U = \exp(2i\phi^a T^a/v)$  is the Goldstone matrix and contains the electroweak  
 1833 Goldstone fields  $\phi^a$ , and  $T^a$  are the generators of  $SU(2)_L$ . Here,  $P_\pm = 1/2 \pm T_3$  are the  
 1834 chiral projection operators, and the Higgs sector is characterized by an order-by-order  
 1835 expansion in the Higgs EW singlet  $h$ , given by the functions

$$F_U(h) = \sum_{n=1}^{\infty} f_{U,n} \left( \frac{h}{v} \right)^n, \quad V(h) = v^4 \sum_{n=2}^{\infty} f_{V,n} \left( \frac{h}{v} \right)^n. \quad (10.11)$$

1836 The coefficients  $f_{U,n}$ ,  $V_{U,n}$  and  $Y_{u,d,e}^{(n)}$  are in principle free parameters and can be of  
 1837  $\mathcal{O}(1)$ . The SM case is retrieved when

$$f_{U,1} = 2, \quad f_{U,2} = 1, \quad f_{V,2} = f_{V,3} = \frac{m_h^2}{2v^2}, \quad f_{V,4} = \frac{m_h^2}{8v^2}, \quad Y_f^{(1)} = Y_f. \quad (10.12)$$

1838 Now, this Lagrangian is structured not in terms of canonical dimensions for the quan-  
 1839 tum fields and couplings, but rather in terms of *chiral* dimensions (as in the case of the  
 1840 chiral EFT of pions in QCD). The chiral dimension assigned to fields, derivatives and  
 1841 couplings are

$$d_\chi(A_\mu, \varphi, h) = 0, \quad d_\chi(\partial, \bar{\psi}\psi, g, y) = 1, \quad (10.13)$$

1842 with  $A_\mu$  being any gauge field,  $g$  representing any of the SM gauge couplings, and  $y$   
 1843 any weak coupling (like the Yukawa couplings). The ordering in the chiral dimension  $d_\chi$   
 1844 is equivalent to counting the number of loops  $L$ ,  $d_\chi = 2L + 2$ . In summary, the NLO  
 1845 (in  $\alpha_s$ ) QCD corrections to  $hh$  production stem from one-loop diagrams in the leading  
 1846 (in  $d_\chi$ ) EWChL  $\mathcal{L}_2$  and from tree diagrams in the next-to leading part  $\mathcal{L}_4$ . All of these  
 1847 contributions are of chiral dimension  $d_\chi = 4$ . Then, the effective Lagrangian reduces to

$$\mathcal{L} \supset \underbrace{-m_t \left( c_t \frac{h}{v} + c_{tt} \frac{h^2}{v^2} \right) \bar{t}t}_{\mathcal{L}_2} - c_{hhh} \frac{m_h^2}{2v} h^3 + \underbrace{\frac{\alpha_s}{8\pi} \left( c_{ggh} \frac{h}{v} + c_{gggh} \frac{h^2}{v^2} \right) G_{\mu\nu}^a G^{a,\mu\nu}}_{\mathcal{L}_4}. \quad (10.14)$$

1848 The EWChL introduces five anomalous couplings to the SM and the corresponding  
1849 LO Feynman diagrams are given in Fig. 10.2.

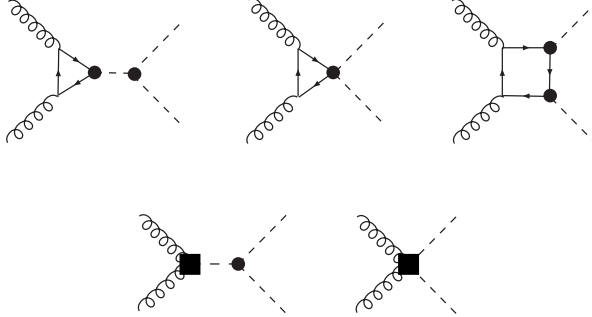


**Figure 10.2:** LO diagrams for the various terms from the EWChL Lagrangian. Both vertices from  $\mathcal{L}_2$  (black dots) and local contact terms from  $\mathcal{L}_4$  (black squares) contribute.

1850 Diagrams that are of higher chiral dimension (or do not belong to  $\mathcal{O}(\alpha_s^4 \alpha^2)$ ) are sys-  
1851 tematically neglected, like the ones given in Fig. 10.3. The full virtual amplitude is then  
1852 given by two-loop contributions (Fig. 10.4), one-loop diagrams that contain one effective  
1853 coupling from  $\mathcal{L}_4$  (Fig. 10.5), and one tree-diagram containing exactly two effective  
1854 vertices between gluons and Higgs bosons (Fig. 10.6). Note that all two-loop diagrams  
1855 with non-SM values of the Higgs couplings can be retrieved from their SM counterparts  
1856 by rescaling at amplitude-level:

$$\begin{aligned} \mathcal{M}_V(\Delta_1) &\rightarrow \mathcal{M}_V^{\text{SM}}(\Delta_1) \cdot c_t c_{hh} && (1^{\text{st}} \text{ row in Fig. 10.4}) \\ \mathcal{M}_V(\Delta_2) &\rightarrow \mathcal{M}_V^{\text{SM}}(\Delta_1) \cdot \frac{\hat{s} - m_h^2}{3m_h^2} c_{tt} && (2^{\text{nd}} \text{ row in Fig. 10.4}) \\ \mathcal{M}_V(\square) &\rightarrow \mathcal{M}_V^{\text{SM}}(\square) \cdot c_t^2 && (3^{\text{rd}}, 4^{\text{th}} \text{ rows in Fig. 10.4}), \end{aligned}$$

1857 where  $\mathcal{M}_V(\Delta_1)$  are the triangle diagrams from the 1<sup>st</sup> row of Fig. 10.4,  $\mathcal{M}_V(\Delta_2)$  from  
1858 the 2<sup>nd</sup> row (given by the corresponding diagrams from the 1<sup>st</sup> row where the  $s$ -channel  
1859 Higgs propagator gets pinched), and  $\mathcal{M}_V(\square)$  are the box-diagrams from the 3<sup>rd</sup> row.  
1860 Accordingly, we use the amplitudes computed in Ref. [219] for the pre-sampled set of  
1861 phase-space points and simply rescale them.

1862 Finally, real-emission diagrams contain five-point one-loop diagrams with SM-like  
1863 topologies, as well as tree diagrams carrying one effective coupling between gluons and  
1864 Higgs bosons from  $\mathcal{L}_4$  (Fig. 10.7).

### 1865 10.3 Total cross-sections for BSM benchmark points

1866 All results for total and differential cross-sections presented in this Chapter can be  
1867 found in Ref. [228]. To summarize, all HTL contributions were computed analytically

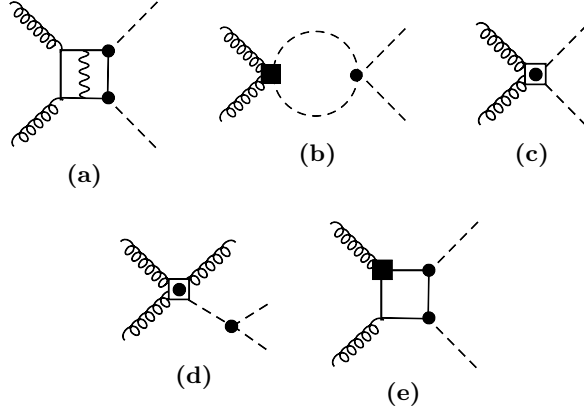


**Figure 10.3:** (a-d) Diagrams that do not scale like  $\alpha_s^4$  are consistently neglected. (e) The chromomagnetic operator  $Q_{ttG} = c_t g_s \bar{t}_L \sigma_{\mu\nu} G^{\mu\nu} t_R$  only contributes at two-loop order at least ( $d_\chi = 6$ ).

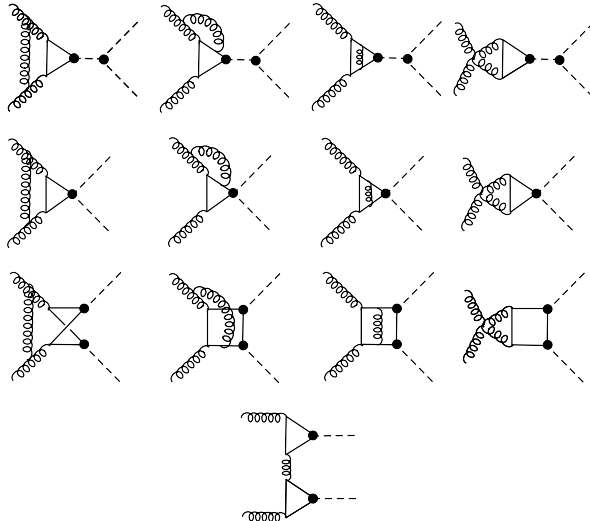


**Figure 10.4:** Two-loop diagrams generated by the EWChL at NLO QCD. They can all be computed by rescaling from the corresponding SM diagrams (see text).

with FORM. In  $\text{FT}_{\text{approx}}$  and in the full theory predictions, the real radiation is provided by GoSAM. A Universal FeynRules Output (UFO) model [229] for the EWChL was produced with FEYNRULES [230, 231] and interfaced to GoSAM to produce all tree and one-loop diagrams. The various parts are assembled into a C++ code which performs the phase-space integration with VEGAS as interfaced through the CUBA package.

The results shown below are produced at a center-of-mass energy of  $\sqrt{s} = 14$  TeV, where we use the PDF4LHC15\_nlo\_100\_pdfas interfaced through LHAPDF. The corresponding value of  $\alpha_s(\mu)$ , with  $\alpha_s(M_Z) = 0.118$ , is consistently employed throughout

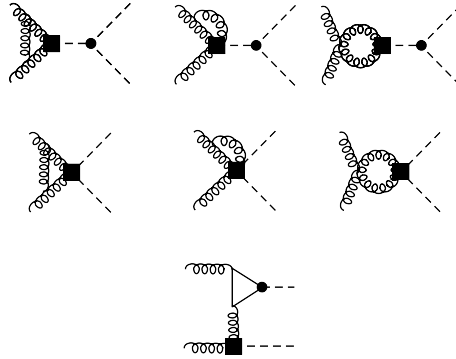


**Figure 10.5:** One-loop virtual contributions at NLO QCD: these diagrams contain exactly one effective contact coupling from  $\mathcal{L}_4$ .

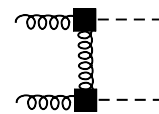


**Figure 10.6:** Tree diagram at NLO QCD containing exactly two effective couplings from  $\mathcal{L}_4$ .

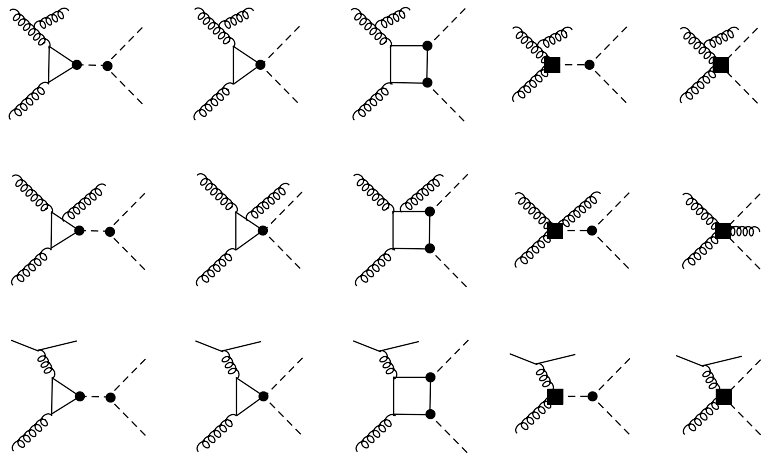


**Figure 10.7:** Real-emission contributions that are either one-loop diagrams without effective contact coupling, or tree diagrams with exactly one such coupling.

the calculation. The Higgs boson and top-quark masses are set to  $m_h = 125$  GeV and  $m_t = 173$  GeV, as the two-loop amplitudes were computed with these values, and both their widths are set to zero. Finally, the renormalization and factorization scales are set to  $\mu_R = \mu_F = \mu_0 = m_{hh}/2$  and uncertainties are estimated according to 7-point scale variations  $\mu_{R,F} = c_{R,F}\mu_0$  with  $(c_R, c_F) \in \{0.5, 1, 2\} \times \{0.5, 1, 2\} \setminus \{(0.5, 2), (2, 0.5)\}$ .

### 10.3 Total cross-sections for BSM benchmark points

1881 To characterize the 5-dimensional BSM space, the set of Higgs coupling variations  
 1882 used in the following part is based mostly on the definition of benchmark (BM) points  
 1883 presented in Ref. [232]. There, the BSM space is scanned for different values of the  
 1884 Higgs anomalous couplings and clustered into blocks that manifest a similar behavior in  
 1885 differential distributions. The set of BM points is defined in Table 10.1, and the total  
 1886 cross-sections,  $K$ -factors and uncertainties are shown in Table 10.2.

1887 First, looking at Table 10.2, the NLO cross-sections can become quite sizeable de-  
 1888 pending on the BM point considered (of  $\mathcal{O}(100)$  times the SM cross-section), and some  
 1889 are even excluded considering recent bounds on  $hh$  production from experimental lim-  
 1890 its. With the ATLAS current limit [16] on the observed non-resonant  $hh$  production  
 1891 cross-section of 220 fb at 95% CL, several BM points would indeed be excluded al-  
 1892 ready. Second, the full  $m_t$ -dependent NLO corrections are important, with  $K$ -factors  
 1893 between 1.66 and 2.34, and are accompanied by large scale uncertainties of  $\mathcal{O}(15 - 20\%)$   
 1894 (similarly to single Higgs production at NLO QCD [233, 234]). Finally, the  $K$ -factors  
 1895 themselves depend substantially on the considered BSM point. This is also illustrated  
 1896 in Fig. 10.8, where only one parameter is varied at a time. In fact, studies realized in  
 1897 the heavy-top limit suggest the  $K$ -factors's dependence on the different couplings to  
 1898 be quite small [235] (of  $\mathcal{O}(5\%)$  or less for all considered coupling variations). Once full  
 1899 top-quark loop corrections are taken into account, though, the  $K$ -factors for  $c_{hhh}$ ,  $c_{tt}$   
 1900 and  $c_t$  vary by more than 30% (55% for  $c_{tt}$ ). Later on, in Section 10.4, we will show  
 1901 that this feature is especially prominent around the top-quark pair  $2m_t$  threshold when  
 1902 considering differential distributions.

BM	$c_{hhh}$	$c_t$	$c_{tt}$	$c_{ggh}$	$c_{gggh}$
1	7.5	1.0	-1.0	0.0	0.0
2	1.0	1.0	0.5	$-\frac{1.6}{3}$	-0.2
3	1.0	1.0	-1.5	0.0	$\frac{0.8}{3}$
4	-3.5	1.5	-3.0	0.0	0.0
5	1.0	1.0	0.0	$\frac{1.6}{3}$	$\frac{1.0}{3}$
6	2.4	1.0	0.0	$\frac{0.4}{3}$	$\frac{0.2}{3}$
7	5.0	1.0	0.0	$\frac{0.4}{3}$	$\frac{0.2}{3}$
8a	1.0	1.0	0.5	$\frac{0.8}{3}$	0.0
9	1.0	1.0	1.0	-0.4	-0.2
10	10.0	1.5	-1.0	0.0	0.0
11	2.4	1.0	0.0	$\frac{2.0}{3}$	$\frac{1.0}{3}$
12	15.0	1.0	1.0	0.0	0.0
SM	1.0	1.0	0.0	0.0	0.0

**Table 10.1:** Different BM points in the 5-dimensional Higgs coupling space are analyzed below at inclusive, respectively differential cross-section level.

1903 Furthermore, the ratio of the cross-section to the SM can be parametrized [232, 236]  
 1904 in terms of the anomalous Higgs couplings: the cross-section ratio is expressed as a poly-  
 1905 nomial whose coefficients correspond to all squared/interference terms from the various  
 1906 diagrams. At LO, this gives 15 possible combinations:

BM	$\sigma_{\text{NLO}} [\text{fb}]$	$K$ -factor	scale uncertainties [%]	stat. uncertainties [%]	$\frac{\sigma_{\text{NLO}}}{\sigma_{\text{NLO,SM}}}$
$B_1$	194.89	1.88	$^{+19}_{-15}$	1.6	5.915
$B_2$	14.55	1.88	$^{+5}_{-13}$	0.56	0.4416
$B_3$	1047.37	1.98	$^{+21}_{-16}$	0.15	31.79
$B_4$	8922.75	1.98	$^{+19}_{-16}$	0.39	270.8
$B_5$	59.325	1.83	$^{+4}_{-15}$	0.36	1.801
$B_6$	24.69	1.89	$^{+2}_{-11}$	2.1	0.7495
$B_7$	169.41	2.07	$^{+9}_{-12}$	2.2	5.142
$B_{8a}$	41.70	2.34	$^{+6}_{-9}$	0.63	1.266
$B_9$	146.00	2.30	$^{+22}_{-16}$	0.31	4.431
$B_{10}$	575.86	2.00	$^{+17}_{-14}$	3.2	17.48
$B_{11}$	174.70	1.92	$^{+24}_{-8}$	1.2	5.303
$B_{12}$	3618.53	2.07	$^{+16}_{-15}$	1.2	109.83
SM	32.95	1.66	$^{+14}_{-13}$	0.1	1

**Table 10.2:** The total cross-sections for the considered BSM BM points, with their respective  $K$ -factors, scale and (MC) statistical uncertainties, as well as the ratio to the SM cross-section  $\sigma_{\text{NLO,SM}} = 32.95 \text{ fb}$ .

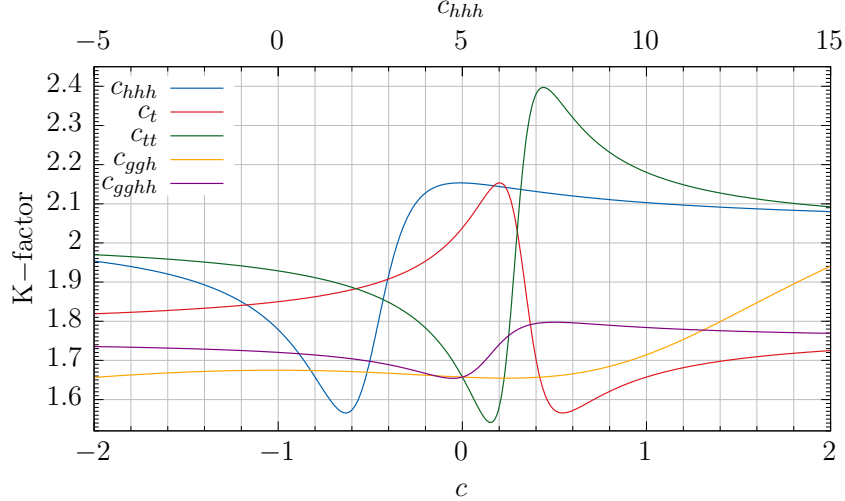


**Figure 10.8:** The  $K$ -factor is shown as a function of  $c_{hhh}$  on the top axis, and of the other couplings on the lower axis.

$$\begin{aligned}
 \sigma/\sigma_{SM} = & A_1 c_t^4 + A_2 c_{tt}^2 + A_3 c_t^2 c_{hhh}^2 + A_4 c_{ggh}^2 c_{hhh}^2 + A_5 c_{gggh}^2 + A_6 c_{tt} c_t^2 \\
 & + A_7 c_t^3 c_{hhh} + A_8 c_{tt} c_t c_{hhh} + A_9 c_{tt} c_{ggh} c_{hhh} + A_{10} c_{tt} c_{gggh} \\
 & + A_{11} c_t^2 c_{ggh} c_{hhh} + A_{12} c_t^2 c_{gggh} + A_{13} c_t c_{hhh}^2 c_{ggh} \\
 & + A_{14} c_t c_{hhh} c_{ggh} + A_{15} c_{ggh} c_{hhh} c_{gggh}. \tag{10.15}
 \end{aligned}$$

### 10.3 Total cross-sections for BSM benchmark points

1907 The coefficients  $A_1$  to  $A_{15}$  are corrected at NLO, and 8 new coefficients appear from  
 1908 genuine NLO diagrams:

$$\Delta\sigma/\sigma_{SM} = A_{16} c_t^3 c_{ggh} + A_{17} c_t c_{tt} c_{ggh} + A_{18} c_t c_{ggh}^2 c_{hhh} + A_{19} c_t c_{ggh} c_{gghh} \\ + A_{20} c_t^2 c_{ggh}^2 + A_{21} c_{tt} c_{ggh}^2 + A_{22} c_{ggh}^3 c_{hhh} + A_{23} c_{ggh}^2 c_{gghh}. \quad (10.16)$$

1909 These coefficients can be determined by dedicated event generation runs for a set of  
 1910 the 5-dimensional parameter space, and by projecting out a system of equations, or  
 1911 by a simple fit of the polynomial in Eq. (10.16) to the calculated set of cross-sections.  
 1912 The results for the NLO coefficients  $A_1$  to  $A_{23}$  at  $\sqrt{s} = 14$  TeV are given in Table C.1.  
 1913 Interestingly, once the cross-section coefficients are computed, the parametrization given  
 1914 in Eqs. (10.15), (10.16) yields the cross-section for any point of the BSM space. This  
 1915 for example allows to produce iso-contour plots where curves represent configurations in  
 1916 the BSM space which lead to the same cross-section, see Figs. 10.9, 10.10, 10.11. In the  
 1917 latter, two BSM couplings are simultaneously varied (within bounds still approximately  
 1918 allowed by experimental measurements), and iso-curves for the ratio to the SM cross-  
 1919 section at LO (red), respectively NLO (black), are shown.

1920 The cross-section iso-curves are given for  $c_{tt}$  against  $c_{gghh}$  in Fig. 10.9a, respectively  
 1921 against  $c_{ggh}$  in Fig. 10.9b. In both cases, the cross-section varies sizeably with respect  
 1922 to the SM value, and is generally more sensitive to changes in  $c_{tt}$ . The NLO corrections  
 1923 to  $hh$  introduce important shifts in the iso-curves (reflected by the large  $K$ -factors).  
 1924 Fig. 10.10 shows iso-contours for variations of  $c_{hhh}$  versus  $c_{ggh}$ , respectively  $c_{tt}$ . Again,  
 1925 the curves are much more dependent on  $c_{hhh}$  than on the Higgs contact coupling, as  
 1926 exhibited by Fig. 10.10a. In comparison, the dependence of the cross-section on  $c_{hhh}$   
 1927 and  $c_{tt}$  is large, with ratios to the SM cross-section going up to a factor  $\mathcal{O}(\sim 100)$ .  
 1928 Finally, iso-contours are also plotted for simultaneous variations of  $c_t$  versus  $c_{tt}$  and  $c_{hhh}$   
 1929 in Fig. 10.11.

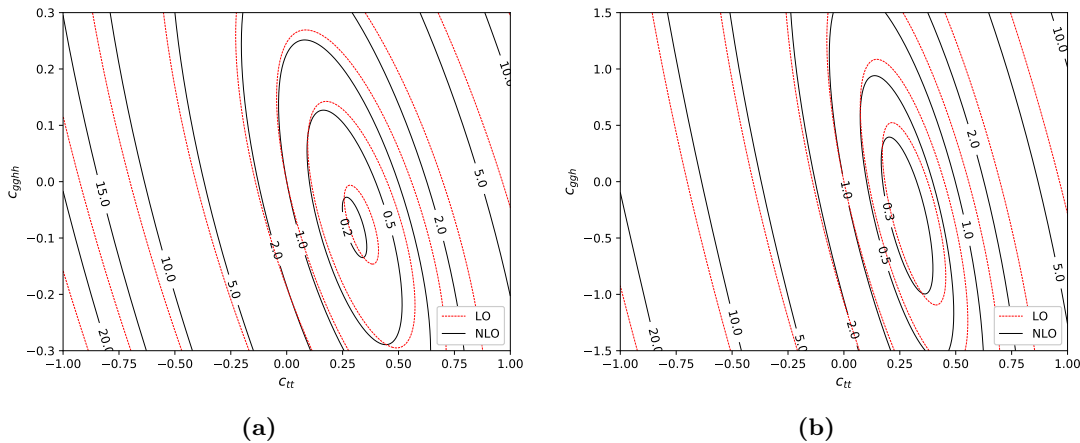


**Figure 10.9:** Iso-contours of  $\sigma/\sigma_{SM}$ : (a)  $c_{gghh}$  and (b)  $c_{ggh}$  versus  $c_{tt}$ .

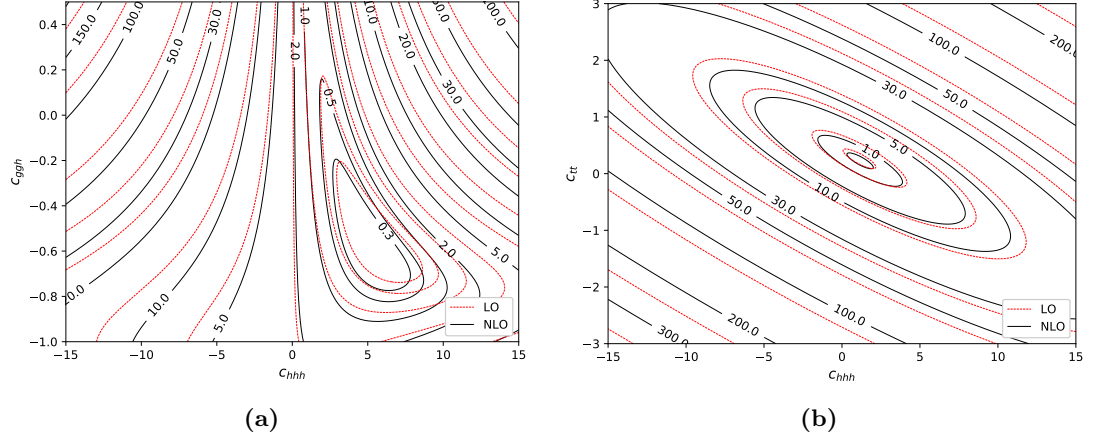


**Figure 10.10:** Iso-contours of  $\sigma/\sigma_{SM}$ : (a)  $c_{gg}$  and (b)  $c_{tt}$  versus  $c_{hh}$ .

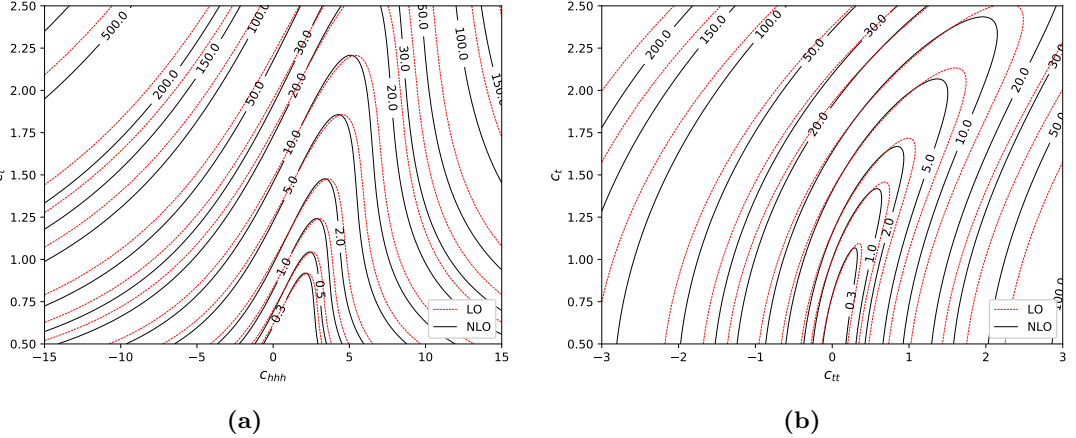


**Figure 10.11:** Iso-contours of  $\sigma/\sigma_{SM}$ : (a)  $c_t$  versus  $c_{hh}$  and (b)  $c_t$  versus  $c_{tt}$ .

## 10.4 Differential cross-sections and HTL approximations

Next, differential cross-sections are compared for the various approximations laid out in Section 10.1.1. We show distributions of the invariant mass of the Higgs boson pair system  $m_{hh}$  and the transverse momentum of one (any) Higgs  $p_{T,h}$  for a subset of the BM points defined in Table 10.2.

In Fig. 10.12, both distributions are displayed for the BM point 6: the SM distributions are plotted against the the BSM Born-improved,  $FT_{approx}$  and full predictions, respectively, both at LO and NLO. While the  $B_6$  total cross-section is similar to the SM value for all considered NLO approximations, the interference pattern between triangle- and box-like diagrams is very different. The  $m_{hh}$  observable in Fig. 10.12a manifests a

1940 dip around  $m_{hh} = 370$  GeV,<sup>5</sup> which would be a characteristic sign of BSM physics at  
 1941 the differential level. As a matter of fact, the chosen value of  $c_{hhh} = 2.4$  corresponds  
 1942 approximately to a maximal destructive interference between triangle- and box-like con-  
 1943 tributions when the other couplings are kept fixed at their SM values. Secondly, the  
 1944 differential  $K$ -factor shown in the first ratio plot (in red), which is found to be rel-  
 1945 atively flat in the usual HTL approximations, varies by more than 70% for the full  
 1946  $m_t$ -dependent NLO prediction. Finally, while both the Born-improved and FT<sub>approx</sub> de-  
 1947 scriptions show the largest difference to the full NLO calculation around the top-quark  
 1948 pair threshold (see the purple and green curves in the second ratio plot), they describe  
 1949 the tail of the  $m_{hh}$  distribution rather well. The same considerations apply to the  $p_{T,h}$   
 1950 distribution plotted in Fig. 10.12b.

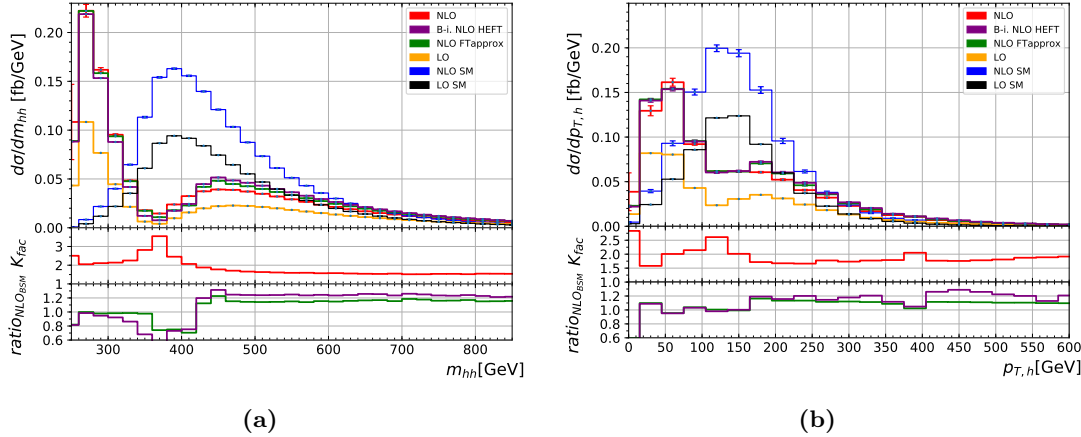


**Figure 10.12:** (a) Higgs boson pair invariant mass and (b) Higgs transverse momentum for BM point 6 ( $c_{hhh} = 2.4, c_t = 1, c_{tt} = 0, c_{ggh} = 2/15, c_{gghh} = 1/15$ ) with all considered  $hh$  production approximations.

1951 The same differential distributions are plotted for the BM point 9 in Fig. 10.13, which  
 1952 is characterized by SM values for  $c_{hhh}, c_t$  and non-zero values of  $c_{tt}$  and gluon-Higgs  
 1953 couplings  $c_{ggh}, c_{gghh}$ . In this case, the cross-section is much larger than the SM value.  
 1954 The anomalous gluon-Higgs coupling values also enhance the tail of both distributions  
 1955 (the dependence of the  $c_{gghh}$  term grows proportionally to the invariant  $\hat{s}$  in the limit  
 1956  $\hat{s} \rightarrow \infty$ ). Both NLO approximations fall short of describing the full prediction around  
 1957 the top-quark pair threshold and in the middle-range part of the  $m_{hh}$  distribution.

1958 Renormalization and factorization scale uncertainties are given along the central pre-  
 1959 diction for the BM point 5 in Fig. 10.14. This BM point is one example where, contrary  
 1960 to the SM case, the envelope is not given by the two most extreme scale variations  
 1961  $c_{R,F} \in \{(0.5, 0.5), (2, 2)\}$ , which both give downwards deviations. As for the SM point,  
 1962 the NLO BM prediction is not covered by the LO scale uncertainties. All BM points not  
 1963 shown here are given in Appendix C for completeness.

<sup>5</sup>The LO pure HTL amplitude vanishes at  $m_{hh} = 429$  GeV.

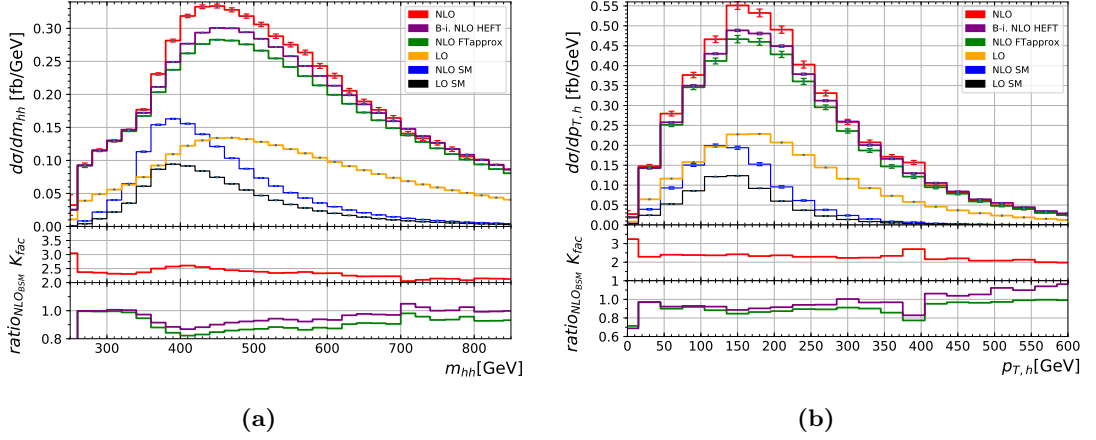


**Figure 10.13:** (a) Higgs boson pair invariant mass and (b) Higgs transverse momentum for BM point 9 ( $c_{hhh} = 1, c_t = 1, c_{tt} = 1, c_{ggh} = -0.4, c_{gggh} = -0.2$ ).

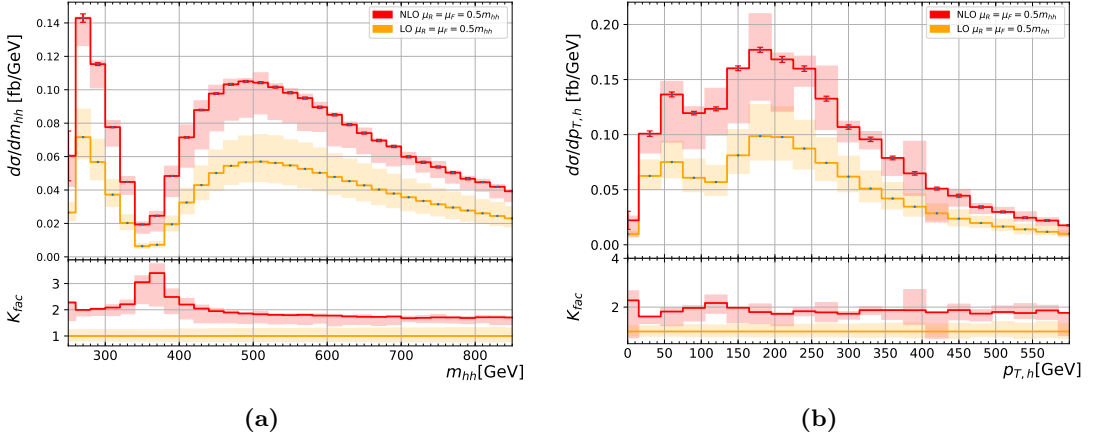


**Figure 10.14:** The (a)  $m_{hh}$  and (b)  $p_{T,h}$  distributions for BM point 5 ( $c_{hhh} = 1, c_t = 1, c_{tt} = 0, c_{ggh} = 8/15, c_{gggh} = 1/3$ ), along with  $\mu_R/\mu_F$  scale uncertainties.

Generally, the full  $m_t$ -dependent NLO prediction introduces a high dependence of the  $K$ -factor on both the anomalous Higgs couplings and at the differential level in distribution bins. For some BM points, the Born-improved and FT<sub>approx</sub> approximations fare rather poorly and should be replaced by the full theory prediction when comparing to experimentally measured cross-sections, for maximal exclusion limits on anomalous couplings. In particular, it should help identify updated BM points in the BSM space of anomalous Higgs couplings. In this prospect, we incorporate part of the EWChL setup presented above into a MC event generator available to experimentalists.

# <sup>1972</sup> 11 Variations of the triple Higgs-coupling <sup>1973</sup> and parton-shower effects

<sup>1974</sup> Having considered the extension of the SM through the EWChL and the effects of the  
<sup>1975</sup> full NLO QCD corrections due to the top-quark loops in  $hh$  production, we present its  
<sup>1976</sup> implementation in a full-fledged MC event generator. Numerical results and differential  
<sup>1977</sup> distributions are given in more detail in Ref. [228]. A version of the  $m_t$ -dependent prediction  
<sup>1978</sup> at NLO was already implemented in the case of the SM in the POWHEG-BOX-V2  
<sup>1979</sup> package `UserProcesses-V2/ggHH`. We extend it to allow for variations of both the Higgs  
<sup>1980</sup> boson trilinear self-coupling  $\lambda$  and the top-Higgs Yukawa coupling  $y_t$ : the result is a public  
<sup>1981</sup> MC generator that permits full particle-level production. In particular, Higgs bosons  
<sup>1982</sup> are allowed to decay, and the fixed-order calculation can be matched to a parton-shower  
<sup>1983</sup> and hadronization package. In this Chapter, we briefly present the working mode of  
<sup>1984</sup> the POWHEG-BOX MC generator. The interfacing of the two-loop contribution to  $hh$   
<sup>1985</sup> production (including the aforementioned coupling variations) is explained, and NLO  
<sup>1986</sup> cross-sections at  $\sqrt{s} = 13, 14, 27$  TeV, as well as differential distributions at  $\sqrt{s} = 14$  TeV  
<sup>1987</sup> are shown. Finally, the matching of the fixed-order NLO calculation to a parton-shower  
<sup>1988</sup> is studied in more depth, and shower-related systematic uncertainties are estimated.

## <sup>1989</sup> 11.1 The Powheg-BOX framework

<sup>1990</sup> The POWHEG-BOX framework [17–19] is a `fortran` MC event generator skeleton that  
<sup>1991</sup> handles MC integration and event production for any arbitrary NLO process, supposing  
<sup>1992</sup> the user grants the few necessary input ingredients for the calculation, namely a  
<sup>1993</sup> parametrization of phase-space and the different contributions to the amplitude. The  
<sup>1994</sup> POWHEG-BOX also constitutes a repository of previously calculated processes which  
<sup>1995</sup> are made publicly available. In the following, we use the second version of the program  
<sup>1996</sup> POWHEG-BOX-V2. The POWHEG formalism bases on the following formula for the  
<sup>1997</sup> hardest emission:

$$d\sigma_{\text{NLO}} = d\Phi_m \bar{B}(\Phi_m) \left( \Delta(p_{T,\min}, \mu^2) + \int_{p_{T,\min}} d\Phi_1 \Delta(p_T, \mu^2) \frac{R(\Phi_{m+1})}{B(\Phi_m)} \Theta(\mu^2 - p_T) \right), \quad (11.1)$$

<sup>1998</sup> where  $p_{T,\min}$  is the parton-shower IR cutoff,  $\mu^2$  is the shower starting scale,  $B$  and  $R$  are  
<sup>1999</sup> the Born and the real-emission matrix-elements, and  $\bar{B}$  represents the Born underlying  
<sup>2000</sup> configuration. Note that in general, the transverse momentum could be replaced by  
<sup>2001</sup> any other shower evolution variable. The function  $\Delta$  is the Sudakov form factor (see

## 11 Variations of the triple Higgs-coupling and parton-shower effects

2002 Section 4.2.2) yielding the probability of no-emission above a given scale. In the POWHEG  
 2003 notation,

$$\Delta(t_0, t) = \exp \left( - \int d\Phi_1 \frac{R(\Phi_{m+1})\Theta(t - t_0)}{B(\Phi_m)} \right). \quad (11.2)$$

2004 For more details, the reader is referred to Ref. [18]. The workflow is quite simple and  
 2005 separates into four stages:

- 2006 • An importance sampling grid for the integration is determined: if run in parallel  
 2007 mode, POWHEG generates importance sampling grids for each seed and subse-  
 2008 quently combines them into one and stores the result in a `pwgxgrid.dat` file.
- 2009 • An upper bounding envelope is determined for the underlying Born kinematics  
 2010 cross-section  $\bar{B}$  and stored into a `pwggrid.dat` file.
- 2011 • The upper bound for the normalization of the radiation function  $R(\Phi_{m+1})/B(\Phi_m)$   
 2012 is found, and stored into a `pwgubound.dat` file.
- 2013 • Events can be generated in the LHE format, and run in parallel. Files `pwgevents.lhe`  
 2014 are produced and can then be fed to a parton-shower algorithm later on.

### 2015 11.2 Interfacing two-loop contributions

2016 The grid of pre-sampled phase-space points amplitudes used for producing the results of  
 2017 Chapter 10 is stored and has to be interfaced to POWHEG. As a first point, the program  
 2018 has to be able to call the virtual amplitude at any phase-space point (without having to  
 2019 recompute the expensive two-loop integrals for any possible kinematics  $(\hat{s}, \hat{t})$ ). In the SM  
 2020 `ggHH` program [237], this is handled by setting up a Python interface that interpolates  
 2021 the 2-dimensional grid: first, the  $(\hat{s}, \hat{t})$  phase-space is re-parametrized into new variables  
 2022  $(x, c_\theta)$  to produce an almost uniform distribution of phase-space points. This is achieved  
 2023 by choosing

$$x = f(\beta(\hat{s})), \quad c_\theta = |\cos(\theta)| = \left| \frac{\hat{s} + 2\hat{t} - 2m_h^2}{\hat{s}\beta(\hat{s})} \right|, \quad \beta = \sqrt{1 - \frac{4m_h^2}{\hat{s}}} \quad (11.3)$$

2024 with  $f$  any monotonic function. In this case,  $f(\beta(\hat{s}))$  is chosen to be the cumulative  
 2025 distribution function of the phase-space points generated in Ref. [219]. A uniform grid in  
 2026 the  $(x, c_\theta)$  space is generated, and the result at each point is set by linearly interpolating  
 2027 the amplitude using the neighbouring points computed by `SECDEC`. The amplitude at  
 2028 any phase-space points is then interpolated using the Clough-Tougher scheme in `SciPy`,  
 2029 which allows for a high numerical stability. For details on the grid performance and  
 2030 caveats, the reader is referred to Ref. [237].

2031 The implementation of variations of the Higgs trilinear self-coupling  $\lambda$  bases on a  
 2032 simple observation: at all orders (in QCD), the full amplitude for di-Higgs production  
 2033 is a second-order polynomial in  $\lambda$ ,

$$M_\lambda \equiv |\mathcal{M}_\lambda|^2 = A + B \lambda + C \lambda^2 . \quad (11.4)$$

2034 Thus knowing the amplitude for three values of  $\lambda$  allows to interpolate the matrix-  
 2035 element to any other arbitrary value. In our case, grids of the virtual amplitudes are  
 2036 produced for  $\lambda \in \{-1, 0, 1\}$ . Before starting the POWHEG run, the three grids are  
 2037 combined to a new grid containing the virtual amplitude for the user-given value of the  
 2038 Higgs self-coupling by simple Lagrange interpolation,

$$M_\lambda = M_{\lambda=0} (1 - \lambda^2) + \frac{M_{\lambda=1}}{2} (\lambda + \lambda^2) + \frac{M_{\lambda=-1}}{2} (-\lambda + \lambda^2) , \quad (11.5)$$

2039 where the uncertainties on the three amplitudes are added in quadrature. This grid is  
 2040 then further propagated to the Clough-Tougher interpolation routine. Note that in the  
 2041 BSM case, we also include points at 100 TeV in the grid to further improve statistics  
 2042 at higher center-of-mass energies, and by extension, in distribution tails. On the other  
 2043 hand, because BSM distributions differ in shape from the SM case (for example, see  
 2044 Fig. 11.2), phase-space regions that could well be populated for certain values of the  
 2045 anomalous couplings are not always well-sampled by the SM grid.

### 2046 11.3 Total and differential cross-sections at fixed-order

2047 We use the PDF4LHC15\_nlo\_30\_pdfas set interfaced to POWHEG-BOX-V2 through  
 2048 LHAPDF. Jets are clustered by the anti- $k_T$  algorithm [238] from **FastJet**, with a jet  
 2049 radius parameter of  $R = 0.4$  and a minimum transverse momentum  $p_{T,\min}^{\text{jet}} = 20 \text{ GeV}$ .  
 2050 Otherwise, the same setup presented in Section 10.3 is used for the next results. Note  
 2051 that the nomenclature is different, with respect to Chapter 10, for variations of the Higgs  
 2052 trilinear coupling and the top-Higgs Yukawa coupling: the Higgs self-coupling ratio to  
 2053 the SM value, formerly called  $c_{hhh}$ , is replaced by  $\kappa_\lambda$  (in reference to the widely-used  
 2054 experimental  $\kappa$  framework), and the top-Higgs Yukawa coupling ratio  $c_t$  is now named  
 2055  $y_t$ .

2056 Total cross-sections for various values of  $\kappa_\lambda = \lambda/\lambda_{\text{SM}}$  were computed for  $\sqrt{s} = 13, 14$   
 2057 and 27 TeV and are displayed in Table 11.1. Note again that the cross-section has a  
 2058 minimum around  $\kappa_\lambda \sim 2.4$ , for which the interference between triangle- and box-like  
 2059 diagrams is at its most destructive. The  $K$ -factor is plotted in Fig. 11.1 as a function  
 2060 of the Higgs self-coupling, this time ranging over the full, not yet excluded region for  $\kappa_\lambda$ .

2061 The distribution of the invariant mass of the Higgs boson pair  $hh$  is shown for the  
 2062 considered values of  $\kappa_\lambda$  in Fig. 11.2 with their respective scale uncertainties. For values  
 2063 of  $\kappa_\lambda$  that lead to minimal cross-section, the interference pattern is well-recognizable  
 2064 with a dip around  $m_{hh} \sim 350 \text{ GeV}$ , near the top-pair threshold. For greater values of  
 2065  $|\kappa_\lambda|$ , this dip completely disappears and the enhanced triangle-like contribution tends  
 2066 to populate the lower  $m_{hh}$ -region. A similar behavior is observed for the transverse  
 2067 momentum of one (any) Higgs boson, as presented in Fig. 11.3, although the effect is  
 2068 partly washed out.

$\lambda_{\text{BSM}}/\lambda_{\text{SM}}$	$\sigma_{\text{NLO}}@13\text{TeV} [\text{fb}]$	$\sigma_{\text{NLO}}@14\text{TeV} [\text{fb}]$	$\sigma_{\text{NLO}}@27\text{TeV} [\text{fb}]$	K-factor@14TeV
-1	$116.71^{+16.4\%}_{-14.3\%}$	$136.91^{+16.4\%}_{-13.9\%}$	504.9	1.86
0	$62.51^{+15.8\%}_{-13.7\%}$	$73.64^{+15.4\%}_{-13.4\%}$	275.29	1.79
1	$27.84^{+11.6\%}_{-12.9\%}$	$32.88^{+13.5\%}_{-12.5\%}$	$127.7^{+11.5\%}_{-10.4\%}$	1.66
2	$12.42^{+13.1\%}_{-12.0\%}$	$14.75^{+12.0\%}_{-11.8\%}$	59.10	1.56
2.4	$11.65^{+13.9\%}_{-12.7\%}$	$13.79^{+13.5\%}_{-12.5\%}$	53.67	1.65
3	$16.28^{+16.2\%}_{-15.3\%}$	$19.07^{+17.1\%}_{-14.1\%}$	69.84	1.90
5	$81.74^{+20.0\%}_{-15.6\%}$	$95.22^{+19.7\%}_{-11.5\%}$	330.61	2.14

**Table 11.1:** The cross-sections for di-Higgs production at full NLO QCD are given for  $\sqrt{s} = 13, 14$  and  $27 \text{ TeV}$  with scale uncertainties for several values of  $\kappa_\lambda = \lambda/\lambda_{\text{SM}}$ .

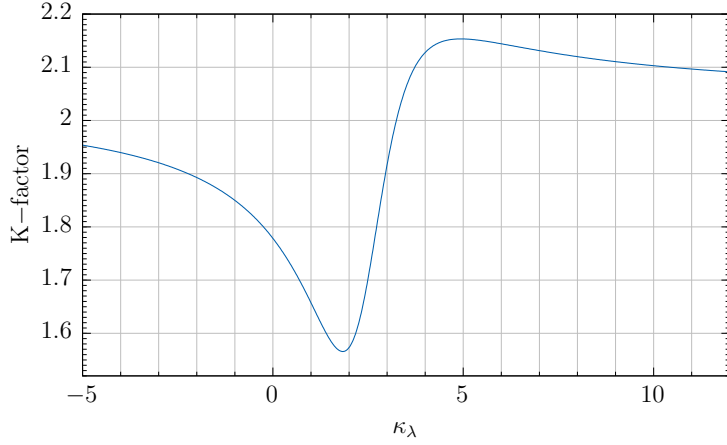


**Figure 11.1:** The full-theory NLO QCD  $K$ -factor is plotted as a function of the trilinear Higgs self-coupling  $\kappa_\lambda$ .

Furthermore, variations of the top-Higgs Yukawa coupling  $y_t$  can be recovered by a trick: allowing for  $y_t$  variations changes Eq. (11.4) into

$$|\mathcal{M}|^2 = y_t^4 \left[ \mathcal{M}_B \mathcal{M}_B^* + \frac{\lambda}{y_t} (\mathcal{M}_B \mathcal{M}_T^* + \mathcal{M}_T \mathcal{M}_B^*) + \frac{\lambda^2}{y_t^2} \mathcal{M}_T \mathcal{M}_T^* \right], \quad (11.6)$$

where  $\mathcal{M}_B$  is the box- and  $\mathcal{M}_T$  is the triangle contribution, and only the ratio  $\frac{\lambda}{y_t}$  appears up to an overall factor. So, it suffices to generate events with the value of  $\lambda$  corresponding to the desired value of the ratio  $\frac{\lambda}{y_t}$ , and finally rescale all results by  $y_t^4$ . For example, to produce results for  $\kappa_\lambda = 1, y_t = 0.8$ , the cross-section is given by

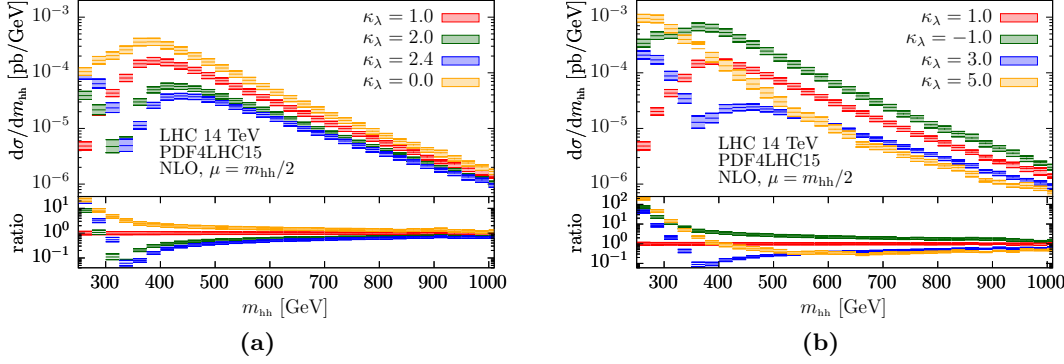


**Figure 11.2:** The Higgs boson pair invariant mass distributions for different values of  $\kappa_\lambda$  are given at  $\sqrt{s} = 14$  TeV.

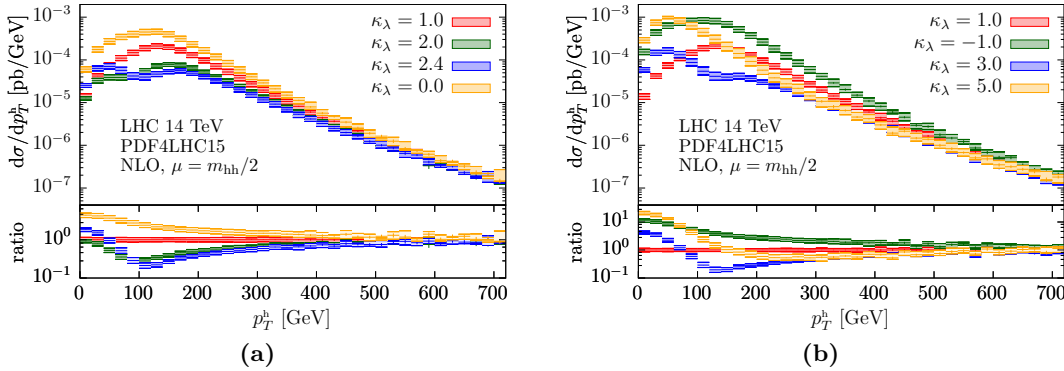


**Figure 11.3:** The transverse momentum of one (any) Higgs boson is shown for several values of  $\kappa_\lambda$  at  $\sqrt{s} = 14$  TeV.

$$d\sigma_{\text{NLO}}(\kappa_\lambda = 1, y_t = 0.8) = (0.8)^4 \cdot d\sigma_{\text{NLO}} \left( y_t = 1, \kappa_\lambda = \frac{1}{0.8} = 1.25 \right). \quad (11.7)$$

2075 Both  $m_{hh}$  and  $p_T^h$  distributions are displayed for  $y_t$ -values close to the currently ex-  
2076 cluded region in Fig. 11.4.

## 2077 11.4 Parton-shower matched predictions at NLO

2078 To be used by experimentalists for full simulation, the fixed-order calculation is matched  
2079 to a parton-shower (whose final-state can also be hadronized later on) within POWHEG.  
2080 In the fourth generation stage presented above, POWHEG generates full parton-level  
2081 events and stores them in LHE files. These can then be used as input to most modern  
2082 parton-shower programs. For our purposes, two different parton-shower programs are

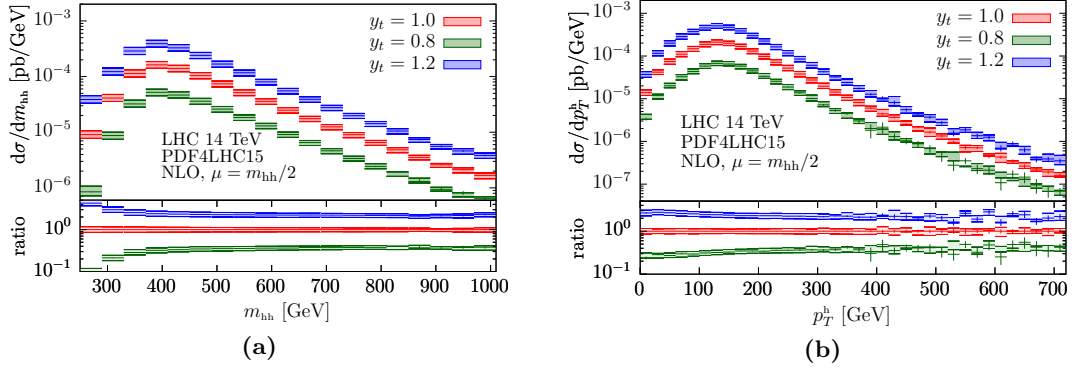


**Figure 11.4:** (a) The invariant mass of the Higgs boson pair system and (b) the transverse momentum of one Higgs boson are shown for three values of  $y_t$ . The procedure for generating  $y_t$ -varied events is explained in the text.

employed, namely **Pythia** 8.235 and **Herwig**7.1.4. Additionally, both the angular-ordered (so called  $\tilde{q}$ ) and the dipole shower algorithms present in **Herwig** are applied. The interfacing of both programs to POWHEG is mostly automatized: we use the standard **UserHooks** based on the **main31** LHE showering routine from **Pythia** to set the shower  $p_T$  definitions and vetoes (see Appendix D). For **Herwig**7, a process-independent interface library is present since revision r3591 of the POWHEG-BOX-V2 which sets the **LHEReader** class and handles the **Herwig** output for the event analysis. Finally, in both showers, we leave the tunes to their default values. Note that the Sudakov form factor is automatically included by POWHEG when producing LHE files. The POWHEG  $h_{\text{damp}}$  parameter is kept fixed throughout the next Section and set to  $h_{\text{damp}} = 250$  GeV.

In Fig. 11.5a, the transverse momentum of one (any) Higgs boson  $p_T^h$  is shown for the fixed-order NLO prediction, as well as the matched predictions to the three different shower algorithms: **Pythia** 8 (PP8), and both the angular-ordered  $\tilde{q}$  shower (PH7- $\tilde{q}$ ) and the dipole shower (PH7-dipole) from **Herwig**. For variables that are inclusive in the additional radiation, like  $p_T^h$ , all predictions are very much identical. In the case of variables that are sensitive to real emission, like the angular distance of both Higgs bosons  $\Delta R^{hh} = \sqrt{(\eta_1 - \eta_2)^2 + (\phi_1 - \phi_2)^2}$  shown in Fig. 11.5b, the showered predictions differ from the NLO calculation. There, the Sudakov exponent effectively resums radiation around  $\Delta R^{hh} = \pi$ , where the Higgs bosons are close to a back-to-back configuration. In addition, the parton-shower starts populating the region  $\Delta R^{hh} < \pi$ . Also, differences between the **Pythia** and **Herwig** parton-showers are already visible: while both **Herwig** showers produce very similar results, **Pythia** overshoots their prediction by  $\sim 50\%$ .

The differences between both parton-shower programs become more obvious when considering the transverse momentum of the Higgs boson pair system  $p_T^{hh}$ , displayed in Fig. 11.6 for two values of the Higgs trilinear coupling  $\kappa_\lambda = 1$ ,  $\kappa_\lambda = 2.4$ . In that case, both **Pythia** and **Herwig** agree at low transverse momentum, until they start to deviate at  $p_T^{hh} \sim 100$  GeV already. Then, while both **Herwig** showers correctly reproduce the hard NLO emission in the high- $p_T^{hh}$  region, the **Pythia** parton-shower produces much

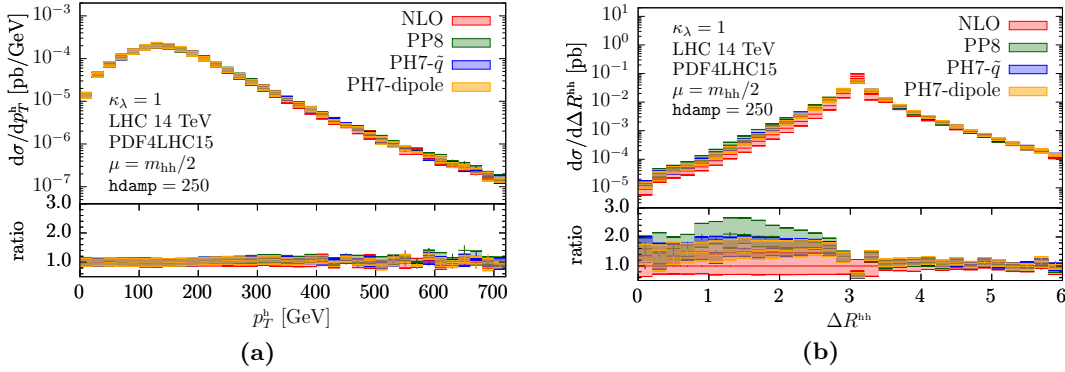


**Figure 11.5:** For the SM case  $\kappa_\lambda = 1$ , (a) the transverse momentum of one Higgs boson, and (b) the angular distance between both Higgs bosons are shown for the fixed-order NLO case, as well as for the three different parton-shower algorithms. The parton-level events from `POWHEG` are matched to `Pythia 8` (PP8), and to both the angular-ordered  $\tilde{q}$ -shower (PH7- $\tilde{q}$ ) and the dipole shower (PH7-dipole) from `Herwig7`.

harder radiation and its ratio to the fixed-order prediction stagnates at  $\sim 2$  over the remaining range. The harder spectrum from `Pythia` was found to be due to too hard sub-leading jets produced solely in the shower [239] as compared to the older `Pythia 6` parton-shower in di-Higgs production. In other processes, like  $t\bar{t}$  production, sizeable differences between `Pythia` and `Herwig` had also already been observed [240].

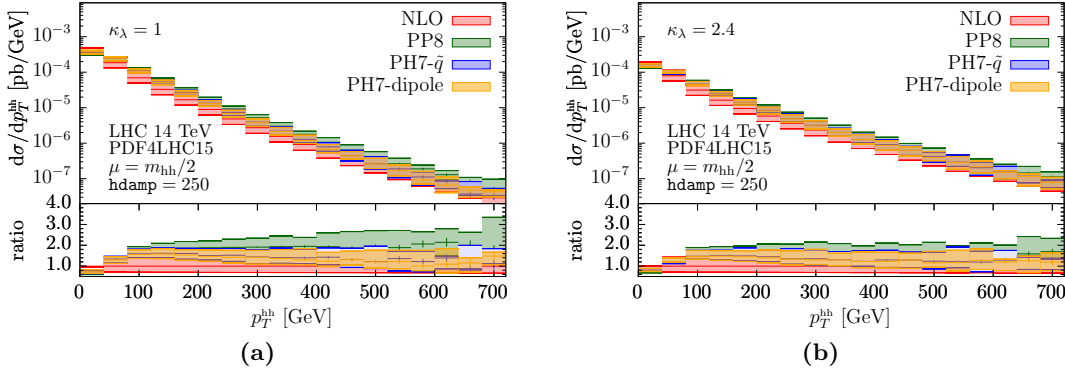


**Figure 11.6:** The NLO fixed-order prediction is compared to results from the three parton-shower algorithms with respect to the transverse momentum of the Higgs boson pair system  $p_T^{hh}$  for (a)  $\kappa_\lambda = 1$  and (b)  $\kappa_\lambda = 2.4$ .

As a way to estimate shower-matching uncertainties, the maximal tranverse momentum allowed for shower emissions can be set in `Herwig` by varying the so-called hard scale  $\mu_Q$ . The parameter `HardScaleFactor` is varied to  $c_Q = 0.5$ ,  $c_Q = 2$  and applied on the central hard shower scale separately for the up- and down-variations of the renormaliza-

2120 tiation and factorization scales  $\mu_{R,F}$ . In Fig. 11.7, the result is presented for the di-Higgs  
 2121 transverse momentum  $p_T^{hh}$  and the angular separation between the Higgs bosons  $\Delta R^{hh}$ .  
 2122 The shower scale variations add to the renormalization/factorizations scale uncertainties,  
 2123 bringing their common envelope to a corresponding 50% – 100% overall systematic  
 2124 uncertainty in the far- $p_T^{hh}$  region of the distribution. The differences between the cen-  
 2125 tral **Pythia** and **Herwig** predictions are then partly covered by the hard shower scale  
 2126 variations.

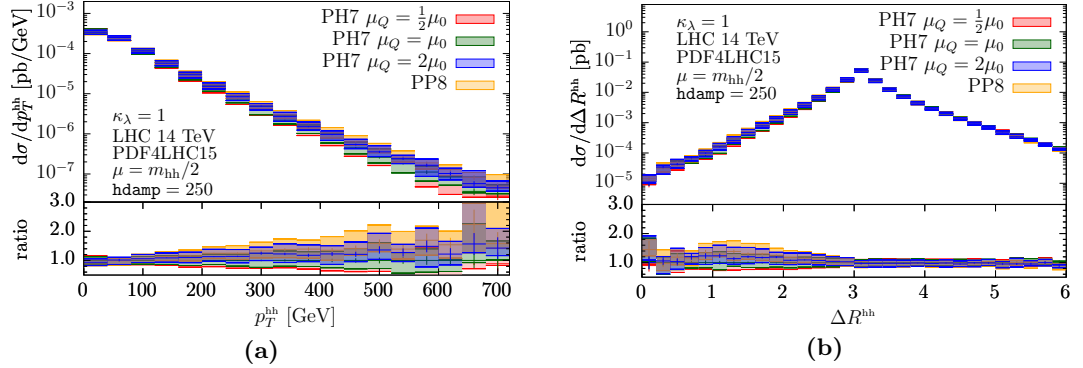


**Figure 11.7:** (a) The di-Higgs transverse momentum  $p_T^{hh}$  and (b) the angular separation  $\Delta R^{hh}$   
 between the Higgs bosons are shown for variations of the **Herwig** hard shower scale,  
 which regulates the maximal allowed transverse momentum of shower emissions.  
 The hard scale  $\mu_Q = c_Q \mu_0$  is varied by  $c_Q \in \{\frac{1}{2}, 2\}$  with respect to the default  
 scale  $\mu_0$ .

2127 All in all, considering both scale and parton-shower uncertainties, the Higgs pair  
 2128 process underlines the necessity of computing higher-order corrections in both fixed-order  
 2129 *and* resummation accuracy. In the future, it will be informative to study parton-shower  
 2130 (as well as other non-perturbative, e.g. hadronization) modeling effects in loop-induced  
 2131 color singlet production and try and reduce the sizeable associated uncertainties.

2132 **12 Conclusion and Outlook**



# Bibliography

- [1] PARTICLE DATA GROUP collaboration, *Review of particle physics*, *Phys. Rev. D* **98** (2018) 030001.
- [2] CDF collaboration, *Observation of Top Quark Production in  $\bar{p}p$  Collisions with the Collider Detector at Fermilab*, *Phys. Rev. Lett.* **74** (1995) 2626–2631.
- [3] D0 collaboration, *Observation of the top quark*, *Phys. Rev. Lett.* **74** (1995) 2632–2637.
- [4] “LHC Top Working Group.”  
<https://twiki.cern.ch/twiki/bin/view/LHCPhysics/LHCTopWG>.
- [5] ATLAS collaboration, *Measurement of the top quark mass in the  $t\bar{t} \rightarrow \text{lepton+jets}$  channel from  $\sqrt{s} = 8$  TeV ATLAS data and combination with previous results*, *Submitted to: Eur. Phys. J.* (2018) [arXiv:1810.01772].
- [6] CMS collaboration, *Measurement of the top quark mass using proton-proton data at  $\sqrt{s} = 7$  and 8 TeV*, *Phys. Rev.* **D93** (2016) 072004 [arXiv:1509.04044].
- [7] P. Marquard, A.V. Smirnov, V.A. Smirnov et al., *Quark Mass Relations to Four-Loop Order in Perturbative QCD*, *Phys. Rev. Lett.* **114** (2015) 142002 [arXiv:1502.01030].
- [8] M. Beneke and V.M. Braun, *Heavy quark effective theory beyond perturbation theory: Renormalons, the pole mass and the residual mass term*, *Nucl. Phys.* **B426** (1994) 301–343 [arXiv:hep-ph/9402364].
- [9] I.I.Y. Bigi, M.A. Shifman, N.G. Uraltsev et al., *The Pole mass of the heavy quark. Perturbation theory and beyond*, *Phys. Rev.* **D50** (1994) 2234–2246 [arXiv:hep-ph/9402360].
- [10] M. Beneke, *More on ambiguities in the pole mass*, *Phys. Lett.* **B344** (1995) 341–347 [arXiv:hep-ph/9408380].
- [11] A.H. Hoang, C. Lepenik and M. Preisser, *On the Light Massive Flavor Dependence of the Large Order Asymptotic Behavior and the Ambiguity of the Pole Mass*, *JHEP* **09** (2017) 099 [arXiv:1706.08526].
- [12] A.H. Hoang and I.W. Stewart, *Top Mass Measurements from Jets and the Tevatron Top-Quark Mass*, *Nucl. Phys. Proc. Suppl.* **185** (2008) 220–226 [arXiv:0808.0222].

## Bibliography

- 2164 [13] A.H. Hoang, S. Plätzer and D. Samitz, *On the Cutoff Dependence of the Quark  
2165 Mass Parameter in Angular Ordered Parton Showers*, *JHEP* **10** (2018) 200  
2166 [arXiv:1807.06617].
- 2167 [14] ATLAS collaboration, *Combined measurements of Higgs boson production and  
2168 decay using up to  $80 \text{ fb}^{-1}$  of proton-proton collision data at  $\sqrt{s} = 13 \text{ TeV}$   
2169 collected with the ATLAS experiment*, Tech. Rep. ATLAS-CONF-2018-031,  
2170 CERN, Geneva, Jul 2018.
- 2171 [15] CMS collaboration, *Combined measurements of the Higgs boson's couplings at  
2172  $\sqrt{s} = 13 \text{ TeV}$* , Tech. Rep. CMS-PAS-HIG-17-031, CERN, Geneva, 2018.
- 2173 [16] ATLAS collaboration, *Combination of searches for Higgs boson pairs in pp  
2174 collisions at 13 TeV with the ATLAS experiment.*, Tech. Rep.  
2175 ATLAS-CONF-2018-043, CERN, Geneva, Sep 2018.
- 2176 [17] P. Nason, *A New method for combining NLO QCD with shower Monte Carlo  
2177 algorithms*, *JHEP* **11** (2004) 040 [arXiv:hep-ph/0409146].
- 2178 [18] S. Frixione, P. Nason and C. Oleari, *Matching NLO QCD computations with  
2179 Parton Shower simulations: the POWHEG method*, *JHEP* **11** (2007) 070  
2180 [arXiv:0709.2092].
- 2181 [19] S. Alioli, P. Nason, C. Oleari et al., *A general framework for implementing NLO  
2182 calculations in shower Monte Carlo programs: the POWHEG BOX*, *JHEP* **06**  
2183 (2010) 043 [arXiv:1002.2581].
- 2184 [20] SUPER-KAMIOKANDE collaboration, *Evidence for oscillation of atmospheric  
2185 neutrinos*, *Phys. Rev. Lett.* **81** (1998) 1562–1567.
- 2186 [21] S.L. Glashow, *The renormalizability of vector meson interactions*, *Nuclear  
2187 Physics* **10** (1959) 107 – 117.
- 2188 [22] S. Weinberg, *A model of leptons*, *Phys. Rev. Lett.* **19** (1967) 1264–1266.
- 2189 [23] A. Salam and J.C. Ward, *Weak and electromagnetic interactions*, *Il Nuovo  
2190 Cimento* **11** (1959) 568–577.
- 2191 [24] D.J. Gross and F. Wilczek, *Ultraviolet behavior of non-abelian gauge theories*,  
2192 *Phys. Rev. Lett.* **30** (1973) 1343–1346.
- 2193 [25] H.D. Politzer, *Reliable perturbative results for strong interactions?*, *Phys. Rev.  
2194 Lett.* **30** (1973) 1346–1349.
- 2195 [26] ATLAS collaboration, *Standard Model Summary Plots Spring 2019*, Tech. Rep.  
2196 ATL-PHYS-PUB-2019-010, CERN, Geneva, Mar 2019.
- 2197 [27] F. Englert and R. Brout, *Broken symmetry and the mass of gauge vector mesons*,  
2198 *Phys. Rev. Lett.* **13** (1964) 321–323.

- 2199 [28] P.W. Higgs, *Broken symmetries and the masses of gauge bosons*, *Phys. Rev. Lett.*  
 2200 **13** (1964) 508–509.
- 2201 [29] G.S. Guralnik, C.R. Hagen and T.W.B. Kibble, *Global conservation laws and*  
 2202 *massless particles*, *Phys. Rev. Lett.* **13** (1964) 585–587.
- 2203 [30] J. Bardeen, L.N. Cooper and J.R. Schrieffer, *Theory of superconductivity*, *Phys.*  
 2204 *Rev.* **108** (1957) 1175–1204.
- 2205 [31] T.D. Lee, *A Theory of Spontaneous T Violation*, *Phys. Rev. D* **8** (1973)  
 2206 1226–1239.
- 2207 [32] S. Dimopoulos and H. Georgi, *Softly Broken Supersymmetry and SU(5)*, *Nucl.*  
 2208 *Phys.* **B193** (1981) 150–162.
- 2209 [33] LHC HIGGS CROSS SECTION WORKING GROUP collaboration, *Handbook of*  
 2210 *LHC Higgs Cross Sections: 4. Deciphering the Nature of the Higgs Sector*,  
 2211 [arXiv:1610.07922].
- 2212 [34] K.G. Chetyrkin and M.F. Zoller, *Three-loop  $\beta$ -functions for top-Yukawa and the*  
 2213 *Higgs self-interaction in the standard model*, *JHEP* **2012** (2012) 33.
- 2214 [35] S. Chigusa, T. Moroi and Y. Shoji, *State-of-the-Art Calculation of the Decay*  
 2215 *Rate of Electroweak Vacuum in the Standard Model*, *Phys. Rev. Lett.* **119** (2017)  
 2216 211801.
- 2217 [36] G. Degrassi, S. Di Vita, J. Elias-Miró et al., *Higgs mass and vacuum stability in*  
 2218 *the Standard Model at NNLO*, *JHEP* **2012** (2012) 98.
- 2219 [37] A.V. Bednyakov, B.A. Kniehl, A.F. Pikelner et al., *Stability of the electroweak*  
 2220 *vacuum: Gauge independence and advanced precision*, *Phys. Rev. Lett.* **115**  
 2221 (2015) 201802.
- 2222 [38] J. Schechter and J.W.F. Valle, *Neutrino masses in  $SU(2) \otimes U(1)$  theories*, *Phys.*  
 2223 *Rev. D* **22** (1980) 2227–2235.
- 2224 [39] T. Yanagida, *Horizontal Symmetry and Masses of Neutrinos*, *Progress of*  
 2225 *Theoretical Physics* **64** (1980) 1103–1105.
- 2226 [40] R.N. Mohapatra and G. Senjanovic, *Neutrino Mass and Spontaneous Parity*  
 2227 *Nonconservation*, *Phys. Rev. Lett.* **44** (1980) 912.
- 2228 [41] F. Borzumati, Y. Grossman, E. Nardi et al., *Neutrino masses and mixing in*  
 2229 *supersymmetric models without R parity*, *Phys. Lett.* **B384** (1996) 123–130  
 2230 [arXiv:hep-ph/9606251].
- 2231 [42] N. Haba, M. Matsuda and M. Tanimoto, *Large neutrino flavor mixings and*  
 2232 *gauge mediated supersymmetry breaking scenario*, *Phys. Lett.* **B478** (2000)  
 2233 351–357 [arXiv:hep-ph/9911511].

## Bibliography

- 2234 [43] B.S. DeWitt, *Quantum Theory of Gravity. I. The Canonical Theory*, *Phys. Rev.*  
2235 **160** (1967) 1113–1148.
- 2236 [44] B.S. DeWitt, *Quantum Theory of Gravity. II. The Manifestly Covariant Theory*,  
2237 *Phys. Rev.* **162** (1967) 1195–1239.
- 2238 [45] B.S. DeWitt, *Quantum Theory of Gravity. III. Applications of the Covariant  
2239 Theory*, *Phys. Rev.* **162** (1967) 1239–1256.
- 2240 [46] F. Zwicky, *Die Rotverschiebung von extragalaktischen Nebeln*, *Helvetica Physica  
2241 Acta* **6** (1933) 110–127.
- 2242 [47] H.W. Babcock, *The rotation of the Andromeda Nebula*, *Lick Observatory Bulletin*  
2243 **19** (1939) 41–51.
- 2244 [48] K.C. Freeman, *On the Disks of Spiral and S0 Galaxies*, **160** (1970) 811.
- 2245 [49] V.C. Rubin and W.K. Ford, Jr., *Rotation of the Andromeda Nebula from a  
2246 Spectroscopic Survey of Emission Regions*, **159** (1970) 379.
- 2247 [50] K.G. Begeman, A.H. Broeils and R.H. Sanders, *Extended rotation curves of  
2248 spiral galaxies - Dark haloes and modified dynamics*, **249** (1991) 523–537.
- 2249 [51] A.D. Sakharov, *Violation of CP Invariance, C asymmetry, and baryon  
2250 asymmetry of the universe*, *Pisma Zh. Eksp. Teor. Fiz.* **5** (1967) 32–35.
- 2251 [52] PLANCK collaboration, *Planck 2013 results. XVI. Cosmological parameters*,  
2252 *Astron. Astrophys.* **571** (2014) A16 [[arXiv:1303.5076](#)].
- 2253 [53] S. Weinberg, *Gauge Hierarchies*, *Phys. Lett.* **82B** (1979) 387–391.
- 2254 [54] M.D. Schwartz, *Quantum Field Theory and the Standard Model*. Cambridge  
2255 University Press, 2014.
- 2256 [55] M.E. Peskin and D.V. Schroeder, *An Introduction to Quantum Field Theory*.  
2257 Addison-Wesley, Reading, USA, 1995.
- 2258 [56] G. Isidori, *Lecture notes in Quantum Field Theory II*, Frühjahrsemester 2015.
- 2259 [57] G. Buchalla, *Lecture notes for Introduction to the SM*, Wintersemester 2008.
- 2260 [58] G. Heinrich, *Lecture notes for Colorful Loops: Introduction to Quantum  
2261 Chromodynamics and Loop Calculations*, Sommersemester 2018.
- 2262 [59] H.B.G. Casimir, *On the Attraction Between Two Perfectly Conducting Plates*,  
2263 *Indag. Math.* **10** (1948) 261–263.
- 2264 [60] G. 't Hooft and M. Veltman, *Regularization and renormalization of gauge fields*,  
2265 *Nuclear Physics B* **44** (1972) 189 – 213.

- [61] G. Passarino and M. Veltman, *One-loop corrections for  $e^+e^-$  annihilation into  $\mu^+\mu^-$  in the Weinberg model*, *Nuclear Physics B* **160** (1979) 151 – 207.
- [62] A. Denner and S. Dittmaier, *Reduction schemes for one-loop tensor integrals*, *Nucl. Phys.* **B734** (2006) 62–115 [arXiv:hep-ph/0509141].
- [63] T. Binoth, J.P. Guillet, G. Heinrich et al., *An algebraic/numerical formalism for one-loop multi-leg amplitudes*, *JHEP* **10** (2005) 015 [arXiv:hep-ph/0504267].
- [64] J.M. Campbell, E.W.N. Glover and D.J. Miller, *One loop tensor integrals in dimensional regularization*, *Nucl. Phys.* **B498** (1997) 397–442 [arXiv:hep-ph/9612413].
- [65] J. Fleischer, F. Jegerlehner and O.V. Tarasov, *Algebraic reduction of one loop Feynman graph amplitudes*, *Nucl. Phys.* **B566** (2000) 423–440 [arXiv:hep-ph/9907327].
- [66] A.I. Davydychev, *A Simple formula for reducing Feynman diagrams to scalar integrals*, *Phys. Lett.* **B263** (1991) 107–111.
- [67] C.G. Callan, *Broken scale invariance in scalar field theory*, *Phys. Rev. D* **2** (1970) 1541–1547.
- [68] K. Symanzik, *Small distance behaviour in field theory and power counting*, *Communications in Mathematical Physics* **18** (1970) 227–246.
- [69] K. Symanzik, *Small-distance-behaviour analysis and Wilson expansions*, *Communications in Mathematical Physics* **23** (1971) 49–86.
- [70] A.D. Martin, W.J. Stirling, R.S. Thorne et al., *Parton distributions for the LHC*, *The European Physical Journal C* **63** (2009) 189–285.
- [71] S. Hoeche, “SLAC Theoretical Physics, Monte-Carlo Simulations.” <https://theory.slac.stanford.edu/our-research/simulations>.
- [72] T. Hahn, *Cuba—a library for multidimensional numerical integration*, *Computer Physics Communications* **168** (2005) 78 – 95.
- [73] G.P. Lepage, *A new algorithm for adaptive multidimensional integration*, *Journal of Computational Physics* **27** (1978) 192 – 203.
- [74] J.H. Friedman and M.H. Wright, *A nested partitioning procedure for numerical multiple integration*, *ACM Trans. Math. Softw.* **7** (1981) 76–92.
- [75] W.H. Press and G.R. Farrar, *Recursive Stratified Sampling for Multidimensional Monte Carlo Integration*, *Computers in Physics* **4** (1990) 190–195.
- [76] J. Berntsen, T.O. Espelid and A. Genz, *An Adaptive Algorithm for the Approximate Calculation of Multiple Integrals*, *ACM Trans. Math. Softw.* **17** (1991) 437–451.

## Bibliography

- 2301 [77] A. Buckley, J. Ferrando, S. Lloyd et al., *LHAPDF6: parton density access in the*  
2302 *LHC precision era*, *The European Physical Journal C* **75** (2015) 132.
- 2303 [78] Z. Nagy, *Next-to-leading order calculation of three-jet observables in*  
2304 *hadron-hadron collisions*, *Phys. Rev. D* **68** (2003) 094002.
- 2305 [79] J.M. Campbell, R.K. Ellis and W.T. Giele, *A multi-threaded version of MCFM*,  
2306 *The European Physical Journal C* **75** (2015) 246.
- 2307 [80] J. Alwall, R. Frederix, S. Frixione et al., *The automated computation of tree-level*  
2308 *and next-to-leading order differential cross sections, and their matching to parton*  
2309 *shower simulations*, *JHEP* **2014** (2014) 79.
- 2310 [81] F. Cascioli, P. Maierhöfer and S. Pozzorini, *Scattering amplitudes with open*  
2311 *loops*, *Phys. Rev. Lett.* **108** (2012) 111601.
- 2312 [82] F. Buccioni, S. Pozzorini and M. Zoller, *On-the-fly reduction of open loops*, *The*  
2313 *European Physical Journal C* **78** (2018) 70.
- 2314 [83] G. Cullen, N. Greiner, G. Heinrich et al., *Automated one-loop calculations with*  
2315 *GoSam*, *The European Physical Journal C* **72** (2012) 1889.
- 2316 [84] G. Cullen, H. van Deurzen, N. Greiner et al., *GoSam-2.0: a tool for automated*  
2317 *one-loop calculations within the Standard Model and beyond*, *The European*  
2318 *Physical Journal C* **74** (2014) 3001.
- 2319 [85] S. Badger, B. Biedermann, P. Uwer et al., *Numerical evaluation of virtual*  
2320 *corrections to multi-jet production in massless QCD*, *Computer Physics*  
2321 *Communications* **184** (2013) 1981 – 1998.
- 2322 [86] K. Arnold, M. Bähr, G. Bozzi et al., *VBFNLO: A parton level Monte Carlo for*  
2323 *processes with electroweak bosons*, *Computer Physics Communications* **180**  
2324 (2009) 1661 – 1670.
- 2325 [87] J. Baglio et al., *VBFNLO: A Parton Level Monte Carlo for Processes with*  
2326 *Electroweak Bosons - Manual for Version 2.7.0*, [arXiv:1107.4038].
- 2327 [88] J. Baglio et al., *Release Note - VBFNLO 2.7.0*, [arXiv:1404.3940].
- 2328 [89] F. Campanario, T.M. Figy, S. Plätzer et al., *Electroweak Higgs Boson Plus Three*  
2329 *Jet Production at Next-to-Leading-Order QCD*, *Phys. Rev. Lett.* **111** (2013)  
2330 211802.
- 2331 [90] T. Binoth, F. Boudjema, G. Dissertori et al., *A proposal for a standard interface*  
2332 *between Monte Carlo tools and one-loop programs*, *Computer Physics*  
2333 *Communications* **181** (2010) 1612 – 1622.
- 2334 [91] S. Alioli, S. Badger, J. Bellm et al., *Update of the Binoth Les Houches Accord for*  
2335 *a standard interface between Monte Carlo tools and one-loop programs*, *Computer*  
2336 *Physics Communications* **185** (2014) 560 – 571.

- 2337 [92] P. Nogueira, *Automatic Feynman Graph Generation*, *Journal of Computational*  
 2338 *Physics* **105** (1993) 279 – 289.
- 2339 [93] J.A.M. Vermaseren, *New features of FORM*, [arXiv:math-ph/0010025].
- 2340 [94] T. Peraro, *Ninja: Automated integrand reduction via Laurent expansion for*  
 2341 *one-loop amplitudes*, *Computer Physics Communications* **185** (2014) 2771 – 2797.
- 2342 [95] G. Cullen, J.P. Guillet, G. Heinrich et al., *Golem95C: A library for one-loop*  
 2343 *integrals with complex masses*, *Computer Physics Communications* **182** (2011)  
 2344 2276 – 2284.
- 2345 [96] J.P. Guillet, G. Heinrich and J.F. von Soden-Fraunhofen, *Tools for NLO*  
 2346 *automation: extension of the Golem95C integral library*, *Comput. Phys.*  
 2347 *Commun.* **185** (2014) 1828–1834 [arXiv:1312.3887].
- 2348 [97] P. Mastrolia, G. Ossola, T. Reiter et al., *Scattering Amplitudes from*  
 2349 *Unitarity-based Reduction Algorithm at the Integrand-level*, *JHEP* **08** (2010) 080  
 2350 [arXiv:1006.0710].
- 2351 [98] R.K. Ellis and G. Zanderighi, *Scalar one-loop integrals for QCD*, *JHEP* **02**  
 2352 (2008) 002 [arXiv:0712.1851].
- 2353 [99] A. van Hameren, *Oneloop: For the evaluation of one-loop scalar functions*,  
 2354 *Computer Physics Communications* **182** (2011) 2427 – 2438.
- 2355 [100] S. Catani and M.H. Seymour, *A General algorithm for calculating jet*  
 2356 *cross-sections in NLO QCD*, *Nucl. Phys.* **B485** (1997) 291–419  
 2357 [arXiv:hep-ph/9605323].
- 2358 [101] G. Salam, *ICTP-SAIFR School on QCD and LHC physics*, Sao Paulo, Brazil,  
 2359 July 2015.
- 2360 [102] G. Altarelli and G. Parisi, *Asymptotic Freedom in Parton Language*, *Nucl. Phys.*  
 2361 **B126** (1977) 298–318.
- 2362 [103] Y.L. Dokshitzer, *Calculation of the Structure Functions for Deep Inelastic*  
 2363 *Scattering and  $e^+e^-$  Annihilation by Perturbation Theory in Quantum*  
 2364 *Chromodynamics.*, *Sov. Phys. JETP* **46** (1977) 641–653.
- 2365 [104] V.N. Gribov and L.N. Lipatov, *Deep inelastic ep scattering in perturbation*  
 2366 *theory*, *Sov. J. Nucl. Phys.* **15** (1972) 438–450.
- 2367 [105] M. Dasgupta, F.A. Dreyer, K. Hamilton et al., *Logarithmic accuracy of parton*  
 2368 *showers: a fixed-order study*, *JHEP* **09** (2018) 033 [arXiv:1805.09327].
- 2369 [106] M. Bahr et al., *Herwig++ Physics and Manual*, *Eur. Phys. J.* **C58** (2008)  
 2370 639–707 [arXiv:0803.0883].

## Bibliography

- 2371 [107] J. Bellm et al., *Herwig 7.0/Herwig++ 3.0 release note*, *Eur. Phys. J.* **C76** (2016)  
2372 196 [arXiv:1512.01178].
- 2373 [108] S. Frixione and B.R. Webber, *Matching NLO QCD computations and parton*  
2374 *shower simulations*, *JHEP* **2002** (2002) 029–029.
- 2375 [109] S. Frixione, P. Nason and C. Oleari, *Matching NLO QCD computations with*  
2376 *parton shower simulations: the POWHEG method*, *JHEP* **2007** (2007) 070–070.
- 2377 [110] S. Gieseke, P. Stephens and B. Webber, *New formalism for QCD parton showers*,  
2378 *JHEP* **12** (2003) 045 [arXiv:hep-ph/0310083].
- 2379 [111] T. Sjostrand, S. Mrenna and P.Z. Skands, *PYTHIA 6.4 Physics and Manual*,  
2380 *JHEP* **05** (2006) 026 [arXiv:hep-ph/0603175].
- 2381 [112] T. Sjostrand, S. Mrenna and P.Z. Skands, *A Brief Introduction to PYTHIA 8.1*,  
2382 *Comput. Phys. Commun.* **178** (2008) 852–867 [arXiv:0710.3820].
- 2383 [113] T. Gleisberg, S. Hoeche, F. Krauss et al., *Event generation with SHERPA 1.1*,  
2384 *JHEP* **02** (2009) 007 [arXiv:0811.4622].
- 2385 [114] B. Andersson, G. Gustafson, G. Ingelman et al., *Parton fragmentation and string*  
2386 *dynamics*, *Physics Reports* **97** (1983) 31 – 145.
- 2387 [115] T. Sjöstrand, S. Ask, J.R. Christiansen et al., *An introduction to PYTHIA 8.2*,  
2388 *Computer Physics Communications* **191** (2015) 159 – 177.
- 2389 [116] A. Kupco, *Cluster hadronization in HERWIG 5.9*, in *Monte Carlo generators for*  
2390 *HERA physics. Proceedings, Workshop, Hamburg, Germany, 1998-1999*,  
2391 292–300, 1998, [arXiv:hep-ph/9906412].
- 2392 [117] S. Gieseke, F. Loschaj and P. Kirchgässner, *Soft and diffractive scattering with the*  
2393 *cluster model in Herwig*, *The European Physical Journal C* **77** (2017) 156.
- 2394 [118] D. Amati and G. Veneziano, *Preconfinement as a property of perturbative QCD*,  
2395 *Physics Letters B* **83** (1979) 87–92.
- 2396 [119] O.S. Brüning, P. Collier, P. Lebrun et al., *LHC Design Report*, CERN Yellow  
2397 Reports: Monographs. CERN, Geneva, 2004.
- 2398 [120] O. Buning, P. Collier, P. Lebrun et al., *LHC Design Report. 2. The LHC*  
2399 *infrastructure and general services*, .
- 2400 [121] M. Benedikt, P. Collier, V. Mertens et al., *LHC Design Report. 3. The LHC*  
2401 *injector chain*, .
- 2402 [122] “CERN Official Website.”  
2403 <http://public.web.cern.ch/public/en/research/AccelComplex-en.html>.

- 2404 [123] ATLAS collaboration, *The ATLAS Experiment at the CERN Large Hadron  
2405 Collider*, *JINST* **3** (2008) S08003.
- 2406 [124] ATLAS collaboration, *Observation of Higgs boson production in association with  
2407 a top quark pair at the LHC with the ATLAS detector*, *Phys. Lett.* **B784** (2018)  
2408 173–191 [[arXiv:1806.00425](#)].
- 2409 [125] ATLAS collaboration, *Observation of light-by-light scattering in ultraperipheral  
2410 Pb+Pb collisions with the ATLAS detector*, .
- 2411 [126] ATLAS collaboration, *Study of the rare decays of  $B_s^0$  and  $B^0$  mesons into muon  
2412 pairs using data collected during 2015 and 2016 with the ATLAS detector*,  
2413 *Submitted to: JHEP* (2018) [[arXiv:1812.03017](#)].
- 2414 [127] ATLAS collaboration, *ATLAS inner detector: Technical design report*. Vol. 2, .
- 2415 [128] ATLAS collaboration, *ATLAS inner detector: Technical design report*. Vol. 1, .
- 2416 [129] ATLAS collaboration, *ATLAS pixel detector: Technical design report*, .
- 2417 [130] ATLAS collaboration, *Operation and performance of the ATLAS semiconductor  
2418 tracker*, *JINST* **9** (2014) P08009 [[arXiv:1404.7473](#)].
- 2419 [131] ATLAS TRT collaboration, *The ATLAS transition radiation tracker*, in  
2420 *Astroparticle, particle and space physics, detectors and medical physics*  
2421 *applications. Proceedings, 8th Conference, ICATPP 2003, Como, Italy, October*  
2422 *6-10, 2003*, 497–501, 2003, [[arXiv:hep-ex/0311058](#)], DOI.
- 2423 [132] A.S. Boldyrev et al., *The ATLAS transition radiation tracker*, *Instrum. Exp.  
2424 Tech.* **55** (2012) 323–334.
- 2425 [133] ATLAS collaboration, *ATLAS liquid-argon calorimeter: Technical Design  
2426 Report*, Technical Design Report ATLAS. CERN, Geneva, 1996.
- 2427 [134] ATLAS collaboration, *ATLAS tile calorimeter: Technical Design Report*,  
2428 Technical Design Report ATLAS. CERN, Geneva, 1996.
- 2429 [135] ATLAS collaboration, *ATLAS muon spectrometer: Technical Design Report*,  
2430 Technical Design Report ATLAS. CERN, Geneva, 1997.
- 2431 [136] D. Boscherini, *Performance and operation of the ATLAS Resistive Plate  
2432 Chamber system in LHC Run-1*, *JINST* **9** (2014) C12039.
- 2433 [137] K. Nikolopoulos et al., *Cathode strip chambers in ATLAS : Installation,  
2434 commissioning and in situ performance*, in *Proceedings, 2008 IEEE Nuclear  
2435 Science Symposium, Medical Imaging Conference and 16th International  
2436 Workshop on Room-Temperature Semiconductor X-Ray and Gamma-Ray  
2437 Detectors (NSS/MIC 2008 / RTSD 2008): Dresden, Germany, October 19-25,  
2438 2008*, 2819–2824, 2008, DOI.

## Bibliography

- 2439 [138] M. Livan, *Monitored drift tubes in ATLAS*, *Nuclear Instruments and Methods in*  
2440 *Physics Research Section A: Accelerators, Spectrometers, Detectors and*  
2441 *Associated Equipment* **384** (1996) 214 – 218.
- 2442 [139] K. Nagai, *Thin gap chambers in ATLAS*, *Nuclear Instruments and Methods in*  
2443 *Physics Research Section A: Accelerators, Spectrometers, Detectors and*  
2444 *Associated Equipment* **384** (1996) 219 – 221.
- 2445 [140] ATLAS collaboration, *Performance of the ATLAS Trigger System in 2010*, *The*  
2446 *European Physical Journal C* **72** (2012) 1849.
- 2447 [141] ATLAS collaboration, *The Run-2 ATLAS Trigger System*, *J. Phys. Conf. Ser.*  
2448 **762** (2016) 012003.
- 2449 [142] ATLAS collaboration, *Electron reconstruction and identification in the ATLAS*  
2450 *experiment using the 2015 and 2016 LHC proton-proton collision data at  $\sqrt{s} =$*   
2451 *13 TeV*, *Submitted to: Eur. Phys. J.* (2019) [arXiv:1902.04655].
- 2452 [143] ATLAS collaboration, *Muon reconstruction performance of the ATLAS detector*  
2453 *in proton–proton collision data at  $\sqrt{s} = 13$  TeV*, *Eur. Phys. J.* **C76** (2016) 292  
2454 [arXiv:1603.05598].
- 2455 [144] A. Hrynevich, *ATLAS jet and missing energy reconstruction, calibration and*  
2456 *performance in LHC run-2*, *Journal of Instrumentation* **12** (2017)  
2457 C06038–C06038.
- 2458 [145] ATLAS collaboration, *Performance of b-Jet Identification in the ATLAS*  
2459 *Experiment*, *JINST* **11** (2016) P04008 [arXiv:1512.01094].
- 2460 [146] GEANT4 collaboration, *GEANT4: A Simulation toolkit*, *Nucl. Instrum. Meth.*  
2461 **A506** (2003) 250–303.
- 2462 [147] E. Richter-Was, D. Froidevaux and L. Poggioli, *ATLFAST 2.0 a fast simulation*  
2463 *package for ATLAS*, .
- 2464 [148] ATLAS collaboration, *Measurement of the top quark mass with the template*  
2465 *method in the  $t\bar{t} \rightarrow$  lepton + jets channel using ATLAS data*, *The European*  
2466 *Physical Journal C* **72** (2012) 2046.
- 2467 [149] ATLAS collaboration, *Measurement of the top quark mass in the  $t\bar{t} \rightarrow$*   
2468 *lepton+jets and  $t\bar{t} \rightarrow$  dilepton channels using  $\sqrt{s} = 7$  TeV ATLAS data*, *The*  
2469 *European Physical Journal C* **75** (2015) 330.
- 2470 [150] ATLAS collaboration, *Measurement of the  $t\bar{t}$  production cross-section using  $e\mu$*   
2471 *events with b-tagged jets in pp collisions at  $\sqrt{s} = 7$  and 8TeV with the ATLAS*  
2472 *detector*, *The European Physical Journal C* **74** (2014) 3109.
- 2473 [151] ATLAS collaboration, *Measurement of the top quark mass in the  $t\bar{t}$  dilepton*  
2474 *channel from  $\sqrt{s} = 8$ TeV ATLAS data*, *Physics Letters B* **761** (2016) 350 – 371.

- 2475 [152] ATLAS collaboration, *Measurement of lepton differential distributions and the*  
 2476 *top quark mass in  $t\bar{t}$  production in  $pp$  collisions at  $\sqrt{s} = 8 \text{ TeV}$  with the ATLAS*  
 2477 *detector*, *The European Physical Journal C* **77** (2017) 804.
- 2478 [153] ATLAS collaboration, *Determination of the top-quark pole mass using  $t\bar{t} + 1\text{-jet}$*   
 2479 *events collected with the ATLAS experiment in 7 TeV  $pp$  collisions*, *JHEP* **2015**  
 2480 (2015) 121.
- 2481 [154] ATLAS collaboration, *Measurement of the top-quark mass in the fully hadronic*  
 2482 *decay channel from ATLAS data at  $\sqrt{s} = 7 \text{ TeV}$* , *The European Physical Journal C* **75** (2015) 158.
- 2484 [155] ATLAS collaboration, *Top-quark mass measurement in the all-hadronic  $t\bar{t}$  decay*  
 2485 *channel at  $\sqrt{s} = 8 \text{ TeV}$  with the ATLAS detector*, *JHEP* **2017** (2017) 118.
- 2486 [156] M. Czakon and A. Mitov, *Top++: A Program for the Calculation of the*  
 2487 *Top-Pair Cross-Section at Hadron Colliders*, *Comput. Phys. Commun.* **185**  
 2488 (2014) 2930 [[arXiv:1112.5675](#)].
- 2489 [157] ATLAS collaboration, *Studies on top-quark Monte Carlo modelling for Top2016*,  
 2490 Tech. Rep. ATL-PHYS-PUB-2016-020, CERN, Geneva, Sep 2016.
- 2491 [158] ATLAS collaboration, *Studies on top-quark Monte Carlo modelling with Sherpa*  
 2492 *and MG5\_aMC@NLO*, Tech. Rep. ATL-PHYS-PUB-2017-007, CERN, Geneva,  
 2493 May 2017.
- 2494 [159] ATLAS collaboration, *Investigation of systematic uncertainties on the*  
 2495 *measurement of the top-quark mass using lepton transverse momenta*, Tech. Rep.  
 2496 ATL-PHYS-PUB-2018-001, CERN, Geneva, Feb 2018.
- 2497 [160] ATLAS collaboration, *Improvements in  $t\bar{t}$  modelling using NLO+PS Monte*  
 2498 *Carlo generators for Run2*, Tech. Rep. ATL-PHYS-PUB-2018-009, CERN,  
 2499 Geneva, Jul 2018.
- 2500 [161] J.M. Campbell, R.K. Ellis, P. Nason et al., *Top-pair production and decay at*  
 2501 *NLO matched with parton showers*, *JHEP* **04** (2015) 114 [[arXiv:1412.1828](#)].
- 2502 [162] J. Bellm, S. Gieseke and S. Plätzer, *Merging NLO Multi-jet Calculations with*  
 2503 *Improved Unitarization*, *Eur. Phys. J.* **C78** (2018) 244 [[arXiv:1705.06700](#)].
- 2504 [163] S. Hoeche, F. Krauss, P. Maierhoefer et al., *Next-to-leading order QCD*  
 2505 *predictions for top-quark pair production with up to two jets merged with a parton*  
 2506 *shower*, *Phys. Lett.* **B748** (2015) 74–78 [[arXiv:1402.6293](#)].
- 2507 [164] S. Höche, P. Maierhöfer, N. Moretti et al., *Next-to-leading order QCD predictions*  
 2508 *for top-quark pair production with up to three jets*, *Eur. Phys. J.* **C77** (2017) 145  
 2509 [[arXiv:1607.06934](#)].

## Bibliography

- 2510 [165] M. Czakon, D. Heymes and A. Mitov, *High-precision differential predictions for*  
2511 *top-quark pairs at the LHC*, *Phys. Rev. Lett.* **116** (2016) 082003  
2512 [[arXiv:1511.00549](#)].
- 2513 [166] M. Czakon, D. Heymes and A. Mitov, *Dynamical scales for multi-TeV top-pair*  
2514 *production at the LHC*, *JHEP* **04** (2017) 071 [[arXiv:1606.03350](#)].
- 2515 [167] M. Czakon, D. Heymes and A. Mitov, *fastNLO tables for NNLO top-quark pair*  
2516 *differential distributions*, [[arXiv:1704.08551](#)].
- 2517 [168] M. Czakon, D. Heymes, A. Mitov et al., *Top-pair production at the LHC through*  
2518 *NNLO QCD and NLO EW*, *JHEP* **10** (2017) 186 [[arXiv:1705.04105](#)].
- 2519 [169] W. Hollik and D. Pagani, *The electroweak contribution to the top quark*  
2520 *forward-backward asymmetry at the Tevatron*, *Phys. Rev.* **D84** (2011) 093003  
2521 [[arXiv:1107.2606](#)].
- 2522 [170] J.H. Kühn, A. Scharf and P. Uwer, *Weak Interactions in Top-Quark Pair*  
2523 *Production at Hadron Colliders: An Update*, *Phys. Rev.* **D91** (2015) 014020  
2524 [[arXiv:1305.5773](#)].
- 2525 [171] D. Pagani, I. Tsinikos and M. Zaro, *The impact of the photon PDF and*  
2526 *electroweak corrections on  $t\bar{t}$  distributions*, *Eur. Phys. J.* **C76** (2016) 479  
2527 [[arXiv:1606.01915](#)].
- 2528 [172] W. Bernreuther, A. Brandenburg, Z.G. Si et al., *Top quark pair production and*  
2529 *decay at hadron colliders*, *Nucl. Phys.* **B690** (2004) 81–137  
2530 [[arXiv:hep-ph/0403035](#)].
- 2531 [173] K. Melnikov and M. Schulze, *NLO QCD corrections to top quark pair production*  
2532 *and decay at hadron colliders*, *JHEP* **0908** (2009) 049 [[arXiv:0907.3090](#)].
- 2533 [174] J.M. Campbell and R.K. Ellis, *Top-quark processes at NLO in production and*  
2534 *decay*, *J. Phys.* **G42** (2015) 015005 [[arXiv:1204.1513](#)].
- 2535 [175] M. Brucherseifer, F. Caola and K. Melnikov,  $\mathcal{O}(\alpha_s^2)$  *corrections to*  
2536 *fully-differential top quark decays*, *JHEP* **04** (2013) 059 [[arXiv:1301.7133](#)].
- 2537 [176] J. Gao and A.S. Papanastasiou, *Top-quark pair-production and decay at high*  
2538 *precision*, *Phys. Rev.* **D96** (2017) 051501 [[arXiv:1705.08903](#)].
- 2539 [177] M. Beneke, P. Falgari, S. Klein et al., *Hadronic top-quark pair production with*  
2540 *NNLL threshold resummation*, *Nucl. Phys.* **B855** (2012) 695–741  
2541 [[arXiv:1109.1536](#)].
- 2542 [178] M. Cacciari, M. Czakon, M. Mangano et al., *Top-pair production at hadron*  
2543 *colliders with next-to-next-to-leading logarithmic soft-gluon resummation*, *Phys.*  
2544 *Lett.* **B710** (2012) 612–622 [[arXiv:1111.5869](#)].

- 2545 [179] A. Ferroglio, S. Marzani, B.D. Pecjak et al., *Boosted top production: factorization*  
 2546 *and resummation for single-particle inclusive distributions*, *JHEP* **01** (2014) 028  
 2547 [[arXiv:1310.3836](#)].
- 2548 [180] A. Broggio, A.S. Papanastasiou and A. Signer, *Renormalization-group improved*  
 2549 *fully differential cross sections for top pair production*, *JHEP* **10** (2014) 98  
 2550 [[arXiv:1407.2532](#)].
- 2551 [181] N. Kidonakis, *High-order threshold corrections for top-pair and single-top*  
 2552 *production*, in *Proceedings, Meeting of the APS Division of Particles and Fields*  
 2553 (*DPF 2015*): *Ann Arbor, Michigan, USA, 4-8 Aug 2015*, 2015,  
 2554 [[arXiv:1509.07848](#)].
- 2555 [182] B.D. Pecjak, D.J. Scott, X. Wang et al., *Resummed differential cross sections for*  
 2556 *top-quark pairs at the LHC*, *Phys. Rev. Lett.* **116** (2016) 202001  
 2557 [[arXiv:1601.07020](#)].
- 2558 [183] M.L. Czakon et al., *Top quark pair production at NNLO+NNLL' in QCD*  
 2559 *combined with electroweak corrections*, in *11th International Workshop on Top*  
 2560 *Quark Physics (TOP2018) Bad Neuenahr, Germany, September 16-21, 2018*,  
 2561 [[arXiv:1901.08281](#)].
- 2562 [184] G. Heinrich, A. Maier, R. Nisius et al., *NLO QCD corrections to  $W^+W^-b\bar{b}$*   
 2563 *production with leptonic decays in the light of top quark mass and asymmetry*  
 2564 *measurements*, *JHEP* **1406** (2014) 158 [[arXiv:1312.6659](#)].
- 2565 [185] S. Frixione, E. Laenen, P. Motylinski et al., *Single-top hadroproduction in*  
 2566 *association with a  $W$  boson*, *JHEP* **07** (2008) 029 [[arXiv:0805.3067](#)].
- 2567 [186] A. Denner, S. Dittmaier, S. Kallweit et al., *NLO QCD corrections to  $WWbb$*   
 2568 *production at hadron colliders*, *Phys. Rev. Lett.* **106** (2011) 052001  
 2569 [[arXiv:1012.3975](#)].
- 2570 [187] A. Denner, S. Dittmaier, S. Kallweit et al., *NLO QCD corrections to off-shell*  
 2571 *top-antitop production with leptonic decays at hadron colliders*, *JHEP* **10** (2012)  
 2572 110 [[arXiv:1207.5018](#)].
- 2573 [188] G. Bevilacqua, M. Czakon, A. van Hameren et al., *Complete off-shell effects in*  
 2574 *top quark pair hadroproduction with leptonic decay at next-to-leading order*,  
 2575 *JHEP* **02** (2011) 083 [[arXiv:1012.4230](#)].
- 2576 [189] R. Frederix, *Top Quark Induced Backgrounds to Higgs Production in the*  
 2577  *$WW^{(*)} \rightarrow ll\nu\nu$  Decay Channel at Next-to-Leading-Order in QCD*, *Phys. Rev.*  
 2578 *Lett.* **112** (2014) 082002 [[arXiv:1311.4893](#)].
- 2579 [190] F. Cascioli, S. Kallweit, P. Maierhöfer et al., *A unified NLO description of*  
 2580 *top-pair and associated  $Wt$  production*, *Eur. Phys. J.* **C74** (2014) 2783  
 2581 [[arXiv:1312.0546](#)].

## Bibliography

- 2582 [191] A. Denner and M. Pellen, *Off-shell production of top-antitop pairs in the*  
2583 *lepton+jets channel at NLO QCD*, *JHEP* **02** (2018) 013 [arXiv:1711.10359].
- 2584 [192] G. Heinrich, A. Maier, R. Nisius et al., *NLO QCD corrections to WWbb*  
2585 *production with leptonic decays in the light of top quark mass and asymmetry*  
2586 *measurements*, *JHEP* **2014** (2014) 158.
- 2587 [193] A. Denner, S. Dittmaier, S. Kallweit et al., *NLO QCD corrections to off-shell*  
2588 *top-antitop production with leptonic decays at hadron colliders*, *JHEP* **2012**  
2589 (2012) 110.
- 2590 [194] S. Höche and J.C. Winter. Private communication.
- 2591 [195] ATLAS collaboration, *Measurement of the top quark mass in the  $t\bar{t} \rightarrow$  dilepton*  
2592 *channel from  $\sqrt{s} = 8$  TeV ATLAS data*, *Phys. Lett.* **B761** (2016) 350–371  
2593 [arXiv:1606.02179].
- 2594 [196] M. Cacciari and G.P. Salam, *Dispelling the  $N^3$  myth for the  $k_t$  jet-finder*, *Phys.*  
2595 *Lett.* **B641** (2006) 57–61 [arXiv:hep-ph/0512210].
- 2596 [197] M. Cacciari, G.P. Salam and G. Soyez, *FastJet User Manual*, *Eur. Phys. J.* **C72**  
2597 (2012) 1896 [arXiv:1111.6097].
- 2598 [198] S. Höche, J. Huang, G. Luisoni et al., *Zero and one jet combined next-to-leading*  
2599 *order analysis of the top quark forward-backward asymmetry*, *Phys. Rev.* **D88**  
2600 (2013) 014040 [arXiv:1306.2703].
- 2601 [199] A. Buckley, J. Butterworth, L. Lönnblad et al., *Rivet user manual*, *Comput.*  
2602 *Phys. Commun.* **184** (2013) 2803–2819 [arXiv:1003.0694].
- 2603 [200] G. Heinrich, A. Maier, R. Nisius et al., *NLO and off-shell effects in top quark*  
2604 *mass determinations*, *JHEP* **07** (2018) 129 [arXiv:1709.08615].
- 2605 [201] C.G. Lester and D.J. Summers, *Measuring masses of semiinvisibly decaying*  
2606 *particles pair produced at hadron colliders*, *Phys. Lett.* **B463** (1999) 99–103  
2607 [arXiv:hep-ph/9906349].
- 2608 [202] A. Barr, C. Lester and P. Stephens,  *$m(T2)$ : The Truth behind the glamour*, *J.*  
2609 *Phys.* **G29** (2003) 2343–2363 [arXiv:hep-ph/0304226].
- 2610 [203] V. Blobel, *An Unfolding method for high-energy physics experiments*, in *Advanced*  
2611 *Statistical Techniques in Particle Physics. Proceedings, Conference, Durham,*  
2612 *UK, March 18-22, 2002*, 258–267, 2002, [arXiv:hep-ex/0208022],  
2613 <http://www.ippp.dur.ac.uk/Workshops/02/statistics/proceedings//blobel2.pdf>.
- 2614 [204] ATLAS collaboration, *Optimisation of the ATLAS b-tagging performance for the*  
2615 *2016 LHC Run*, Tech. Rep. ATL-PHYS-PUB-2016-012, CERN, Geneva, Jun  
2616 2016.

- 2617 [205] ATLAS collaboration, *Flavour tagging algorithms and performance at the*  
 2618 *ATLAS experiment*, Tech. Rep. ATL-PHYS-PROC-2016-105, CERN, Geneva,  
 2619 Aug 2016.
- 2620 [206] ATLAS collaboration, *Observation of a new particle in the search for the*  
 2621 *Standard Model Higgs boson with the ATLAS detector at the LHC*, *Phys. Lett.*  
 2622 **B716** (2012) 1–29 [[arXiv:1207.7214](#)].
- 2623 [207] CMS collaboration, *Observation of a new boson at a mass of 125 GeV with the*  
 2624 *CMS experiment at the LHC*, *Phys. Lett.* **B716** (2012) 30–61 [[arXiv:1207.7235](#)].
- 2625 [208] E.W.N. Glover and J.J. van der Bij, *Higgs Boson Pair Production via Gluon*  
 2626 *Fusion*, *Nucl. Phys.* **B309** (1988) 282.
- 2627 [209] M. Spira, A. Djouadi, D. Graudenz et al., *Higgs boson production at the LHC*,  
 2628 *Nucl. Phys.* **B453** (1995) 17–82 [[arXiv:hep-ph/9504378](#)].
- 2629 [210] R. Bonciani, A. Ferroglia, P. Mastrolia et al., *Two-loop  $N(F)=1$  QED Bhabha*  
 2630 *scattering differential cross section*, *Nucl. Phys.* **B701** (2004) 121–179  
 2631 [[arXiv:hep-ph/0405275](#)].
- 2632 [211] C. Anastasiou, S. Beerli, S. Bucherer et al., *Two-loop amplitudes and master*  
 2633 *integrals for the production of a Higgs boson via a massive quark and a*  
 2634 *scalar-quark loop*, *JHEP* **01** (2007) 082 [[arXiv:hep-ph/0611236](#)].
- 2635 [212] G. Degrassi, P.P. Giardino and R. Gröber, *On the two-loop virtual QCD*  
 2636 *corrections to Higgs boson pair production in the Standard Model*, *Eur. Phys. J.*  
 2637 **C76** (2016) 411 [[arXiv:1603.00385](#)].
- 2638 [213] R. Bonciani, V. Del Duca, H. Frellesvig et al., *Next-to-leading order QCD*  
 2639 *corrections to the decay width  $H \rightarrow Z\gamma$* , *JHEP* **08** (2015) 108 [[arXiv:1505.00567](#)].
- 2640 [214] T. Gehrmann, S. Guns and D. Kara, *The rare decay  $H \rightarrow Z\gamma$  in perturbative*  
 2641 *QCD*, *JHEP* **09** (2015) 038 [[arXiv:1505.00561](#)].
- 2642 [215] R. Gröber, A. Maier and T. Rauh, *Reconstruction of top-quark mass effects in*  
 2643 *Higgs pair production and other gluon-fusion processes*, *JHEP* **03** (2018) 020  
 2644 [[arXiv:1709.07799](#)].
- 2645 [216] R. Bonciani, G. Degrassi, P.P. Giardino et al., *Analytical Method for*  
 2646 *Next-to-Leading-Order QCD Corrections to Double-Higgs Production*, *Phys. Rev.*  
 2647 *Lett.* **121** (2018) 162003 [[arXiv:1806.11564](#)].
- 2648 [217] G. Mishima, *High-Energy Expansion of Two-Loop Massive Four-Point Diagrams*,  
 2649 *JHEP* **02** (2019) 080 [[arXiv:1812.04373](#)].
- 2650 [218] J. Davies, G. Mishima, M. Steinhauser et al., *Double Higgs boson production at*  
 2651 *NLO in the high-energy limit: complete analytic results*, *JHEP* **01** (2019) 176  
 2652 [[arXiv:1811.05489](#)].

## Bibliography

- [219] S. Borowka, N. Greiner, G. Heinrich et al., *Full top quark mass dependence in Higgs boson pair production at NLO*, *JHEP* **10** (2016) 107 [arXiv:1608.04798].
- [220] A. von Manteuffel and C. Studerus, *Reduze 2 - Distributed Feynman Integral Reduction*, [arXiv:1201.4330].
- [221] J. Carter and G. Heinrich, *SecDec: A general program for sector decomposition*, *Comput. Phys. Commun.* **182** (2011) 1566–1581 [arXiv:1011.5493].
- [222] S. Borowka, J. Carter and G. Heinrich, *Numerical Evaluation of Multi-Loop Integrals for Arbitrary Kinematics with SecDec 2.0*, *Comput. Phys. Commun.* **184** (2013) 396–408 [arXiv:1204.4152].
- [223] S. Borowka, G. Heinrich, S.P. Jones et al., *SecDec-3.0: numerical evaluation of multi-scale integrals beyond one loop*, *Comput. Phys. Commun.* **196** (2015) 470–491 [arXiv:1502.06595].
- [224] S.P. Jones, *Automation of 2-loop Amplitude Calculations*, *PoS LL2016* (2016) 069 [arXiv:1608.03846].
- [225] J. Baglio, F. Campanario, S. Glaus et al., *Gluon fusion into Higgs pairs at NLO QCD and the top mass scheme*, [arXiv:1811.05692].
- [226] G. Buchalla, O. Catà and C. Krause, *Complete Electroweak Chiral Lagrangian with a Light Higgs at NLO*, *Nucl. Phys.* **B880** (2014) 552–573 [arXiv:1307.5017].
- [227] G. Buchalla, O. Catá and C. Krause, *On the Power Counting in Effective Field Theories*, *Phys. Lett.* **B731** (2014) 80–86 [arXiv:1312.5624].
- [228] G. Buchalla, M. Capozi, A. Celis et al., *Higgs boson pair production in non-linear Effective Field Theory with full  $m_t$ -dependence at NLO QCD*, *JHEP* **09** (2018) 057 [arXiv:1806.05162].
- [229] C. Degrande, C. Duhr, B. Fuks et al., *UFO - The Universal FeynRules Output*, *Comput. Phys. Commun.* **183** (2012) 1201–1214 [arXiv:1108.2040].
- [230] A. Alloul, N.D. Christensen, C. Degrande et al., *FeynRules 2.0 - A complete toolbox for tree-level phenomenology*, *Comput. Phys. Commun.* **185** (2014) 2250–2300 [arXiv:1310.1921].
- [231] N.D. Christensen and C. Duhr, *FeynRules - Feynman rules made easy*, *Comput. Phys. Commun.* **180** (2009) 1614–1641 [arXiv:0806.4194].
- [232] A. Carvalho, M. Dall’Osso, T. Dorigo et al., *Higgs Pair Production: Choosing Benchmarks With Cluster Analysis*, *JHEP* **04** (2016) 126 [arXiv:1507.02245].
- [233] A. Djouadi, M. Spira and P. Zerwas, *Production of Higgs bosons in proton colliders. QCD corrections*, *Physics Letters B* **264** (1991) 440 – 446.

## Bibliography

- 2687 [234] S. Dawson, *Radiative corrections to Higgs boson production*, *Nucl. Phys.* **B359**  
2688 (1991) 283–300.
- 2689 [235] R. Grober, M. Muhlleitner, M. Spira et al., *NLO QCD Corrections to Higgs Pair*  
2690 *Production including Dimension-6 Operators*, *JHEP* **09** (2015) 092  
2691 [arXiv:1504.06577].
- 2692 [236] A. Azatov, R. Contino, G. Panico et al., *Effective field theory analysis of double*  
2693 *Higgs boson production via gluon fusion*, *Phys. Rev.* **D92** (2015) 035001  
2694 [arXiv:1502.00539].
- 2695 [237] G. Heinrich, S.P. Jones, M. Kerner et al., *NLO predictions for Higgs boson pair*  
2696 *production with full top quark mass dependence matched to parton showers*,  
2697 *JHEP* **08** (2017) 088 [arXiv:1703.09252].
- 2698 [238] M. Cacciari, G.P. Salam and G. Soyez, *The Anti- $k(t)$  jet clustering algorithm*,  
2699 *JHEP* **04** (2008) 063 [arXiv:0802.1189].
- 2700 [239] *Les Houches 2017: Physics at TeV Colliders Standard Model Working Group*  
2701 *Report*, 2018.
- 2702 [240] S. Ferrario Ravasio, T. Jezo, P. Nason et al., *A Theoretical Study of Top-Mass*  
2703 *Measurements at the LHC Using NLO+PS Generators of Increasing Accuracy*,  
2704 [arXiv:1801.03944].

# 2705 A Further template fit plots

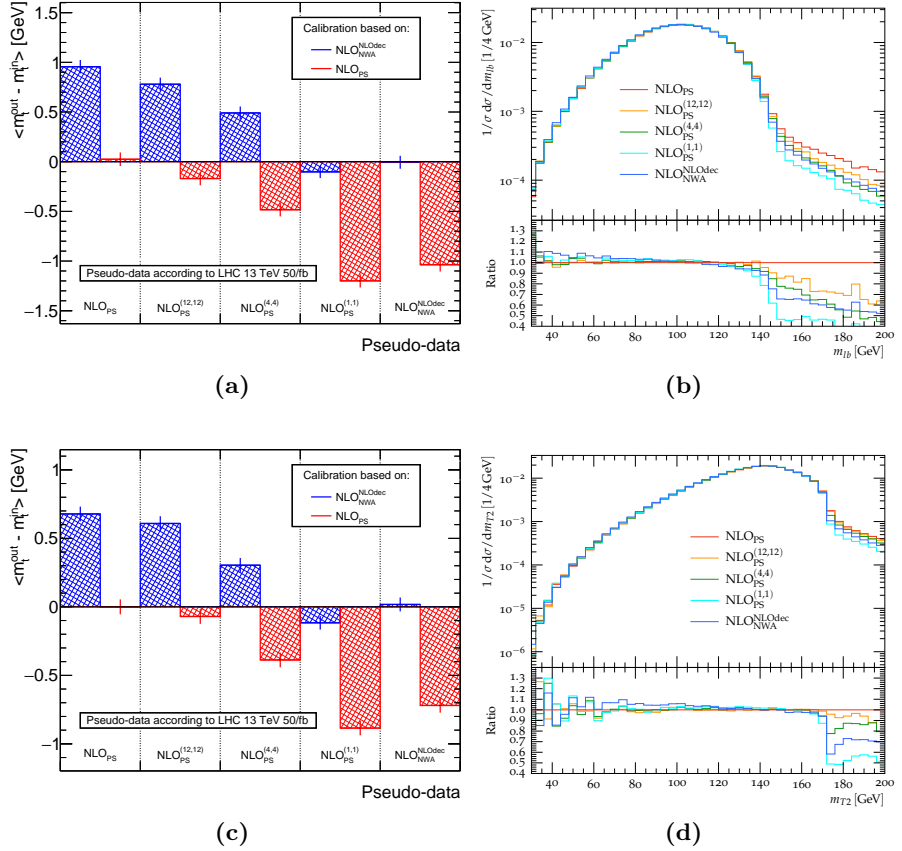


**Figure A.1**

**Figure A.2:** (a) The mass offsets  $\Delta m_t$  fitted from the  $m_{\ell b}$  distribution are shown for restricted-shower pseudo-data samples  $\text{NLO}_{\text{PS}}^{(n_{\text{max}}^{\text{prod}}, n_{\text{max}}^{\text{dec}})}$ , where the shower is terminated after a certain number of emissions  $n_{\text{max}}$  in the  $t\bar{t}$  production and decay showers. They are compared to the full parton-shower and the  $\text{NLO}_{\text{NWA}}^{\text{NLOdec}}$  pseudo-data prediction. For each of these pseudo-data sets, the offset in  $m_t$  is given as a colored bar (in blue for the  $\text{NLO}_{\text{NWA}}^{\text{NLOdec}}$  calibration function, respectively in red when using the  $\text{NLO}_{\text{PS}}$  calibration). (b) The corresponding normalized  $m_{\ell b}$  distribution is plotted for the mentioned predictions at  $m_t = 172.5$  GeV. (c-d) Same as (a-b) but for  $m_{T2}$ .

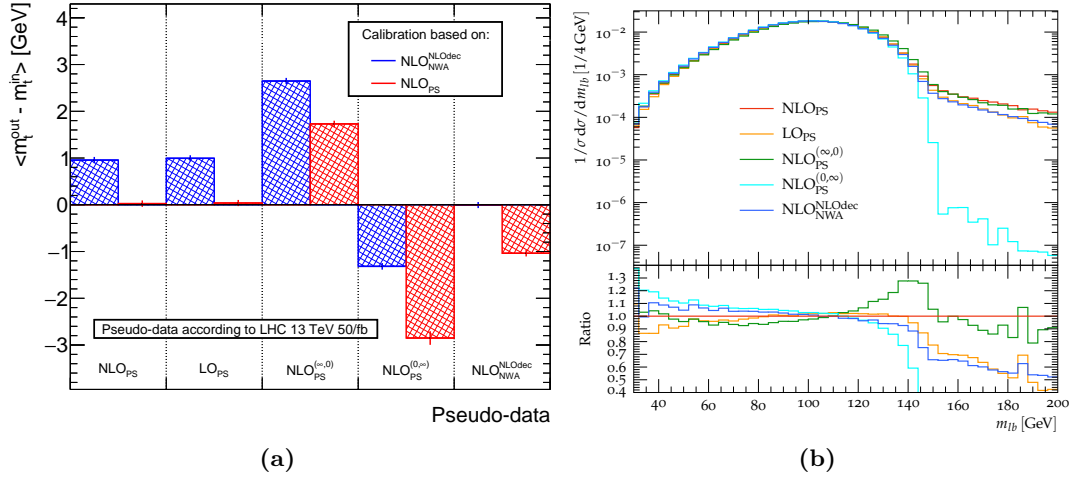


**Figure A.3:** Same as Fig. A.2, but for the  $\text{NLO}_{\text{PS}}$  and  $\text{LO}_{\text{PS}}$  cases, as well as for pseudo-data sets generated by predictions where the decay shower, respectively the production shower are entirely deactivated.

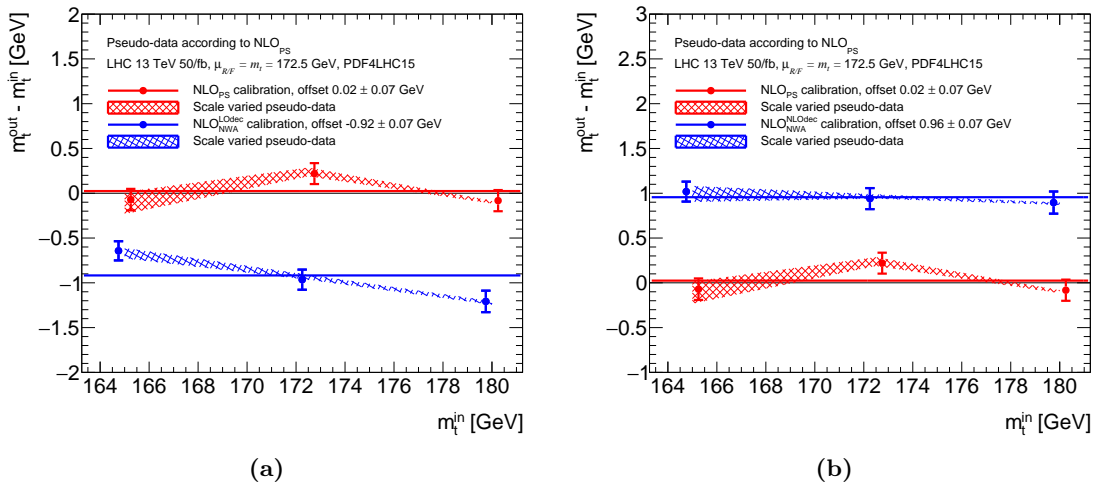


**Figure A.4:** Further band plots from  $m_{\ell b}$  fitted pseudo-data sets.

## A Further template fit plots

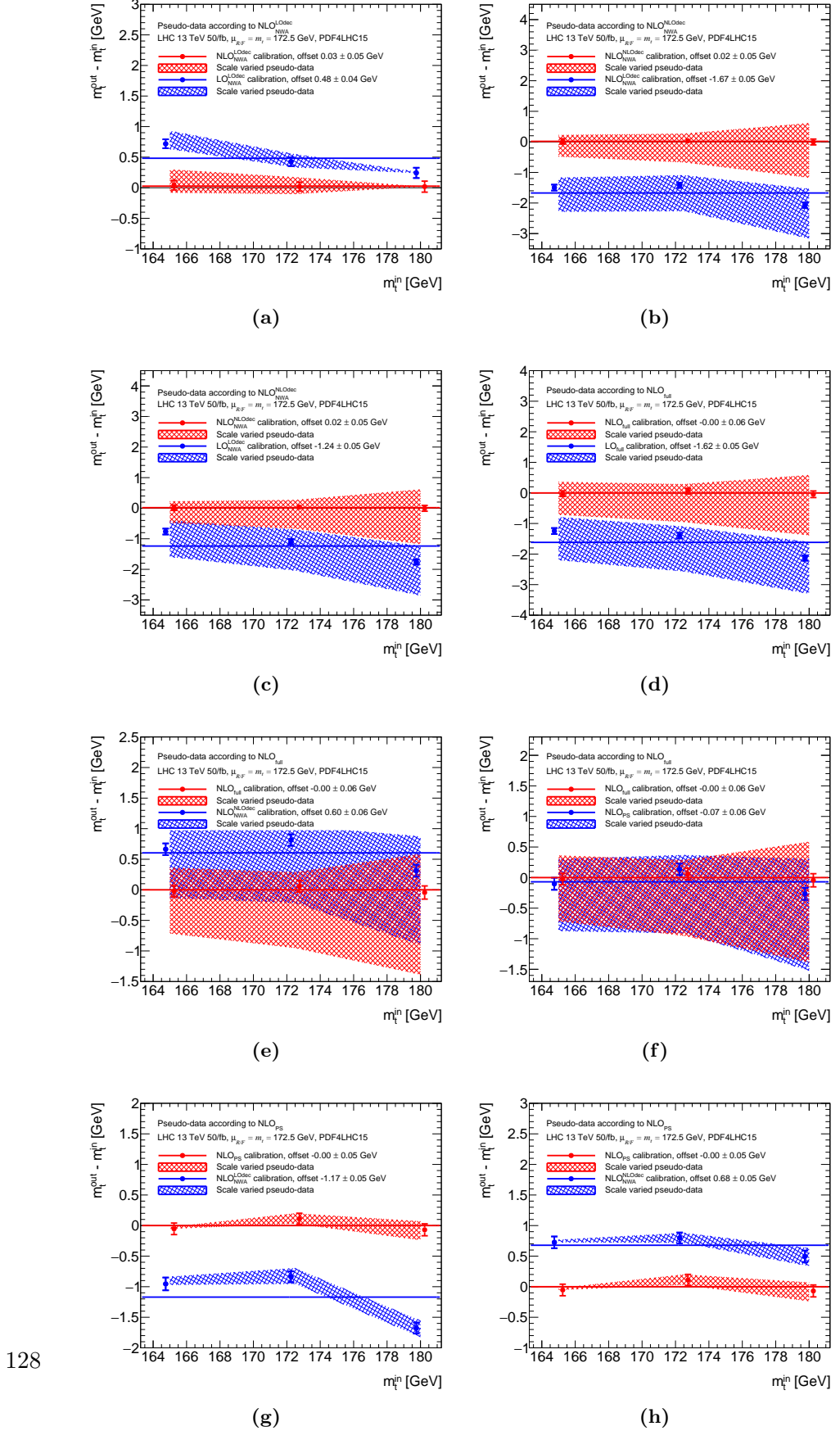


**Figure A.5:** Further band plots from  $m_{T2}$  fitted pseudo-data sets.

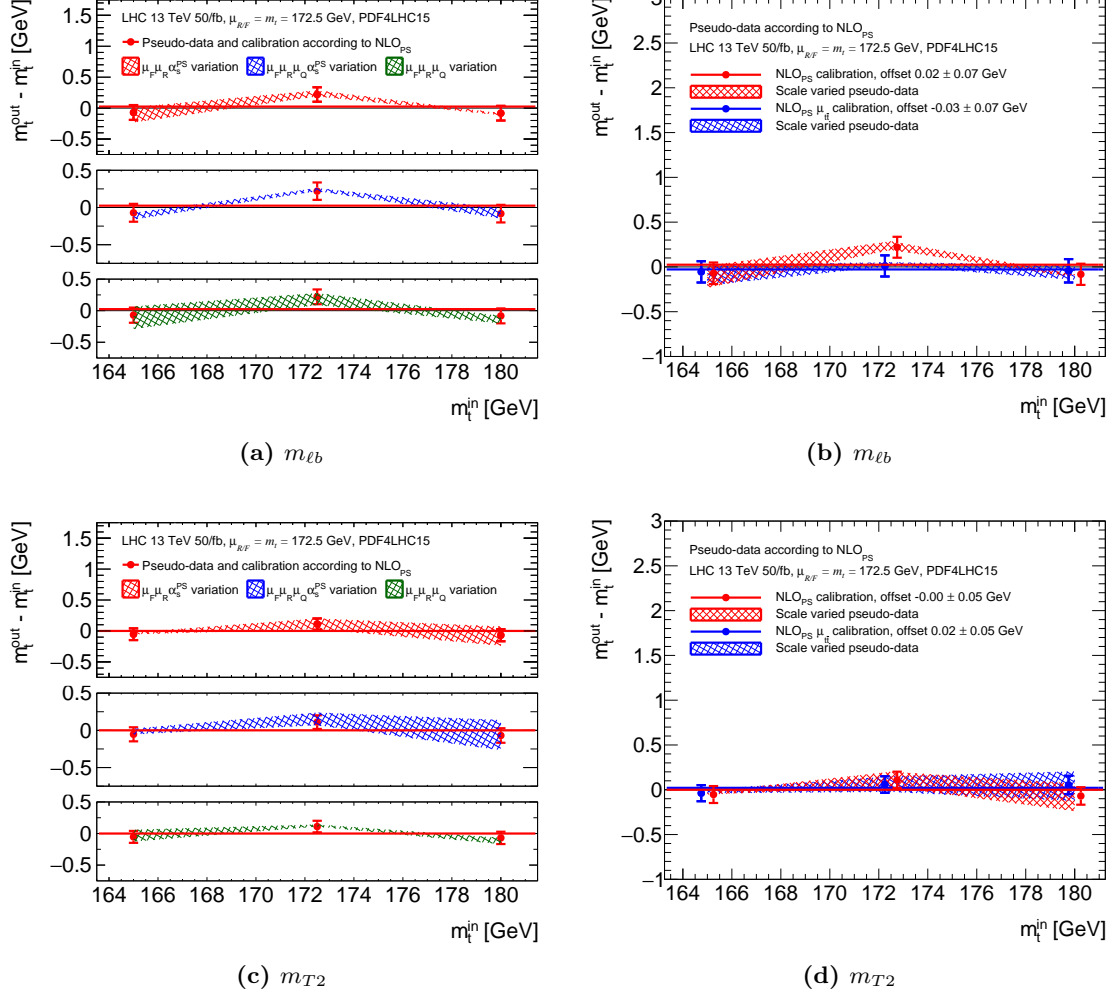


**Figure A.6:** Offsets from NLOPS predictions comparing (a) different prescriptions for evaluating the shower scale uncertainties and (b) the two different central scale choices described in the text.

2706 **B Color-flow comparisons for Sherpa**

## 2707 C BSM benchmark points in $hh$ production

2708 The coefficients  $A_i$ ,  $i = 1, \dots, 23$  (15) defined for the general expression of the NLO (LO)  
 2709 cross-section as a function of the anomalous Higgs couplings in Eq. (10.16) are shown  
 2710 in Table C.1, at 13 TeV at LHC. To compute these, the cross-section was calculated for  
 2711 different values of the couplings that were replaced in Eq. (10.16), thus giving a system  
 2712 of equations that one can project out to extract the values of the coefficients  $A_i$ .

2713 The LO and NLO coefficients for  $\sqrt{s} = 13, 14$  and  $27$  TeV are available on the ARXIV  
 2714 e-print of Ref. [228], as well as a Mathematica file explaining how to use them. These  
 2715 can also be derived differentially for a fixed bin width. The differential coefficients can  
 2716 also be downloaded for the  $m_{hh}$  distribution, with the binning shown in our histograms.

$A_i$	$A_i^{\text{LO}}$	$\Delta A_i^{\text{LO}}$	$A_i^{\text{NLO}}$	$\Delta A_i^{\text{NLO}}$
$A_1$	2.0806	0.0016	2.2339	0.0101
$A_2$	10.2011	0.0081	12.4598	0.0424
$A_3$	0.2781	0.0019	0.3422	0.0154
$A_4$	0.3140	0.0003	0.3468	0.0033
$A_5$	12.2731	0.0101	13.0087	0.0962
$A_6$	-8.4931	0.0089	-9.6455	0.0504
$A_7$	-1.3587	0.0015	-1.5755	0.0136
$A_8$	2.8025	0.0131	3.4385	0.0772
$A_9$	2.4802	0.0128	2.8669	0.0772
$A_{10}$	14.6908	0.0311	16.6912	0.1785
$A_{11}$	-1.1592	0.0031	-1.2529	0.0291
$A_{12}$	-5.5118	0.0131	-5.8122	0.1340
$A_{13}$	0.5605	0.0034	0.6497	0.0287
$A_{14}$	2.4798	0.0190	2.8593	0.1930
$A_{15}$	2.8943	0.0158	3.1448	0.1487
$A_{16}$			-0.008162	0.000225
$A_{17}$			0.020865	0.000399
$A_{18}$			0.016816	0.000783
$A_{19}$			0.029858	0.000829
$A_{20}$			-0.027025	0.000702
$A_{21}$			0.072692	0.001288
$A_{22}$			0.014523	0.000704
$A_{23}$			0.123291	0.006506

**Table C.1:** The coefficients defined in Eqs. (10.15), (10.16) are determined by computing cross-sections for a subset of parameters, and projecting out equations for the  $A_i$ 's. Statistical uncertainties are propagated from the cross-section level to the coefficient result, without correlations.

C BSM benchmark points in  $hh$  production

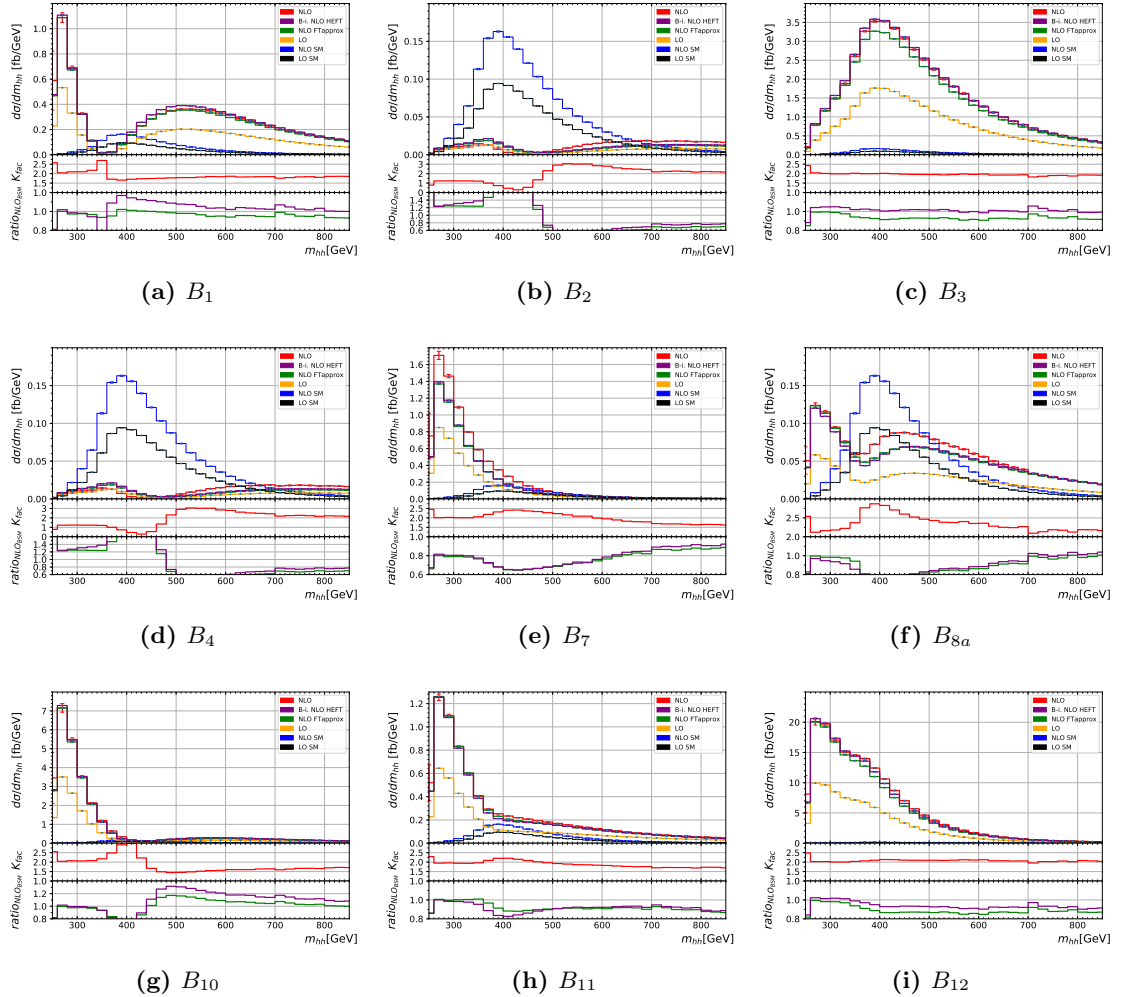


**Figure C.1:** The invariant mass of the Higgs boson pair  $m_{hh}$  is shown for the different benchmark points  $B_i$ ,  $i = 1, \dots, 12$  defined in Table 10.1 and not already shown in Chapter 10.

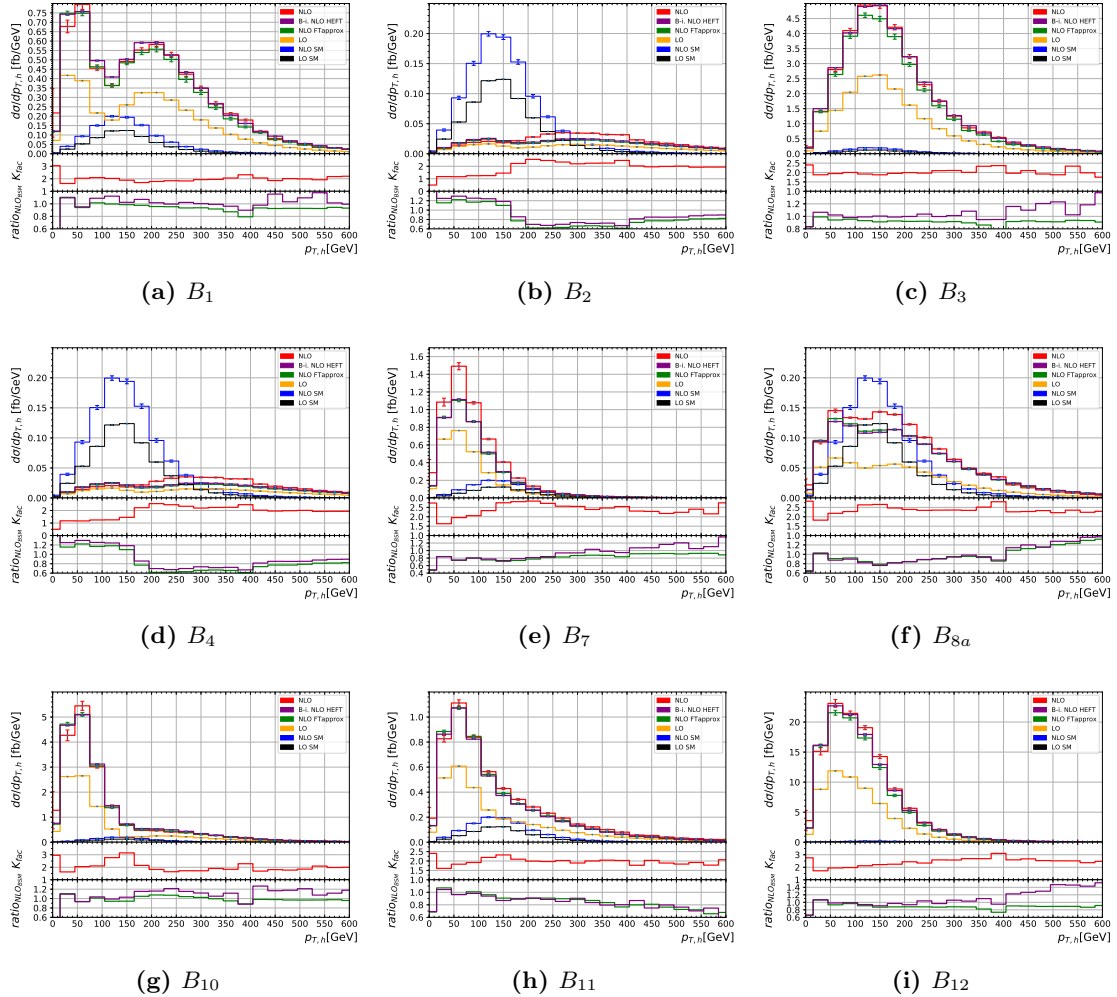


**Figure C.2:** The transverse momentum  $p_{T,h}$  of one (any) Higgs boson is shown for the different benchmark points  $B_i$ ,  $i = 1, \dots, 12$  defined in Table 10.1 and not already shown in Chapter 10.

## 2717 D Hardness definitions in matching Powheg 2718 to Pythia

2719     The technical parameters for matching the **Pythia** 8 parton-shower to LHE files pro-  
2720     duced by **POWHEG** are defined in a file called `main31.cmnd`, which bases on the LHE  
2721     showering example from **Pythia**. There, several definitions for the additional radia-  
2722     tion have to be set in order for the parton-shower to avoid double-counting regions of  
2723     phase-space already covered by **POWHEG**. We set:

- 2724       • The number of final-state particles in the Born process  $gg \rightarrow hh$ .

2725           **POWHEG:nFinal = 2**

- 2726       • The parton-shower vetoes emissions that have a transverse momentum higher than  
2727       the hardest **POWHEG** emission, and checks the first three. A veto is applied if  
2728       **pTemt > pThard** (see below).

2729           **POWHEG:veto = 1**

2730           **POWHEG:vetoCount = 3**

- 2731       • The **pTemt** and **pThard** scale definition is set: **pTemt** is set to the transverse mo-  
2732       mentum of the radiated particle with respect to the emitting parton, and **pThard** is  
2733       set to the **SCALUP** value read in the LHE event, and set by **POWHEG**. The definition  
2734       of the emitted parton is chosen by **Pythia** for the final-state radiation.

2735           **POWHEG:pTemt = 0**

2736           **POWHEG:pThard = 0**

2737           **POWHEG:emitted = 0**

2738           **POWHEG:pTdef = 1**

2739     The hardness **pTdef** is defined by the transverse momentum  $p_T$  for initial-state  
2740     radiation, and with the distance between radiator and emitted partons  $d_{ij}$  for  
2741     final-state radiation corresponding to the **POWHEG** definition given by:

$$d_{ij} = \frac{m_{ij}^2 E_i E_j}{(E_i + E_j)^2} .$$

## 2742 Acknowledgments

2743 First and foremost, I am infinitely grateful to both my supervisors, Stefan Kluth on the  
2744 ATLAS computing side, and Gudrun Heinrich in the phenomenology group, for actively  
2745 following my progress and keeping me on the right track with always astute advice. I  
2746 could not have done it without their considerate help and encouragement.

2747 I am much obliged to all my publication collaborators, past and present, for their  
2748 hard work, spontaneity and for maintaining an ever enjoyable working atmosphere: G.  
2749 Buchalla, A. Celis, M. Capozi, G. Heinrich, S. Jones, M. Kerner, G. Luisoni, R. Mah-  
2750 bubani, A. Maier, R. Nisius, H. Rzehak, J. Schlenk, M. Schulze and J. Winter. I would  
2751 also like to thank A. Knue and B. Pearson for their incredible understanding of all  
2752 the tiny details of the ATLAS analysis. They are responsible for making the interface  
2753 comprehensible, which probably saved me a lot of nightmarish headaches.

2754 Of course, there is no office without officemates: my appreciation goes to A. Knue, A.  
2755 Verbitskyi, D. Britzger, F. Klimpel and S. Schulte from the ATLAS computing group,  
2756 for the lively discussions and the enormous pleasure I had working with you.

2757 Much valued was the time spent with the people from Gudrun's phenomenology group:  
2758 it is not always easy to move to a new city or meet entirely new people, and for the casual  
2759 climate and the few Oktoberfest visits together, I am most grateful. Thanks to H. Bahl,  
2760 M. Capozi, L. Chen, S. Hessenberger, S. Jahn, V. Papara, C. Pietsch, J. Schlenk, T.  
2761 Zirke for making my first few months in Munich brighter.

2762 I am eternally indebted to all the excellent friends that made the time at the Institute  
2763 seem relativistically short, in particular those living permanently in, or sporadically  
2764 passing by Connollystrasse: E. Bertoldo, M. Capozi, G. (Giovanni), N. Ferreiro, M.  
2765 Mancuso, E. Vitagliano, F. (Francesco), P. (Pablo).

2766 I cannot stress enough how much friends were important to my mental sanity: after  
2767 the long hours and weekends of work, it was always good to know whom to count on for  
2768 releasing the pressure. This also applies to all the people whose visits from Switzerland  
2769 rekindled the spark after a weekend of partying. Lots and lots of thanks to B. Despond,  
2770 M. Predikaka and K. Novoselc, A. Du Cos, A. Lichtlé, C. Crusem, (Zurich guyz).

2771 To my girlfriend at the time, Marthe, I want to say how grateful I am for the moments  
2772 we enjoyed together. The last two years had an indescribably carefree, tender feel, and  
2773 I am profoundly glad to have walked part of the path with you.

2774 Finally, I offer my last resounding thanks to my whole family, in particular to my  
2775 parents and my siblings. Without my parents, I would never have a life nearly as  
2776 exciting and vibrant as this one. Thank you for what I know sometimes amounted to  
2777 difficult sacrifices, and for your unfaltering support. To my brother and sister, thank  
2778 you for the frequent calls, the fun times in Gruyère, Munich or wherever halfway was,  
2779 and generally for keeping me anchored in the normal world.